MODELING AN INTERNAL HYDRAULIC SYSTEM WHICH CONTROLS BALL MOTIONS WITHIN A BOUNDED FLUID

by

DIANE IDEC CHAMBERS

B.S., Massachusetts Institute of Technology

(1975)

SUBMITTED IN PARTIAL FULFILLMENT

OF THE REQUIREMENTS FOR THE

DEGREE OF

MASTER OF SCIENCE

at the

MASSACHUSETTS INSTITUTE OF TECHNOLOGY

(May, 1976)

Signature of Author Signature redacted
Department of Mechanical Engineering, May, 1976

Certified by Signature redacted
Thesis Supervisor

Accepted by Signature redacted
Chairman, Department Committee on Graduate Students

MODELING AN INTERNAL HYDRAULIC SYSTEM WHICH CONTROLS BALL MOTIONS WITHIN A BOUNDED FLUID

by

DIANE IDEC CHAMBERS

Submitted to the Department of Mechanical Engineering on May 7, 1976 in partial fulfillment of the requirements for the Degree of Master of Science

ABSTRACT

A ball is floated in a fluid and encased in a spherical shell. This thesis models and analyzes the hydraulic system necessary to preserve the orientation of the ball with respect to an inertial frame regardless of outer shell motions. Two subsystems are investigated: a series of hydrostatic bearings on the ball surface control ball radial translation relative to the shell and a set of tangentially directed jets control attempted ball rotation. The fluid power for the two subsystems comes from a pump located in the center of the ball.

This thesis examines pressure-flow requirements of each of the two subsystems and the pump. The transduction of fluid power to mechanical power taking place in the suspension and torquing subsystems is analyzed. Dynamic responses to disturbances in both the translational and rotational modes of motion are predicted.

Thesis Supervisor: Henry M. Paynter

Title: Professor of Mechanical Engineering

ACKNOWLEDGMENTS

I would like to thank Professor H. M. Paynter, my thesis advisor, for all the help he gave me in this endeavor. His suggestions on different problem approaches were invaluable. I am grateful he always made time to see me when I needed guidance.

My thanks also go to the mechanical design group of Draper Labs. The comments and ideas of the engineers there were very useful both in my understanding of the problem and my presentation of a solution.

I am particularly grateful to my husband, Frank, for all the time and encouragement he gave me while I was working on this thesis. He always listened to my ideas and shared my problems. His help in proofreading was greatly appreciated.

This thesis was prepared under CSDL Project 52-56333, sponsored by the Space and Missile Systems Organization of the Air Force Systems Command through Contract F04701-73-C-0277. I am grateful to the Draper Lab Staff who worked on the typing and illustrations of the final document.

The publication of this report does not constitute approval by the U. S. Air Force or the Charles Stark Draper Laboratory of the finding or conclusions therein. It is published only for the exchange and stimulation of ideas.

TABLE OF CONTENTS

TABLE OF CONTENTS (Continued)

LIST OF ILLUSTRATIONS

LIST OF ILLUSTRATIONS (Continued)

LIST OF ILLUSTRATIONS (Continued)

LIST OF ILLUSTRATIONS (Continued)

CHAPTER 1

INTRODUCTION

1.1 Description of Purpose and Geometry of System

We are given a ball floated in a fluid and encased in a spherical shell. It is desired to keep the orientation of this ball unaltered with respect to an inertial frame regardless of outside disturbances to the enclosing case. The purpose of this report is to model and analyze the hydraulic system necessary to accomplish this task in order to be able to predict responses both on a static and dynamic level.

There are two basic motions of the ball within the case. Extreme eccentricities of the ball could result in collisions with the outer shell and resultant loss of inertial reference. Also, the ball cannot be permitted to turn about any of three orthogonal axes. Rotation of the outer case may tend to induce a similar motion of the sphere via the viscous drag of the annular fluid between the two members. The hydraulic system under investigation must be able to prevent rotary motions of this sort. Figure 1-1 illustrates the two modes of movement of the inner ball.

1.1.1 Suspension Subsystem

Radial translational motion is restricted by a set of eight "fluidic springs" situated symmetrically on the sphere's outer surface. By a "fluidic spring" is meant a hydraulic suspension pad. The placement of these "springs" can be pictured by imagining a cube with a circular pad on each of its eight corners enclosing the inner ball. The projection of each pad along a cube diagonal onto the sphere determines its placement on the ball. Figure 1-2 illustrates the pad positioning.

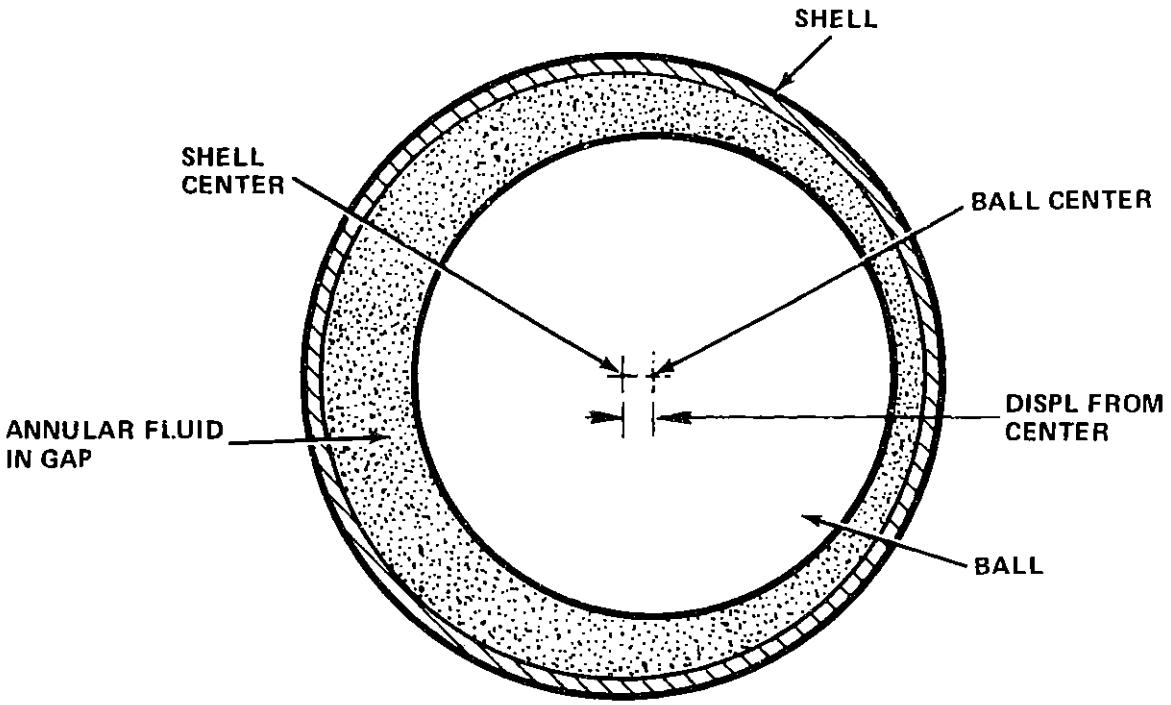

Figure 1-1. Two Modes of Inner Ball Movement

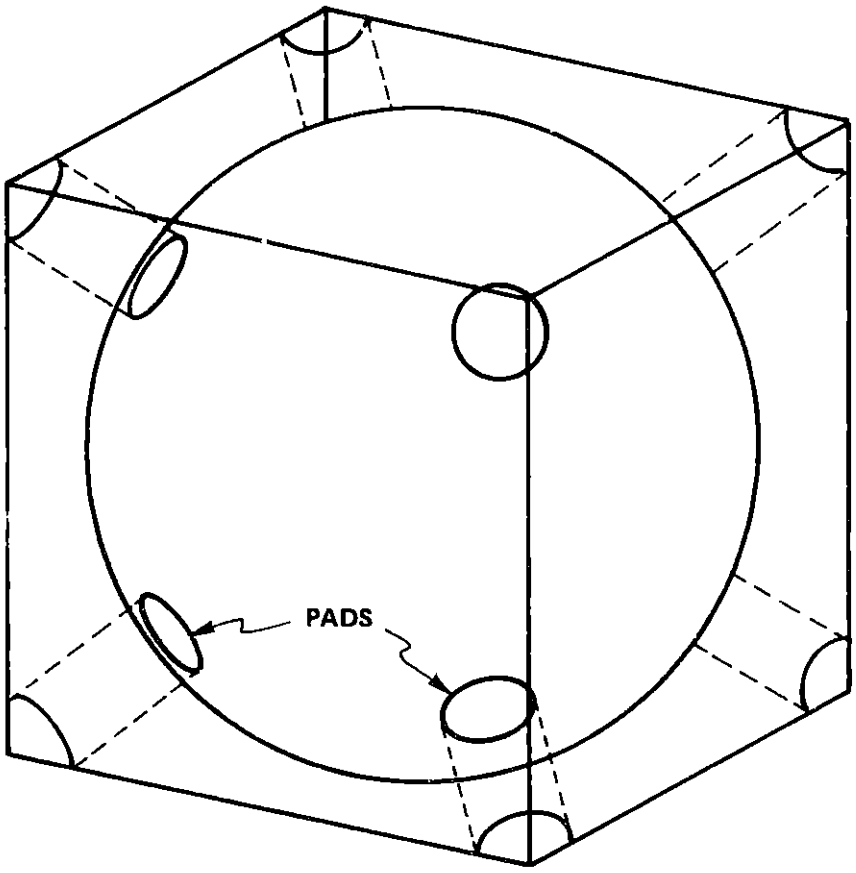

Figure 1-2. Positioning of Support Pads for Suspension System

The suspension pad itself consists of a circular disc with a recessed central portion termed the plenum. The outer spherical shell acts as one huge cover plate for all eight pads. Fluid is injected into the plenum through an orifice in the center of the plenum bottom. It fills the plenum and then flows out between the edges of "sill" of the pad and the inner surface of the shell. (See Figure 1-3.) Pressure is built up within the plenum and across the pad sill. The pressure distribution can be integrated to obtain a support force for each pad. This force increases as the clearance between the pad and the inner surface of the outer shell is decreased. Each pad acts therefore as a spring undergoing compression. All eight pads acting together serve to center the ball within its enclosing case.

1.1.2 Torquing Subsystem

To prevent inner ball rotation a method of torquing the ball needed to be devised. Two jet nozzles compose a valve in this system. (Older designs had only one nozzle per valve.) One pair of valves, or "torquer jet pair", was situated about each of three orthogonal axes of the ball. The positioning of these six valves can be envisioned as being centered on six of the twelve edges of a cube and expelling fluid in a direction perpendicular to this edge. The three orthogonal axes pass through the midpoints of the cube faces. (See Figure 1-4.) By expelling fluid tangentially from the ball into the annulus at a high velocity a reaction force couple is produced by each nozzle pair about a particular axis.

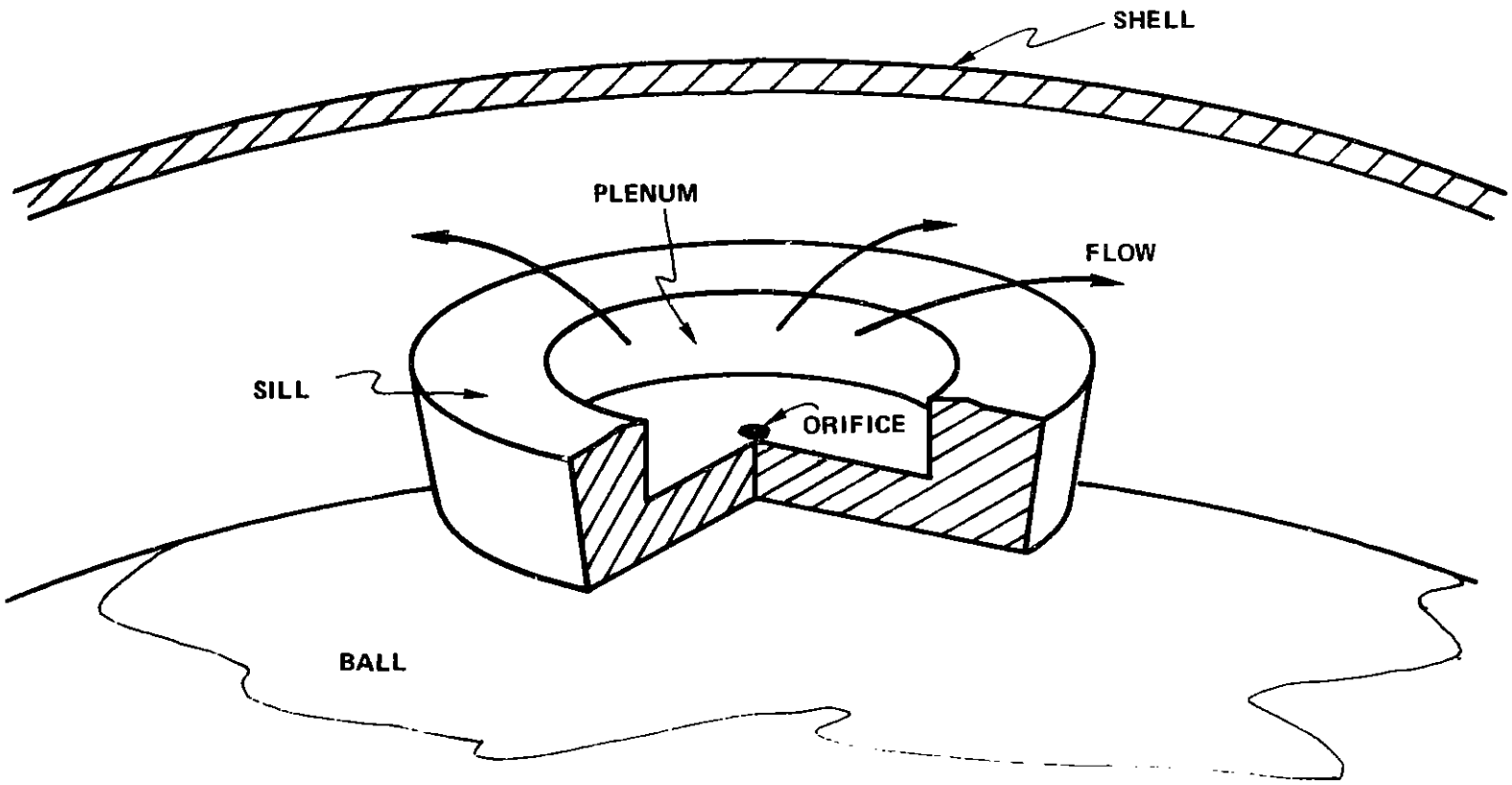

Figure 1-3. Geometry of Suspension Pad

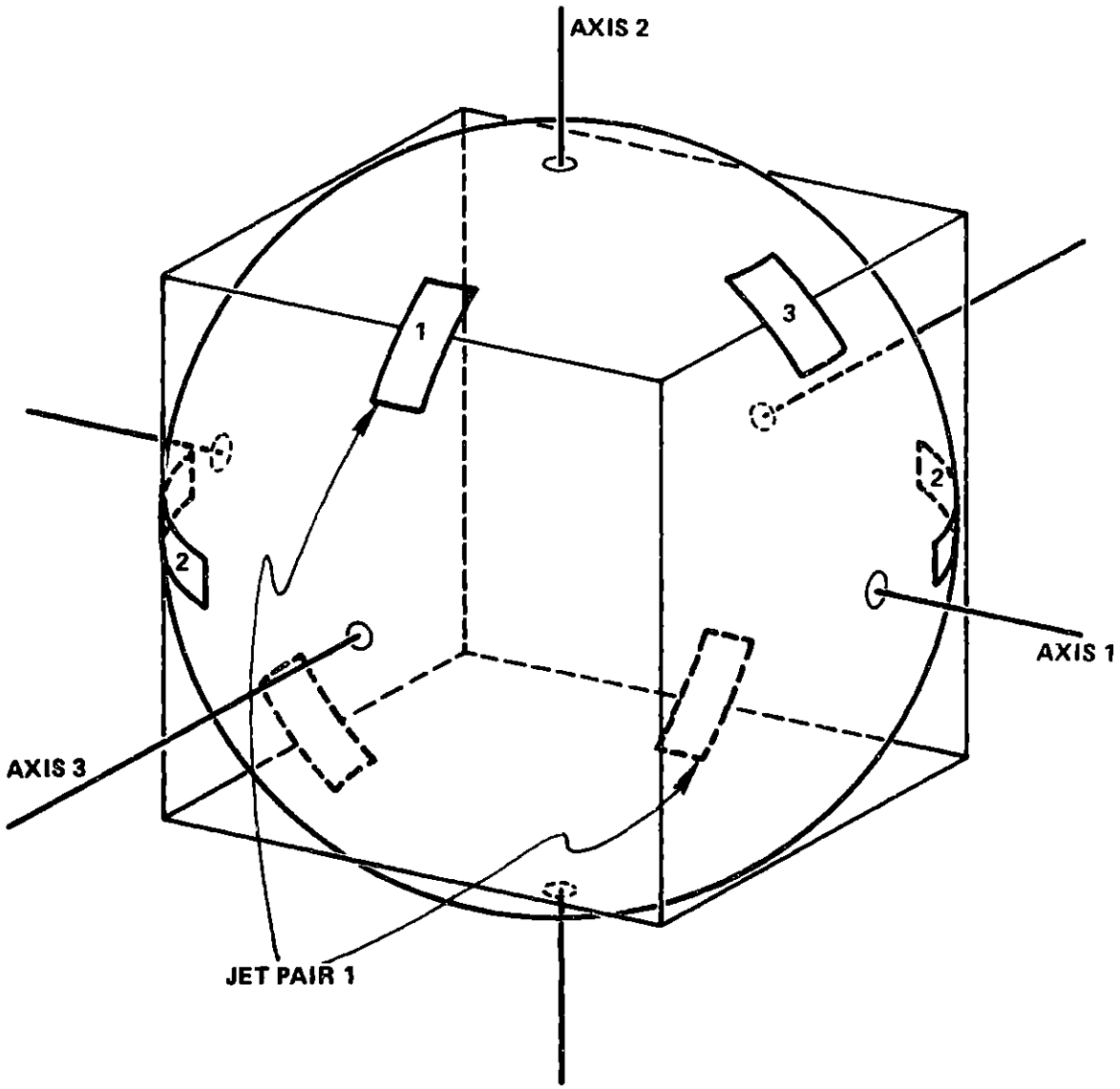

Figure 1-4. Positioning of Jet Pairs for Torquing System

Each double nozzled valve of each torquer jet pair has three modes of operation; (1) it can expel fluid at a specific flow rate to produce a reaction force contributing to a couple in a clockwise direction about the pair's axis, (2) it can expel fluid in a direction 180° opposed from (1) to produce a reaction force contributing to a couple in a counterclockwise direction, or (3) it can expel half the amount of fluid equally in both directions (neutral position) to produce no torque. (See Figure 1-5.) Combinations of these three discrete modes of operation for each jet pair acting for infinitely variable durations of time can produce continuously variable torques about any axis desired.

1.1.3 Piping to Subsystems

The fluid which enters the annular gap between the inner and outer shell from either the suspension pads or the torquer jets is pumped out to these two subsystems from a pump centered within the ball itself. Eight pathways extend radially outward from the pump toward each suspension pad or corner of the analogous cube. Two pathways feed one pad each and the remaining six pathways each guide fluid to one pad and one half of each of two valves. Figure 1-6 shows a schematic cube and accompanying table to illustrate the inner piping of the ball. In the figure, V refers to a valve and P refers to a pad. Pathways are numbered to correspond to the pad they lead to but are not drawn in the figure. This passageway connects to the particular corners that the cube edge joins. It serves as a pressure equalizer between the paths.

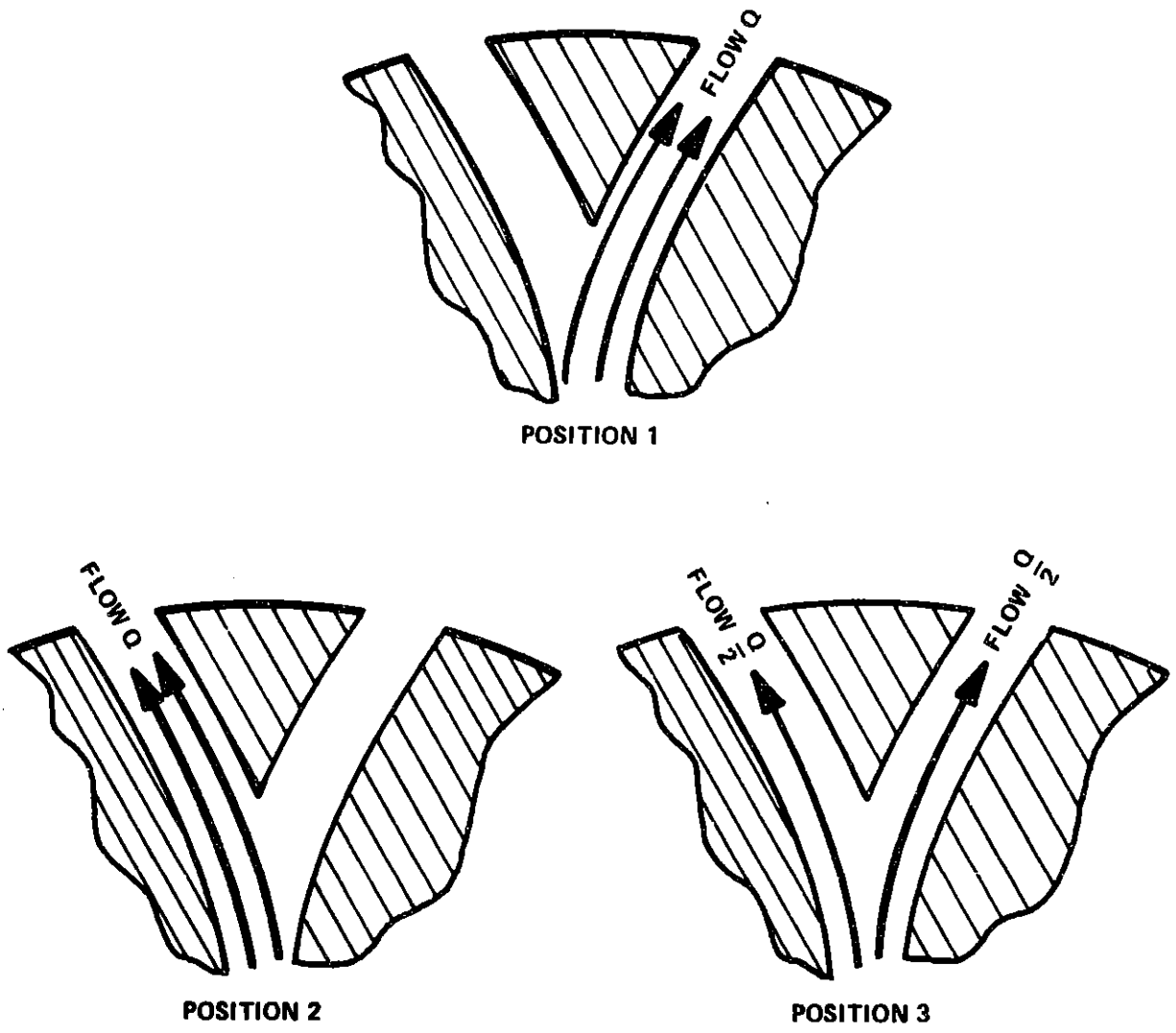

Figure 1-5. Three Operating Positions of Jet Nozzle

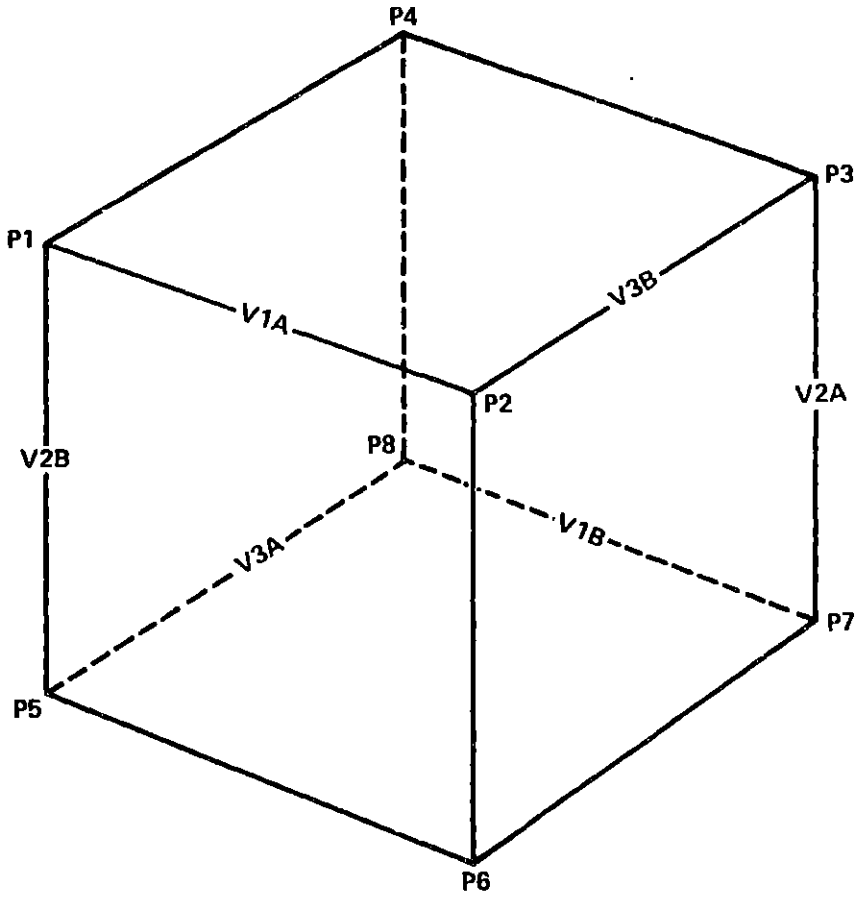

PATH #	PAD # FED	VALVES FED	
1	P1	1/2 V1A	1/2 V2B
2	P2	1/2 V1A	1/2 V3B
3	P3	1/2 V2A	1/2 V3B
4	P4		
5	P5	1/2 V2B	1/2 V3A
6	P6		
7	P7	1/2 V1B	1/2 V2A
8	P8	1/2 V1B	1/2 V3A

Figure 1-6. Inner Piping to Suspension and Torquing Subsystems

The eight major pathways split up just before reaching the sphere surface into smaller passageways which lead either to a suspension pad orifice, or to a certain half of a specific valve nozzle configuration, or to a pressure equalizing passage. That fluid which proceeds toward a valve passes first through a filter to cleanse itself of impurities and then out a nozzle in one of the three modes indicated in the previous section. The fluid which flows through a pad orifice passes out to the annular gap across the pad sills.

Once in the annular gap the fluid must be returned to the pump to complete the hydraulic loop. Three intake holes which are screened with filters are equally spaced circumferentially about each pad. The annular fluid flows in these holes and back to pump in the center of the ball through passages which parallel the eight original outlet pathways.

1.1.4 Pump

The centrally located pump used for the total hydraulic system is a centrifugal pump powered by an eight pole polyphase induction motor. The pump rotor acts as its own journal bearing while the central portion of the rotor is the impeller of the pump. Low pressure fluid enters axially through the hollow core of the rotor from either end and is pumped outward when it reaches the center. A diagram of the pump is shown in Figure 1-7.

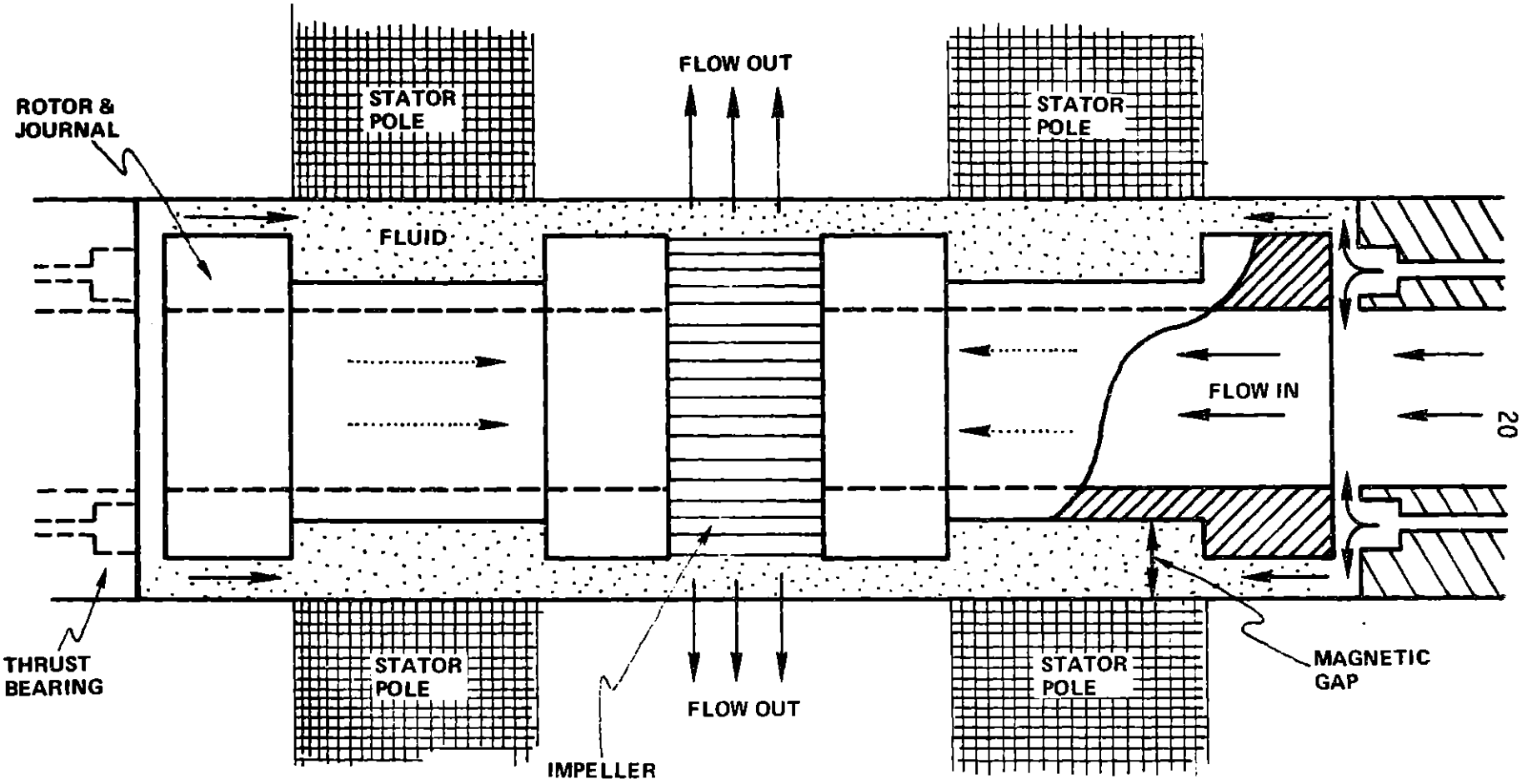

Figure 1-7. Turbopump Configuration

1.2 Modeling of System

For purposes of analysis of a system such as previously described, a mathematical model of it must be formed and computations made for that model. The values computed from such a model can be only as accurate as the model itself and their limit of credibility is confined to the regions of operation where the model is deemed valid. For example, the fluid used throughout the entire system is modeled as an incompressible, Newtonian fluid, i.e., the shear stress exerted by the fluid is proportional to the velocity gradient, the constant of proportionality being the fluid viscosity, μ. The fluid in reality is not truly incompressible. Its density ρ may change by as much as 1.1% for extremes of temperature. Its viscosity μ may change by $\pm$13.6% for the same temperature extremes. For the purposes of this analysis, however, temperature changes are assumed slight enough and slow enough as to leave the fluid density ρ and viscosity μ unaltered. Each system component was modeled in a particular way. This section explains the models used and assigns symbols to these mathematical elements. Its goal is to formulate one concise diagram illustrating the interactions of the important system variables.

1.2.1 Pump

The pump is the source of fluid power for the system. It may be modeled as a pressure source. The symbol used for a source is illustrated in Figure 1-8a.

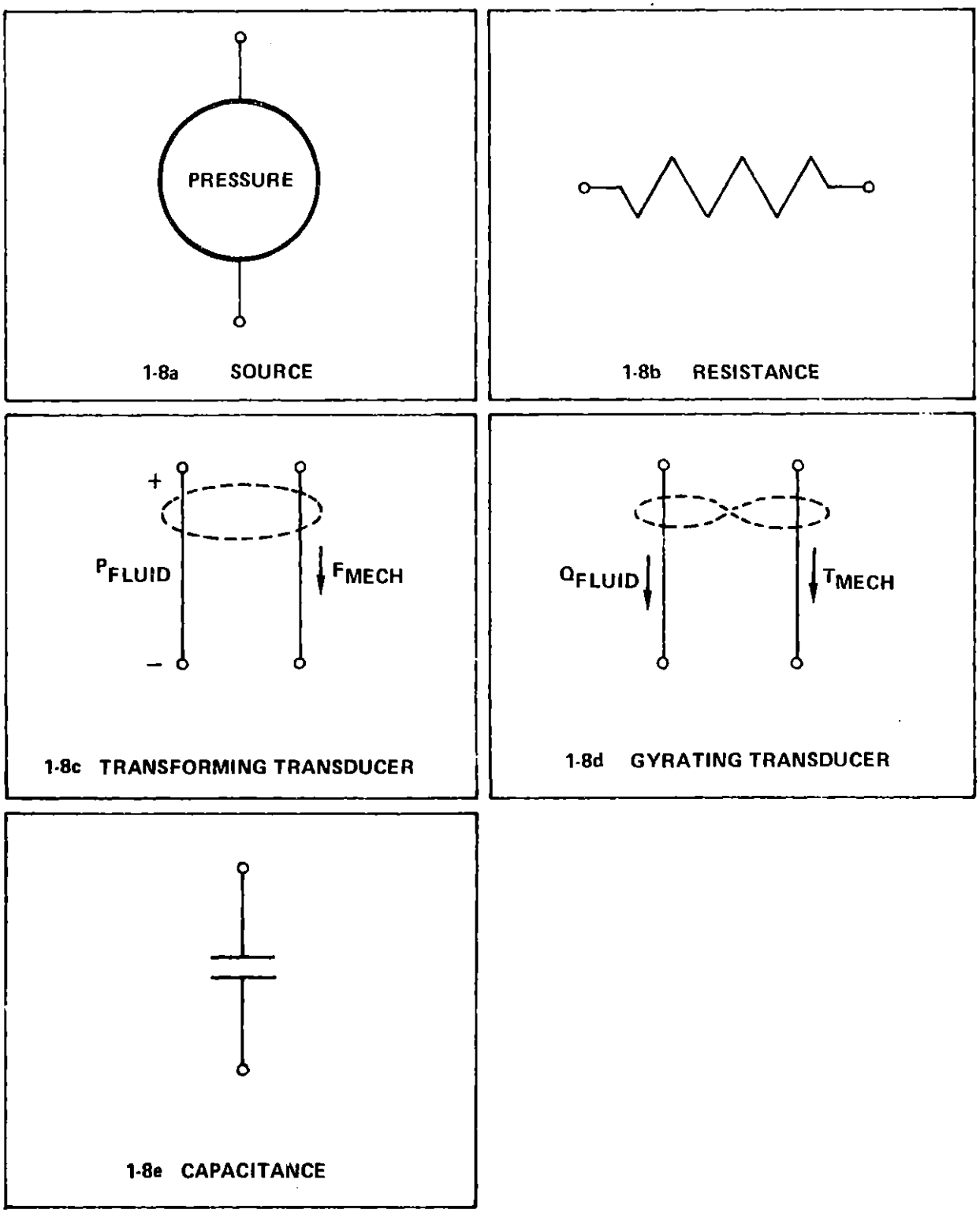

Figure 1-8. Symbols for Various Fluid Elements[1*]

*Superscript numerals refer to references at end of work.

1.2.2 Resistances

There are some elements in the system which serve to dissipate fluid power and thus may be termed fluid resistances. There is a pressure drop across the sill of a suspension pad. Flow through a filter or through an orifice experiences a pressure drop in the direction of flow, also. Because of this pressure loss the sills, orifices, filters, and piping of the hydraulic system have been modeled as fluid resistances. The symbol to be used for a resistor is shown in Figure 1-8b. Its resemblance to the symbol for an electrical resistor is intentional; both fluid and electric resistors are analogous in that they both dissipate power. Unlike the electrical counterpart, however, the fluid resistances do not have a simple proportionality between the pressure loss and flow but rather are highly nonlinear. An expression for each of these is derived in Chapter 2.

1.2.3 Suspension Pads

The suspension pads of the fluid system provide a support force through the integration of the pressure distribution across the pad surface. Since they convert a fluid effort variable, pressure, P_{fluid} to a mechanical effort variable, force, F_{mech} the pads can be called transforming transducers. They provide the coupling between the fluid and mechanical aspects of the system which control radial translational motions of the inner sphere. The symbol to be used for a transforming tranducer is indicated in Figure 1-8c. The loop indicates the coupling between the effort variables of both systems.

1.2.4 Torquer Jets

The torquer jets spin the ball through the reaction force produced by expelling a high flow rate (i.e., high velocity) fluid stream from a nozzle. The torques T_{mech} resulting in the mechanical rotary motion of the system are a direct consequence of the high fluid flow rate Q_{fluid}. Since this subsystem converts a flow variable in the fluid system, to an effort variable in the mechanical system, it may be modeled as a gyrating transducer. The symbol which will be used for a gyrating transducer is illustrated in Figure 1-8d. The crossed loop indicates the cross coupling between the effort and flow variables of the fluidic and mechanical systems.

1.2.5 Mechanical Aspects

The modeling of the fluidic parts of the system are important in their relation to the system's mechanical aspects. The ball itself may be modeled as a lumped mass. For translational purposes it has an effective mass, M_{eff}. It has rotary moments of inertia J about its spin axes. The ball's inertances to both translational and rotary motions are modeled by mechanical capacitances. The symbol for a mechanical capacitance is illustrated in Figure 1-8e. The symbol reflects the ball's similarity to an electrical capacitance. Just as in the electric circuits a capacitor resists instantaneous changes of voltage, a mass resists instantaneous changes of linear and angular velocities.

1.2.6 Outside Disturbances

The ball-case system is subjected to two forms of outside disturbances. The entire system may be exposed to a linear acceleration. This disturbance is modeled as a velocity source. Rotary disturbances are present also; they are modeled by an angular velocity source. The symbol for a source was given in Figure 1-8a.

1.2.7 System Circuit

Figure 1-9 shows a schematic of the modeling used for the system. The fine lines indicate the hydraulics of the system. The heavy solid lines represent the translational mechanical aspects of the ball and the dashed heavy lines, the rotational features. The advantage of displaying the system in the form of an electric analog is that the pathways of fluid flow can be seen by imagining where the current would flow if Figure 1-9 were really an electric circuit. Elements with a common pressure differential or common velocity are pictured as parallel circuits.

To better understand the system we will trace the fluid path through the circuit. Flow begins at the high pressure side of the pump at the far left. The flow divides, part of it going to support the axial thrust bearings of the pump rotor, the remainder heading out along eight pathways to he corners of the imaginary cube. There is a pressure drop along each of these pathways. When the flow is just beneath the outer surface of the sphere it divides again. Six pathways feed one suspension pad and one half of each of two valves; two pathways feed one pad only as explained in "Piping to Subsystems" (1.1.3).

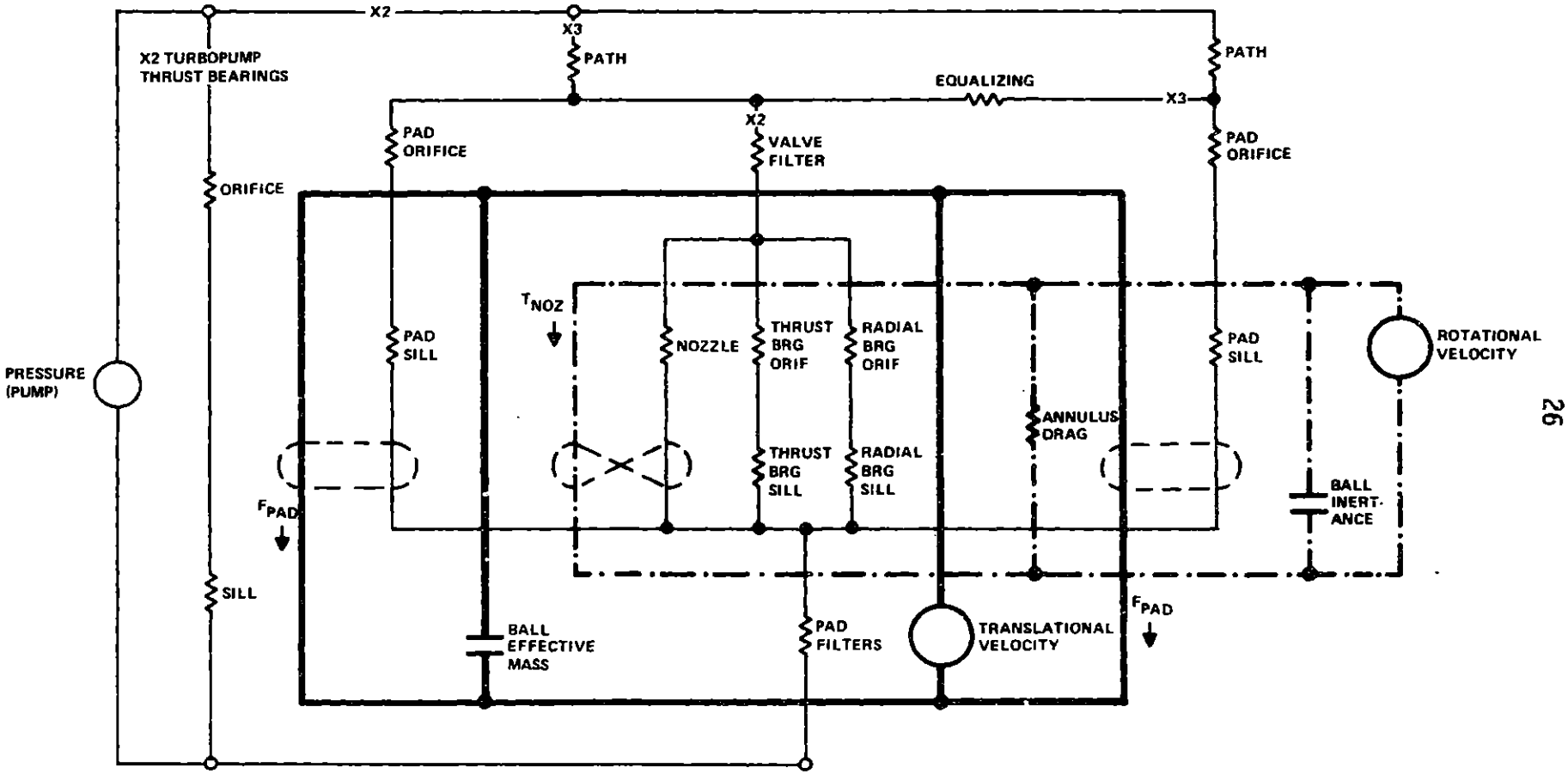

Figure 1-9. Hydraulic Circuit with Coupling to Suspension and Torquing Subsystems

The pad flow passes through an orifice and across a sill before entering the annulus. The valve flow, after passing through a filter divides between the nozzle and bearing mechanisms of the nozzle operation. The flow which reaches the annulus via the nozzle then rejoins the pad flow and the total flow then returns to the low pressure side of the pump after passing through twenty-four pad filters clustered in groups of three about each pad.

The translational section of the circuit is composed of a velocity source and a force source (the pads) acting on a mass (the ball). The rotational section has a source of rotational velocity (the outer case) and a torque source (the nozzles) acting to rotate a mass (the ball) and rotary damper (annular drag). This circuit and the interactions between its various sections was used as a guide in the calculations of later chapters.

1.3 Organization of Paper

To analyze a system as large as described, a logical path throughout the system is necessary. This report proceeds "from the inside to the outside". Analysis begins in Chapter 2 with a calculation of the various losses accrued in transporting fluid to the two subsystems, translational and rotational. Once at the outer surface of the ball, Chapter 3 examines the suspension system. Chapter 4 then examines the losses due to outer surface geometry and presents an analysis of the torquing system. Once the power requirements needed to get the fluid from the center of the ball to the outer surface where it is utilized and the power needed for suspension and torquing are known, the report then returns to examine the pump necessary to achieve these tasks. Chapter 5 studies the pump itself.

CHAPTER 2

CALCULATION OF RESISTANCES

2.1 Sill Resistances[2]

The turbopump thrust bearings and servo valve bearings as well as the suspension pads contain sills which experience pressure drops. An analysis of a typical sill should be applicable to all three cases.

Consider a circular pad and plenum as shown in Figure 2-1. Notation is as follows:

r_o	radius of orifice
r_p	radius of plenum
d	depth of plenum
r_s	outer radius of sill
h	pad clearance
h_o	mean pad clearance
ε	tilt
θ	position on pad

Inspection of Figure 2-1 yields the following relationship for the pad clearance

$$h(r, \theta) = h_o + \varepsilon \frac{r}{r_s} \cos \theta \qquad (2\text{-}1)$$

To simplify this relationship let us assume clearance variations across the sill are much less than those around the sill, i.e.,

$$\frac{dh}{dr} \ll \frac{dh}{d\theta} \qquad (2\text{-}2)$$

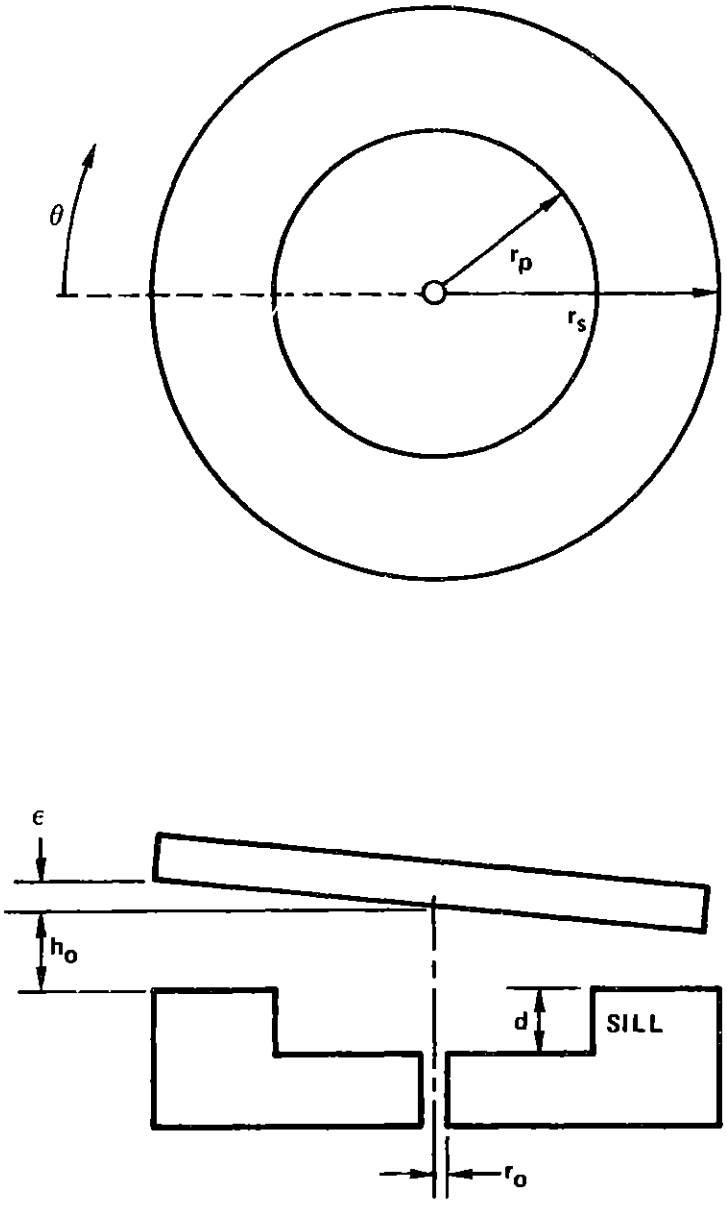

Figure 2-1. Suspension Pad Illustrating Sill and Plenum Regions

This assumption enables us to write the pad clearance as a function of θ only, r being replaced by average of the inner and outer sill radii

$$h(\theta) = h_o + \frac{\varepsilon}{r_s}\left(\frac{r_s + r_p}{2}\right)\cos\theta \tag{2-3}$$

To obtain the pressure drop across the sill we must look at the equilibrium of a small wedge of fluid between the sill and the lid. If the width of the sill is much less than its length (mean circumference) we may approximate our wedge as a rectangle. Figure 2-2 shows approximations made.

The preceding assumptions have reduced the wedge to a rectangular segment which may be envisioned as a small section of a channel in Pouiseuille flow. For this case the volume flow rate per unit depth q is given by

$$q = -\frac{h^3(\theta)}{12\mu}\frac{dp}{dr} \tag{2-4}$$

where μ is the fluid viscosity and $\frac{dp}{dr}$ is the radial pressure gradient. The volume flow rate per unit area for one section may also be given by

$$q = \frac{dQ_{sill}}{rd\theta} \tag{2-5}$$

where Q_{sill} is the total flow across the pad sill. Upon substitution the following relationship for the radial pressure gradient is obtained

$$\frac{dp}{dr} = \frac{-12\mu\, dQ_{sill}}{h^3(\theta)\, rd\theta} \tag{2-6}$$

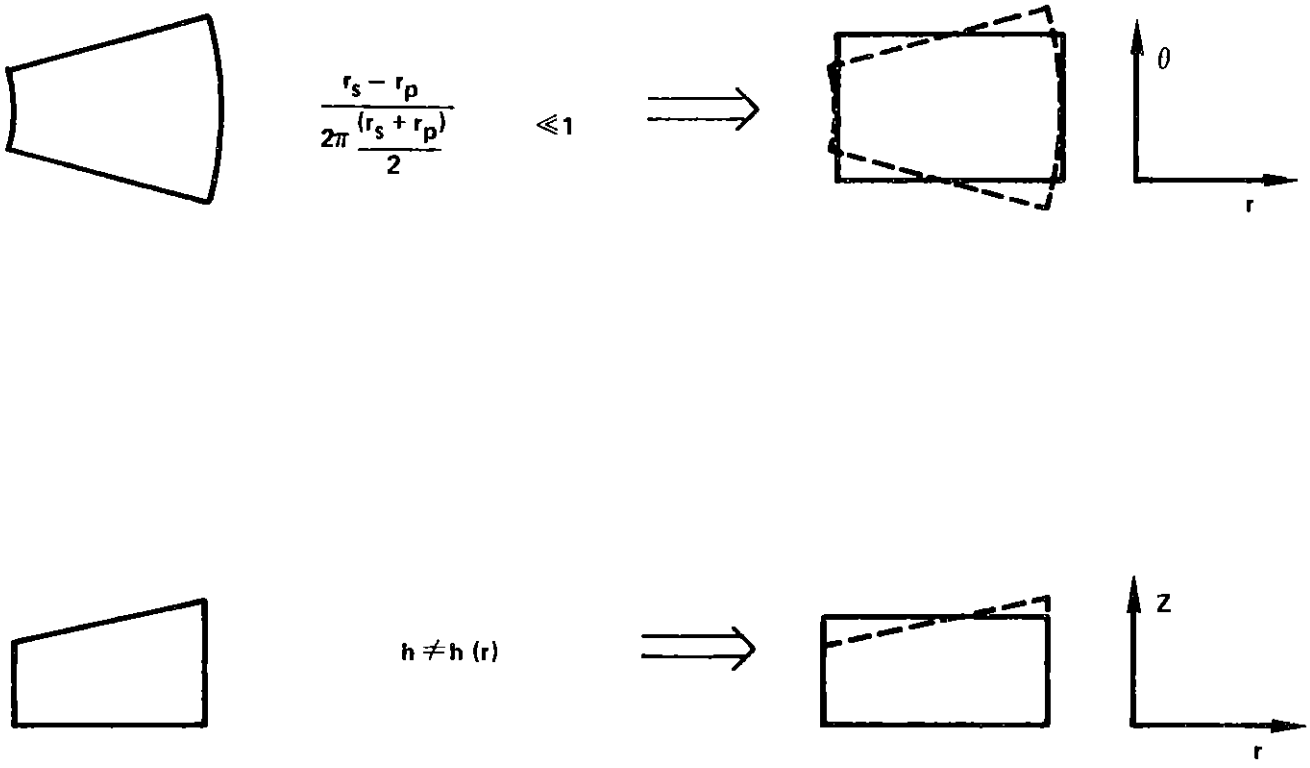

Figure 2-2. Sill Geometric Approximations Changing Tilted Circular Wedge to Rectangular Segment

Separation of variables and integration of the above equaion between r_p and r_s yields

$$P(r_p) - P(r_s) = \frac{12\mu}{h^3(\theta)} \ln \frac{r_s}{r_p} \quad \frac{dQ_{sill}}{d\theta} \tag{2-7}$$

A second integration obtains the total flow rate Q_{sill}

$$Q_{sill} = \frac{P(r_p) - P(r_s)}{12\mu \ln\left(r_s/r_p\right)} \int_0^{2\pi} h^3(\theta)\, d\theta \tag{2-8}$$

Substituting equation (2-3) for $h(\theta)$ and integrating gives the relation

$$\int_0^{2\pi} h^3(\theta)d\theta = 2\pi h_o{}^3 + 3\left[\frac{\varepsilon}{r_s}\left(\frac{r_s + r_p}{2}\right)\right]^2 h_o\pi \tag{2-9}$$

A final substitution of equation (2-9) into equation (2-8) gives the results

$$Q_{sill} = \frac{P(r_p) - P(r_s)}{12\mu \ln\left(r_s/r_p\right)} 2\pi h_o{}^3 \left\{ 1 + \frac{3}{2}\left[\frac{\varepsilon}{2h_o}\left(1 + \frac{r_p}{r_s}\right)\right]^2 \right\} \tag{2-10}$$

or alternatively the pressure drop across the sill $P(r_p)$-$P(r_s)$ is given by

$$P(r_p) - P(r_s) = \frac{6\mu \ln\left(r_s/r_p\right)}{\pi h_o{}^3 \left\{ 1 + \frac{3}{2}\left[\frac{\varepsilon}{2h_o}\left(1 + \frac{r_p}{r_s}\right)\right]^2 \right\}} Q_{sill} \tag{2-11}$$

For zero tilt the pressure drop is inversely proportional to the cube of the gap; any tilt tends to reduce this pressure drop. The hydraulic power lost across this sill is given by the product of the flow and pressure drop across the sill

$$P_{sill} = \left[P(r_p) - P(r_s)\right] Q_{sill} = \frac{6\mu \ln\left(r_s/r_p\right)}{\pi h_o^3 \left\{1 + \frac{3}{2}\left[\frac{\epsilon}{2h_o}\left(1 + \frac{r_p}{r_s}\right)\right]^2\right\}} Q_{sill}^2 \quad (2\text{-}12)$$

2.1.1 Numeric Applications

Having been derived, the above relationships describing system pressure drops due to the presence of sills, will be applied to each of the four sill geometries found in the hydraulic subsystem. Each one has a picture illustrating the geometry involved and a list of parameter values followed by plotted conclusions.

2.1.1.1 Pressure Drop Across Suspension Pad Sills

There are eight suspension pads on the outer surface of the inner sphere. The eccentricity of the ball itself determines the gap of each padand its corresponding resistive pressure drop. Pad geometry is shown in the upper right corner of Figure 2-3. Values used in the computations were

r_s = .475 in. $\qquad$ r_p = .475 in.

μ = 2.077 x 10^{-7} lb-sec/in.^{2}

Figure 2-3 plots the pad fluid resistance

$$\frac{P(r_p) - P(r_s)}{Q_{sill}}$$

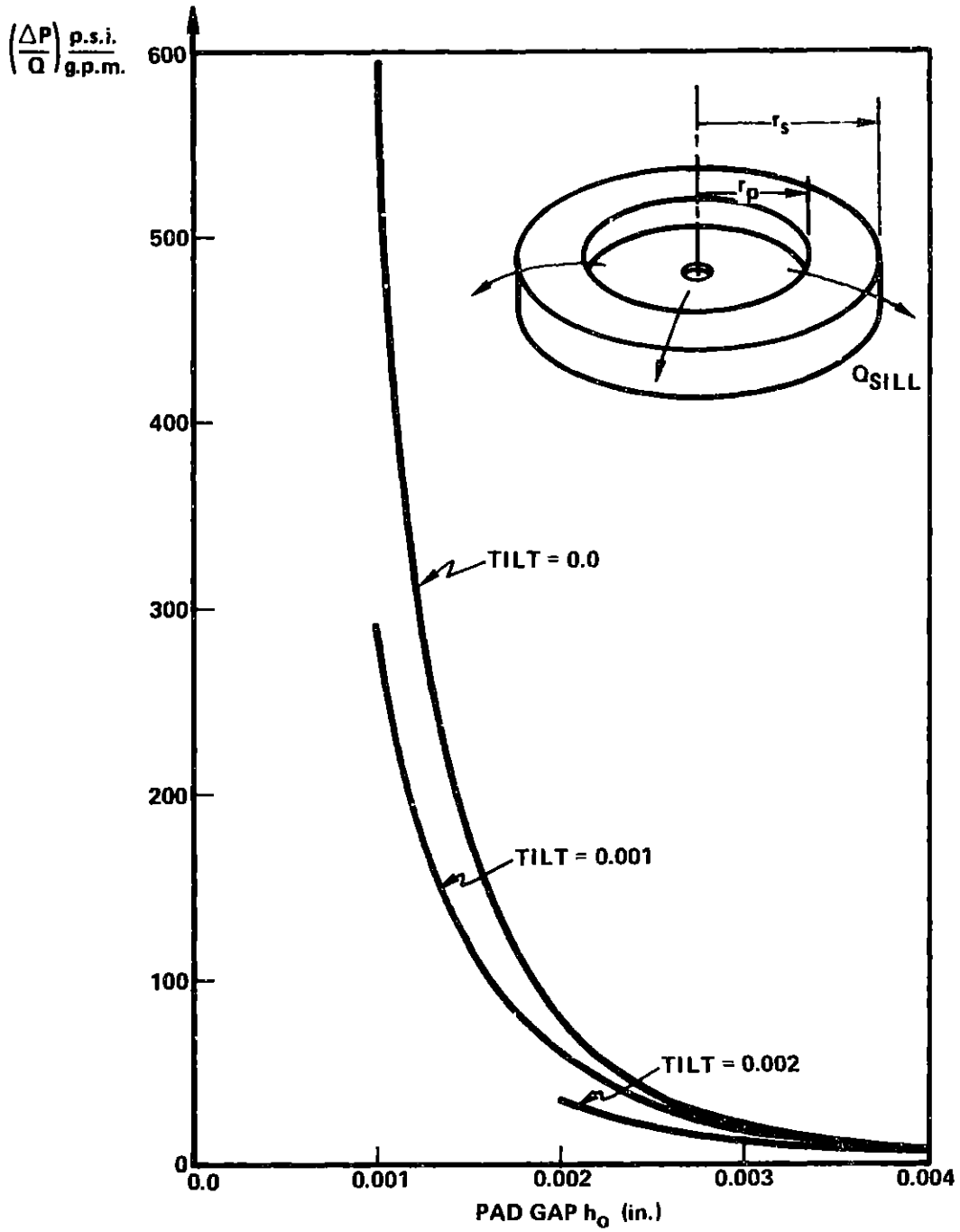

Figure 2-3. Suspension Pad Sill Resistance Versus Pad Gap

as a function of pad gap for tilt values of 0.0, .001, and .002 in. Tilt serves to decrease the pressure differential across the sill. Although this occurrence is favorable from a resistance point of view, it is this integrated pressure gradient which supplies necessary support forces. Tilt thus decreases the available suspension pad force. (See section 3.1.)

2.1.1.2 Pressure Drop Across Turbopump Thrust Bearing Sills

The turbopump thrust bearings are configured such that they have two sills. The bearing is pictured in the upper right corner of Figure 2-4. The resistance across the inner sill

$$\frac{P(r_1) - P(r_0)}{Q_{sill}}$$

and the outer sill

$$\frac{P(r_2) - P(r_3)}{Q_{sill}}$$

are plotted in Figure 2-4. Note that a positive flow across the sill is radially outward and therefore in calculations the flow across the inner sill must be considered negative. The pertinent parameter values were

r_0 = .188 in. r_1 = .360 in.

r_2 = .200 in. r_3 = .375 in.

μ = 2.077×10^{-7} lb-sec/in. ε = 0.0

2.1.1.3 Pressure Drop Across Valve Thrust Bearing Sills

The valve thrust bearing sills differ from the previous two types only in that there is no plenum region. Flow leaks directly into the sill area and radially outward. Figure 2-5 illustrates the bearing in the upper right corner and plots the pressure drop at flow rates ranging from 0.0 to .01 gpm. The slope of the graph is the sill resistance $\frac{\Delta P}{Q}$.

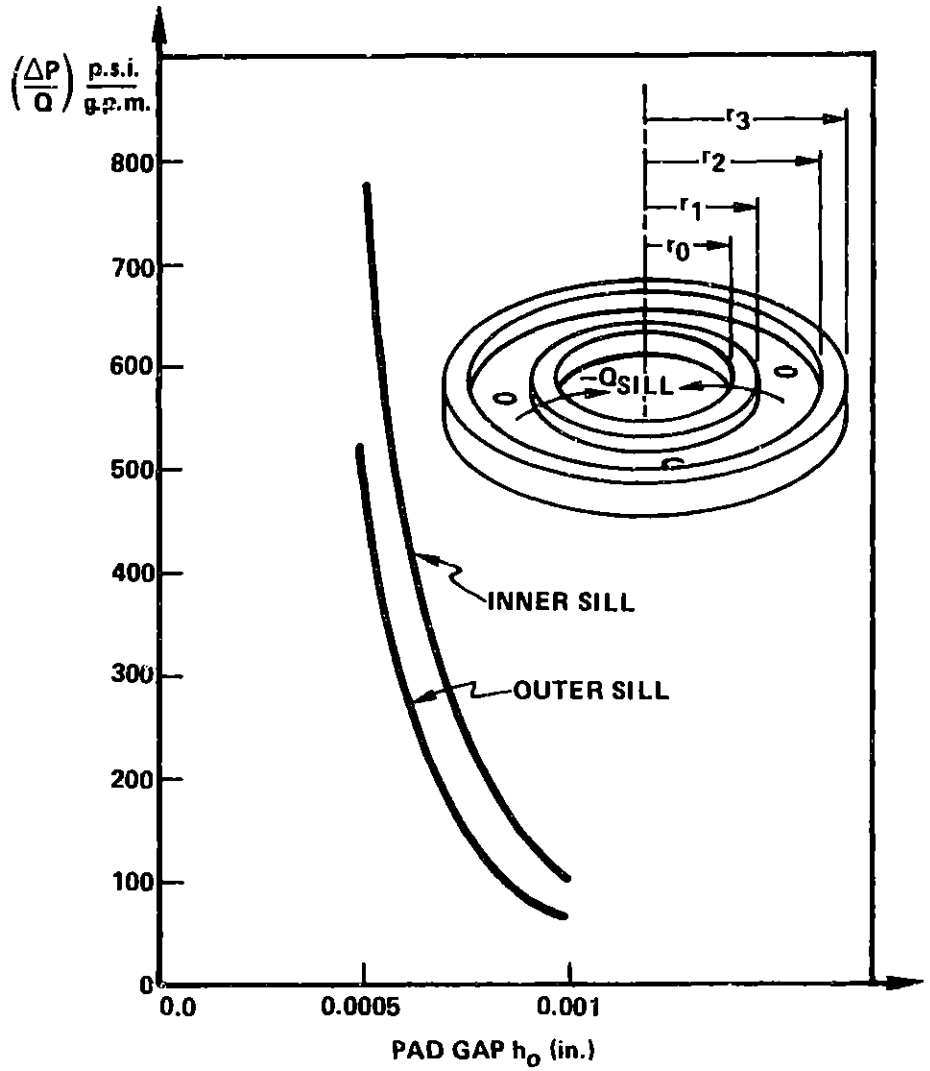

Figure 2-4. Turbopump Thrust Bearing Sill Resistance Versus Pad Gap

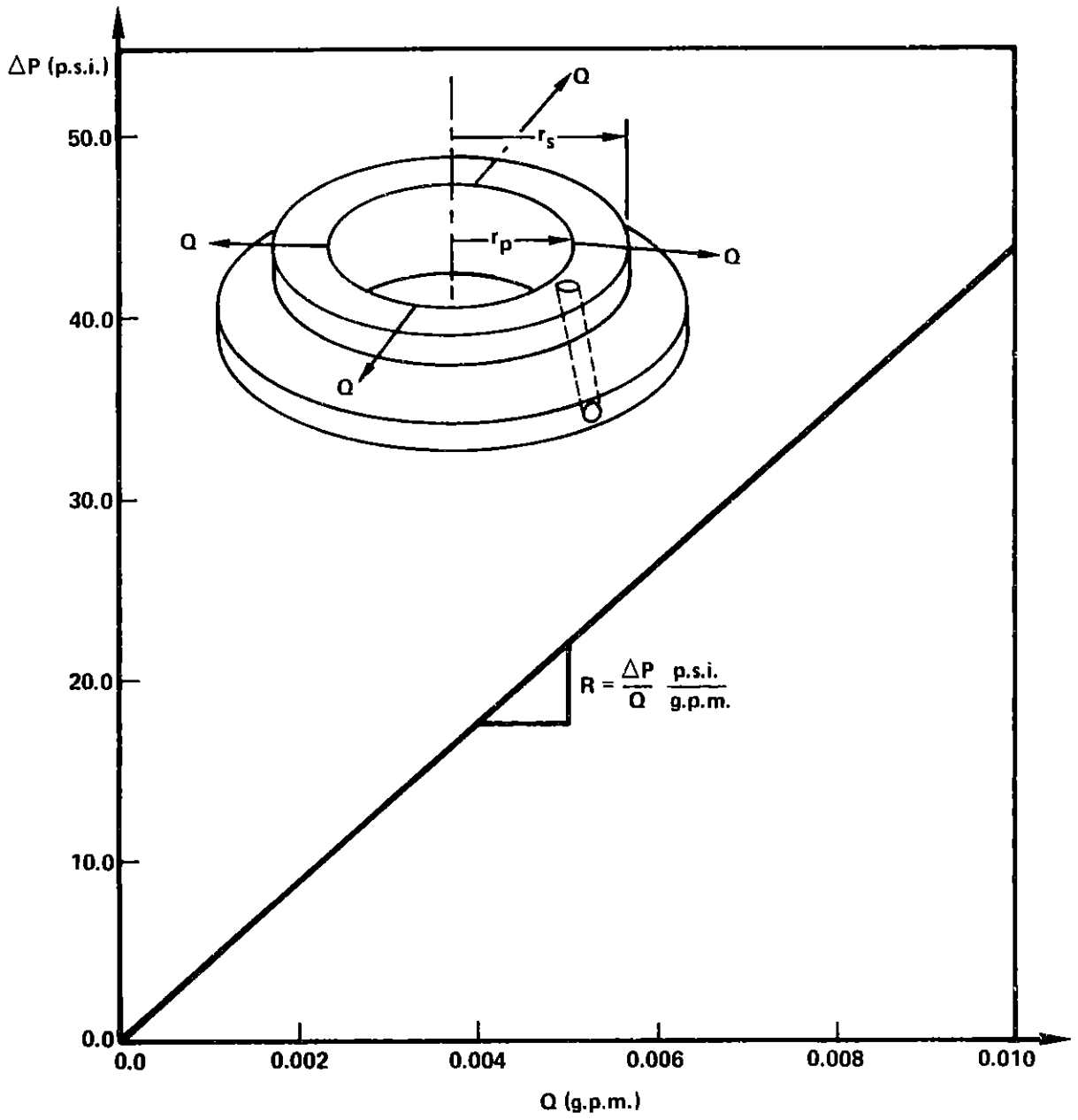

Figure 2-5. Pressure-Flow Characteristic of Valve Thrust Bearing Seal

For the dimensions listed below this particular bearing's resistance was 4.38×10^3 psi/gpm.

$r_p = .126$ in. $\qquad r_s = .180$ in.

$\mu = 2.077 \times 10^{-7}$ lb-sec/in.^{2}

A constant gap of .0005 in. and zero tilt conditions were assumed.

2.1.1.4 Pressure Drop Across Valve Radial Bearing Sills

The valve radial bearings, unlike the three previous sill designs, have a rectangular rather than circular geometry. Three rectangular plenums are "wrapped" circumferentially about the valve rotor at either end. The same basic formulas, however, may be applied with slight modifications. Instead of a radial flow, fluid flow is assumed to occur only perpendicular to the long side of the rectangular plenum, i.e., along the axis of the rotor. (See Figure 2-6.)

The flow across the pad sill is assumed to be Poiseuille flow as before and the gap b is modeled as the gap between two parallel plates. Parallelism is a valid simplification here since the gap b is much much less than the radius of curvature of the rotor. The equation for this type of flow is

$$Q_{sill} = \frac{wb^3}{12\mu}\left(\frac{dp}{dx}\right) \qquad (2\text{-}13)$$

where Q_{sill} is the flow across the sill, w is the width of the sill normal to the flow direction, b is the sill clearance, μ is the fluid viscosity, and $\frac{dp}{dx}$ is the pressure gradient in the direction of fluid flow. The upper portion of Figure 2-7 illustrates these quantities.

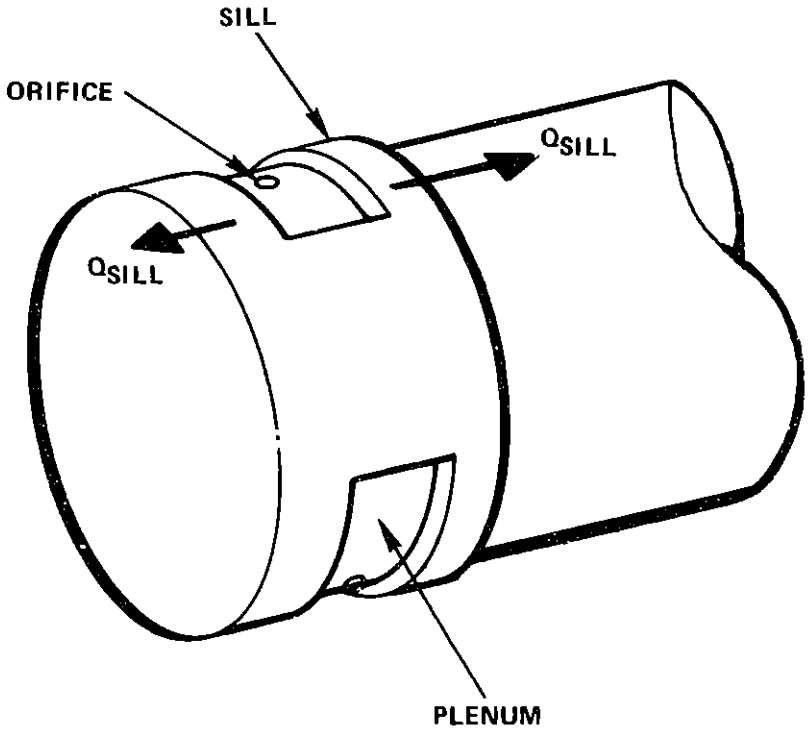

Figure 2-6. Valve Radial Bearing Configuration Illustrating Sill and Plenum Regions

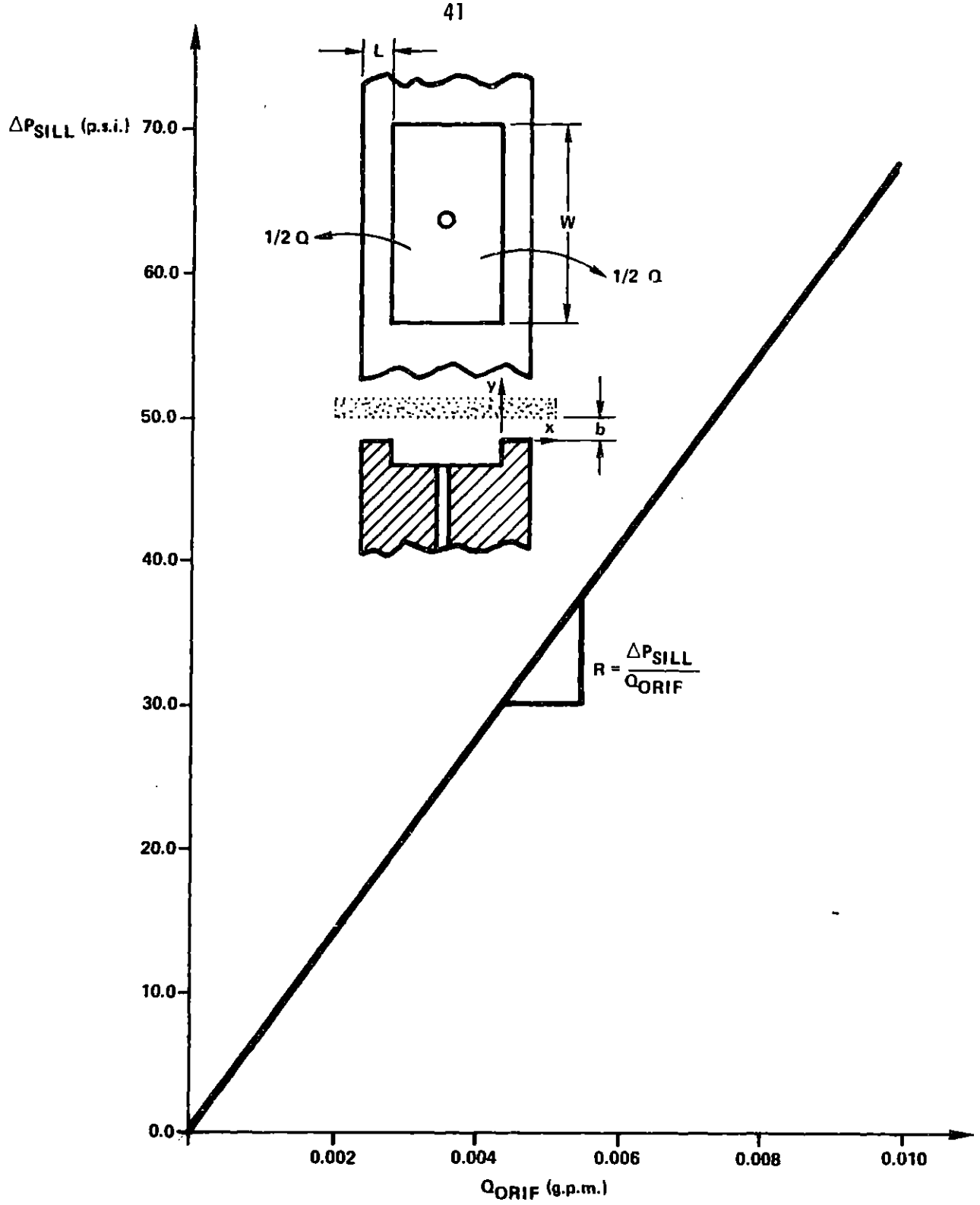

Figure 2-7. Pressure-Flow Characteristic of Valve Radial Bearing

Integration of equation (2-13) across the length of the pad sill (x = 0 to L) gives

$$\Delta P = \frac{12\mu}{wb^3} L\, Q_{sill} \qquad (2\text{-}14)$$

From symmetry arguments it can be seen that the flow across one sill is one half the orifice flow Q_{orif} so the pressure drop can be written as

$$\Delta P = \frac{6\mu}{wb^3} L\, Q_{orif} \qquad (2\text{-}15)$$

The resistance of two sills $\frac{\Delta P}{Q_{sill}}$ can be found by substituting the values listed below:

w = .17 in. b = .0005 in.

L = .03 in. $\mu = 2.077 \times 10^{-7}$ lb-sec/in.^{2}

The resistance of the radial valve bearings is

$$R = 6.75 \times 10^3 \text{ psi/gpm}$$

The flow characteristics of the bearing are plotted in Figure 2-7.

2.2 Orifice Resistances

The turbopump thrust bearings, suspension pads, and servo valves all contain orifice losses. Calculations of these losses can proceed by applying Bernoulli's equation on a streamline through the orifice between points on either side. Note from Figure 2-8 that fluid emerging from the orifice will have a smaller cross sectional area than the orifice and thus an increased velocity.

$$P_1 + \frac{\rho V^2_{ideal}}{2} = P_2 + \frac{\rho V^2_{orif}}{2} \tag{2-16}$$

or

$$P_1 - P_2 = \frac{\rho}{2}\left(V^2_{orif} - V^2_{ideal}\right)$$

The actual velocity may be written as a contraction coefficient times the ideal velocity ($V_{orif} = c_v V_{ideal}$). Substituting this relation into equation (2-16) gives

$$P_1 - P_2 = \frac{\rho}{2} V^2_{orif}\left(1 - \frac{1}{c_v^2}\right) \tag{2-17}$$

A differential pressure ΔP is defined as $P_2 - P_1$. The actual flow rate is given by the reduced area orifice, $Q_{orif} = c_c A_o V_{orif}$, where c_c is a contraction coefficient for the orifice area. Substituting these relations into equation (2-17) gives

$$\Delta P = \frac{\rho}{2}\left(\frac{1}{c_v^2} - 1\right)\frac{Q^2_{orif}}{c_c^2 A_o^2} \tag{2-18}$$

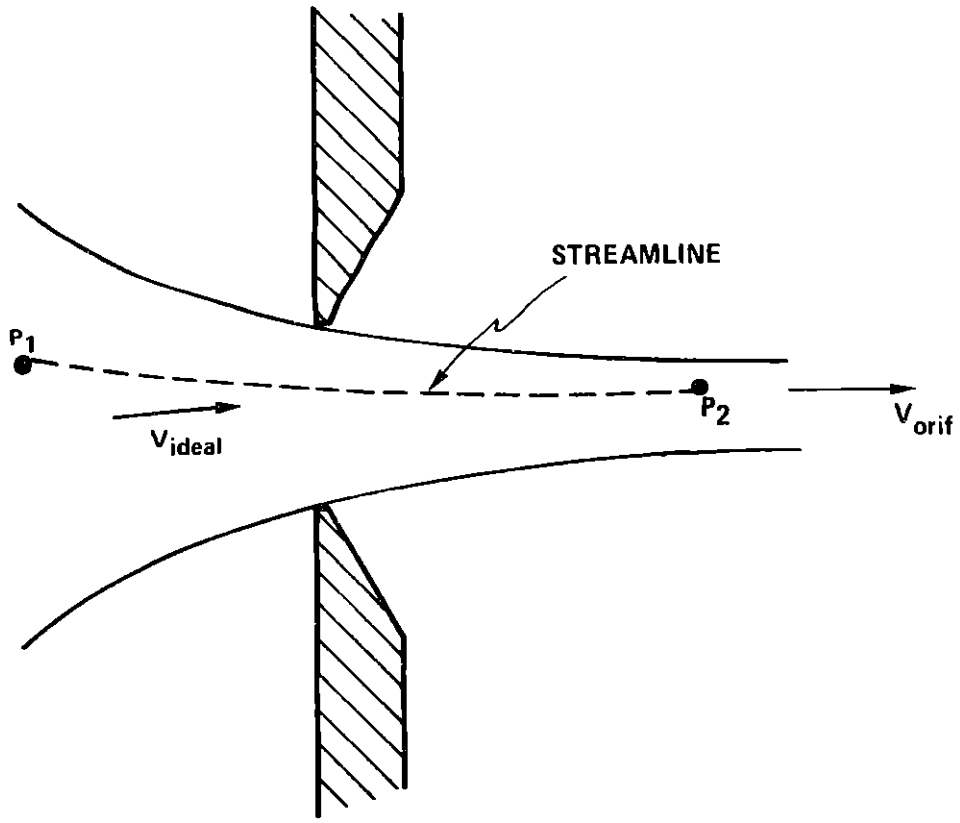

Figure 2-8. Flow Through a Sharp Edged Orifice

The coefficients c_c and c_v have been determined empirically in many fluid texts. One need only know the orifice geometry. Some examples are given in Figure 2-9.[3]

The resistance for an orifice may be defined as $R_{orif} = \frac{\Delta P}{Q^2_{orif}}$ or, in terms of system geometry,

$$R_{orif} = \frac{\rho}{2}\left(\frac{1}{c_v^2} - 1\right)\frac{1}{c_c^2 A_o^2} \tag{2-19}$$

The hydraulic power lost across an orifice is given by the product of the pressure difference and flow or since $\Delta P = R\, Q^2_{orif}$ the power P is given by

$$P = R\, Q^3_{orif} = \frac{\rho}{2}\left(\frac{1}{c_v^2} - 1\right)\frac{1}{c_c^2 A_o^2}\, Q^3_{orif} \tag{2-20}$$

2.2.1 Numeric Applications

Some of the various orifices found in this hydraulic system are pad orifices, turbopump thrust bearing orifices, nozzle orifices, and valve radial and thrust bearing orifices. Figure 2-10 pictures a few of these orifices, the values for c_c and c_v assumed, and the resistances calculated. All orifice calculations assume a fluid density of 1.675×10^{-4} lb-sec^2/in.^{4}.

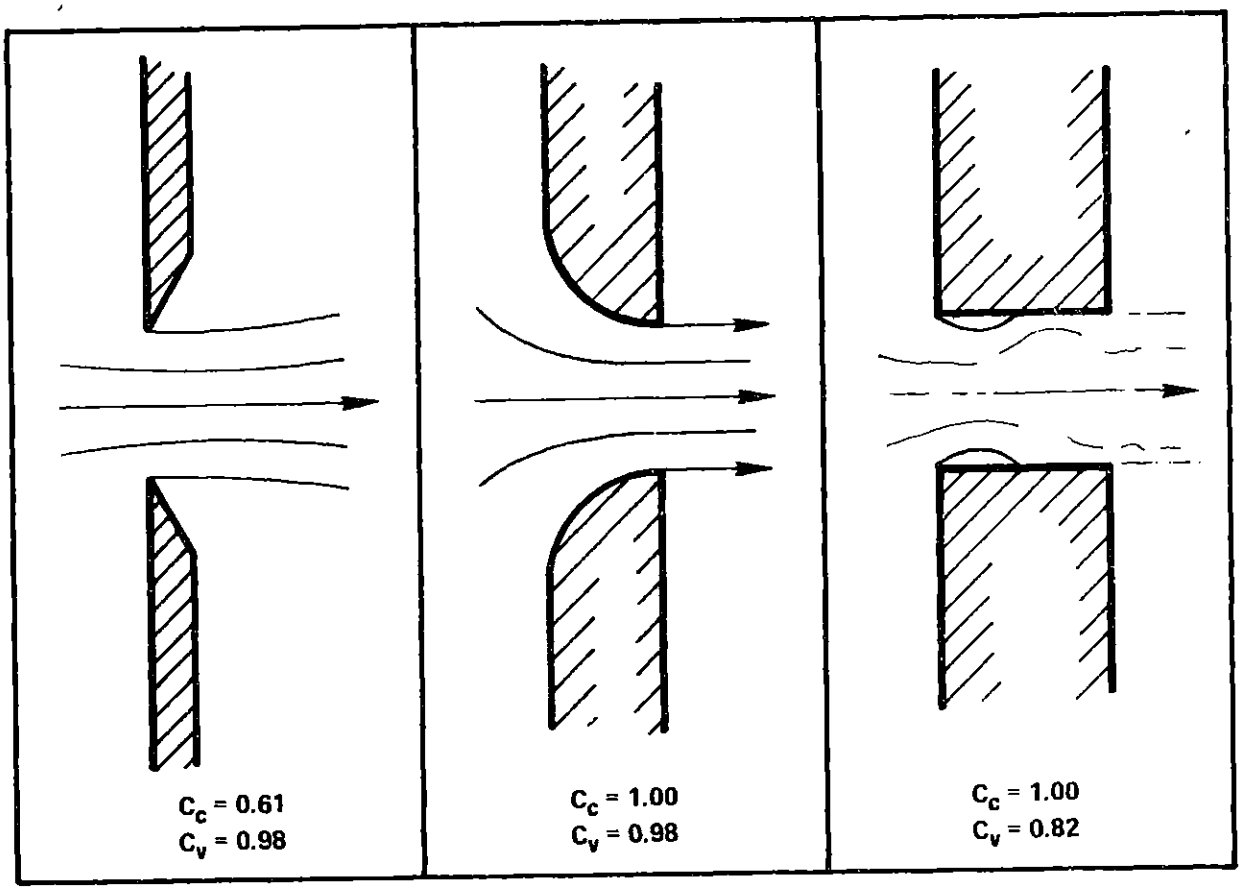

Figure 2-9. Flow Through Various Types of Orifices. Typical Values of Velocity and Contraction Coefficients are Noted for Each Type

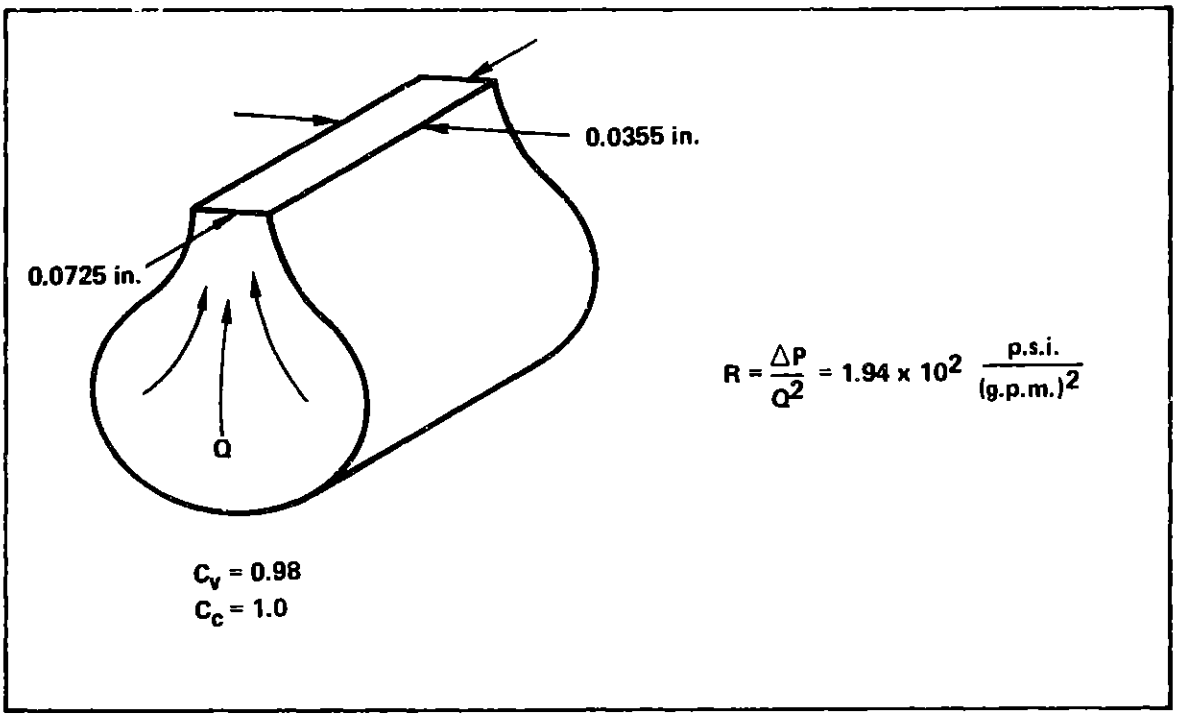

NOZZLE ORIFICE

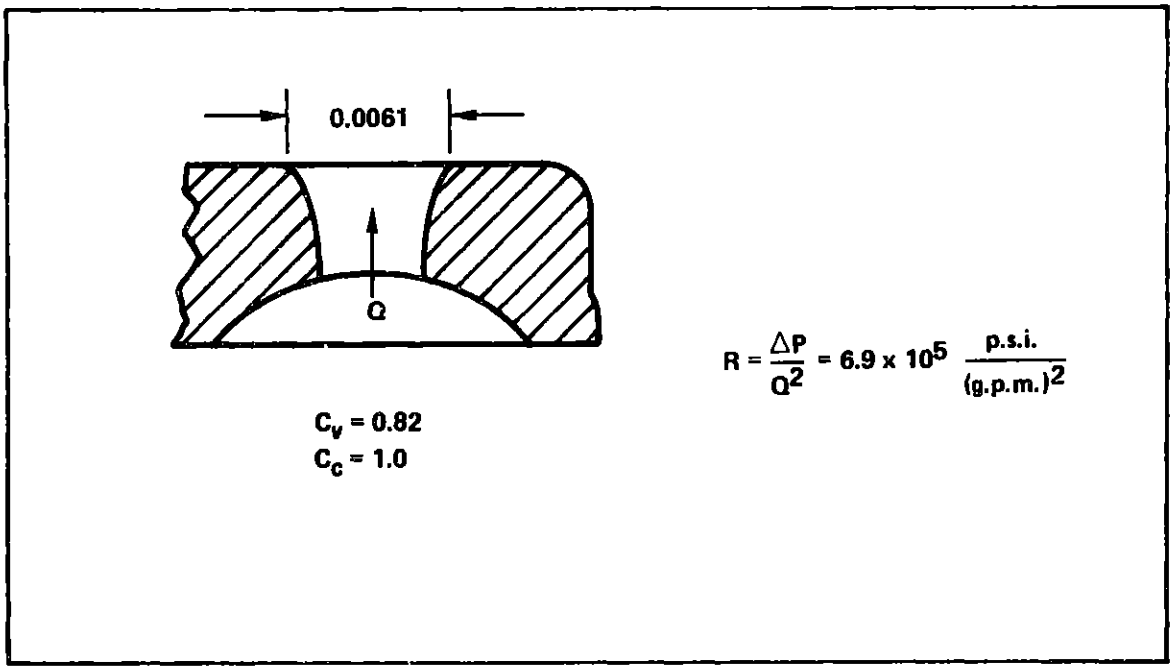

VALVE RADIAL BEARING ORIFICE

Figure 2-10. Typical Orifices Found in System with Associated Velocity and Contraction Coefficients

2.3 Inner Piping Losses

The previous sections analyzed pressure drops experienced by various system components due to sills, orifices, etc. There are pressure drops along the way to these components as well due to frictional losses along the inner piping. The major contributors to these pathway losses are the eight radial passages which transport the fluid to the pads and valves. This section calculates the magnitude of these fluid resistances.

Before trying to estimate any fluid viscous loss we must determine first whether the flow is laminar or turbulent. Pressure losses in a laminar flow are proportional to the volumetric flow rate Q. In turbulent flow the pressure loss ΔP varies roughly as Q^2. The determination of the exact transition point from laminar to turbulent flow is almost impossible to do analytically since it is a function of surface roughness, initial flow disturbances and many other variables. Experiments have shown, however, that a good estimate for the laminar to turbulent flow transition in pipes is when a nondimensional flow parameter, called the Reynold's number Re, is roughly 2000. The Reynold's number for pipe flow is based on the pipe diameter D and is given by

$$Re = \frac{VD}{\nu} \tag{2-21}$$

where V is the average fluid velocity through the pipe and ν is the fluid kinematic viscosity. Flows with a Reynold's number of 2000 or less are laminar; those with Re greater than 2000 are turbulent.

The eight radial pathways do not have circular cross sections so a problem arises as to the definition of the Reynold's number. To account for this discrepancy, an equivalent hydraulic radius R_h is calculated which is the ratio of the cross sectional area A to the wetted perimeter P_{wetted} of the pipe. A cross section of a radial path is shown in Figure 2-11 with pertinent dimensions. A cross sectional area of .004 $in.^2$ and a wetted perimeter of .893 in. gives for the hydraulic radius

$$R_h = \frac{A}{P_{wetted}} = .049 \text{ in.} \tag{2-22}$$

The Reynold's number based on the hydraulic radius is then given by

$$Re = \frac{Q}{A} \frac{4R_h}{\nu} \tag{2-23}$$

where $\frac{Q}{A}$ has been substituted for the average fluid velocity V. It can be shown that four times the hydraulic radius does indeed simplify to the pipe diameter for pipes of circular cross section.

The pressure drop ΔP along a pipe is given by

$$\Delta P = f \frac{L}{4R_h} \frac{\rho Q^2}{2A^2} \tag{2-24}$$

where L is the pipe length and ρ the fluid density. The multiplicative factor f is known as the friction factor. It is a function of the Reynold's number. For laminar flow

$$f = \frac{64}{Re} \tag{2-25}$$

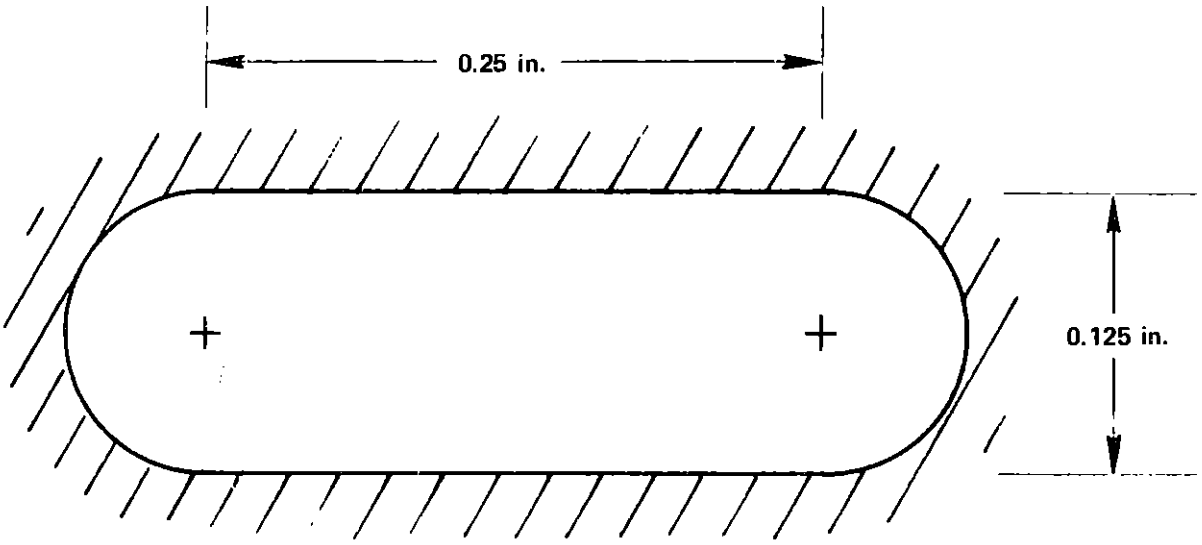

$$A = (0.25)(0.125) + \frac{\pi}{4}(0.125)^2 = 0.044 \text{ in}^2$$

$$P_{WETTED} = 2(0.25) + \pi(0.125) = 0.893 \text{ in.}$$

Figure 2-11. Radial Path Cross Section. Area and Wetted Perimeter are Calculated

and for turbulent flow

$$f = \frac{.3164}{Re^{.25}} \qquad (2\text{-}26)$$

In calculating pressure drop one must first determine if the flow is laminar or turbulent. The critical flow for these paths (that at which Re = 2000) is about .14 gpm. The pressure flow characteristic is shown in Figure 2-12. The pipe length used for those calculations was 4 in. The discontinuity at Q = .14 gpm is due to the uncertainty during the transition period. It causes no problems, however, because this system operates totally within the turbulent regime of the radial paths.

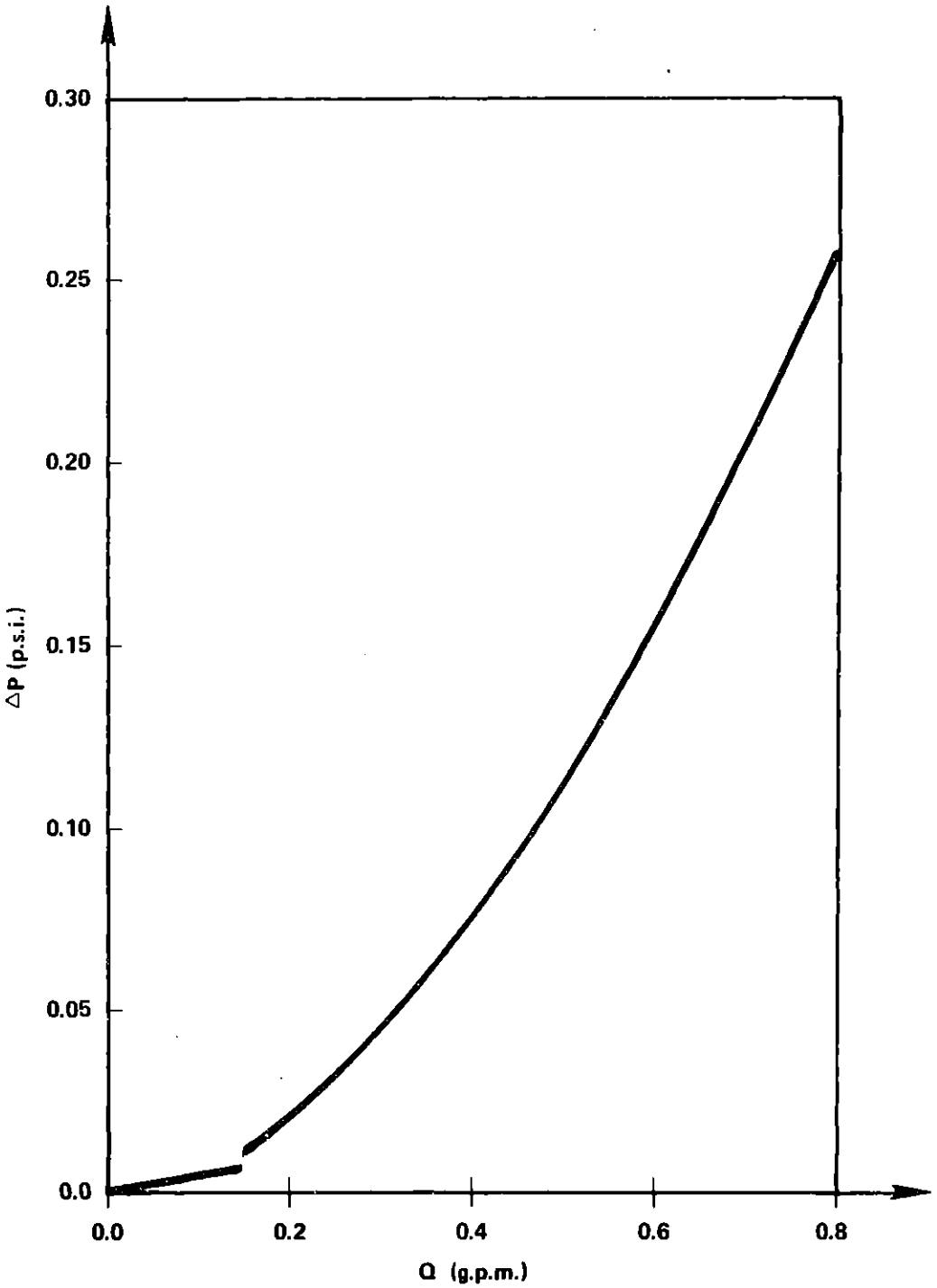

Figure 2-12. Radial Path Pressure-Flow Characteristic

2.4 Filter Resistances

There is a pressure drop ΔP experienced as the fluid flows through a filter. To calculate the filter's resistance to flow some assumptions are necessary. Let us visualize a filter as a thin sheet with cylindrical holes through it with diameters equal to the particle retention size of the filter P and lengths equal to the filter thickness t. (See Figure 2-13.) Looking at one hole a force balance is done between the pressure and viscous forces

$$\Delta P \frac{\pi p^2}{4} = \tau \pi p t \tag{2-27}$$

The shear stress τ can be related to the fluid velocity through the hole V_{hole} and the density ρ of the fluid via a coefficient of friction C_f

$$\tau = C_f \frac{\rho V^2_{hole}}{2} \tag{2-28}$$

Substitution of this relation into equation (2-27) yields

$$\Delta P = 4C_f \frac{\rho V^2_{hole}}{2} \frac{t}{p} \tag{2-29}$$

The fluid velocity through the holes needs to be determined. From continuity considerations and assuming an incompressible fluid the following relationship between the hole area A_{hole} and pipe area A_{pipe} and pipe velocity V_{pipe} is obtained

$$V_{hole} = \frac{A_{pipe}}{\Sigma A_{hole}} V_{pipe} \tag{2-30}$$

The hole area may be represented by a porosity or "percentage holes" coefficient ξ times the pipe area.

$$\Sigma A_{hole} = \xi A_{pipe} \tag{2-31}$$

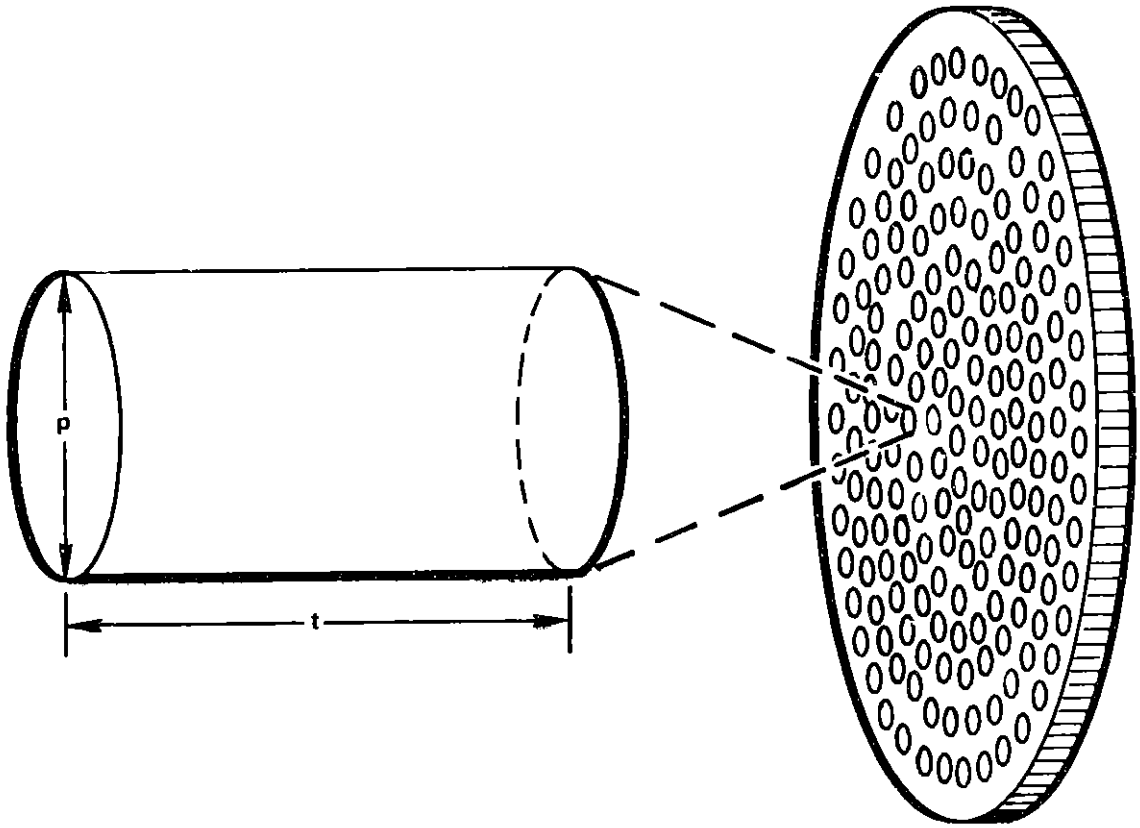

Figure 2-13. Model Used for Filter Analysis

Assuming an isotropic filter this porosity coefficient may be determined from the weight per unit area w of the screen material.

$$\xi = 1 - \frac{w}{t\rho_{mat'l}} \tag{2-32}$$

Here t is the screen thickness and $\rho_{mat'l}$ is the weight density of the filter material. Noting that the flow rate Q_{pipe} through the filter equals the velocity through the pipe times the pipe area and substituting into equation (2-29) gives

$$\Delta P = 4C_f \frac{\rho}{2} \frac{t}{p} \left(\frac{Q_{pipe}}{\xi A_{pipe}} \right)^2 \tag{2-33}$$

Definition of a friction factor f as four times the coefficient of friction C_f yields:

$$\Delta P = f \frac{\rho}{2} \frac{t}{p} \left(\frac{Q_{pipe}}{\xi A_{pipe}} \right)^2 \tag{2-34}$$

What needs to be determined is the friction factor f. For a series of filters by the same manufacturer a plot of log Re versus log f was made.[4] It is shown in Figure 2-14. The Reynold's number used in the plot was based on the filter particle retention size and velocity through a filter passage, i.e.,

$$Re = \frac{V_{hole} p}{\nu} \tag{2-35}$$

where ν is the kinematic viscosity of the fluid.

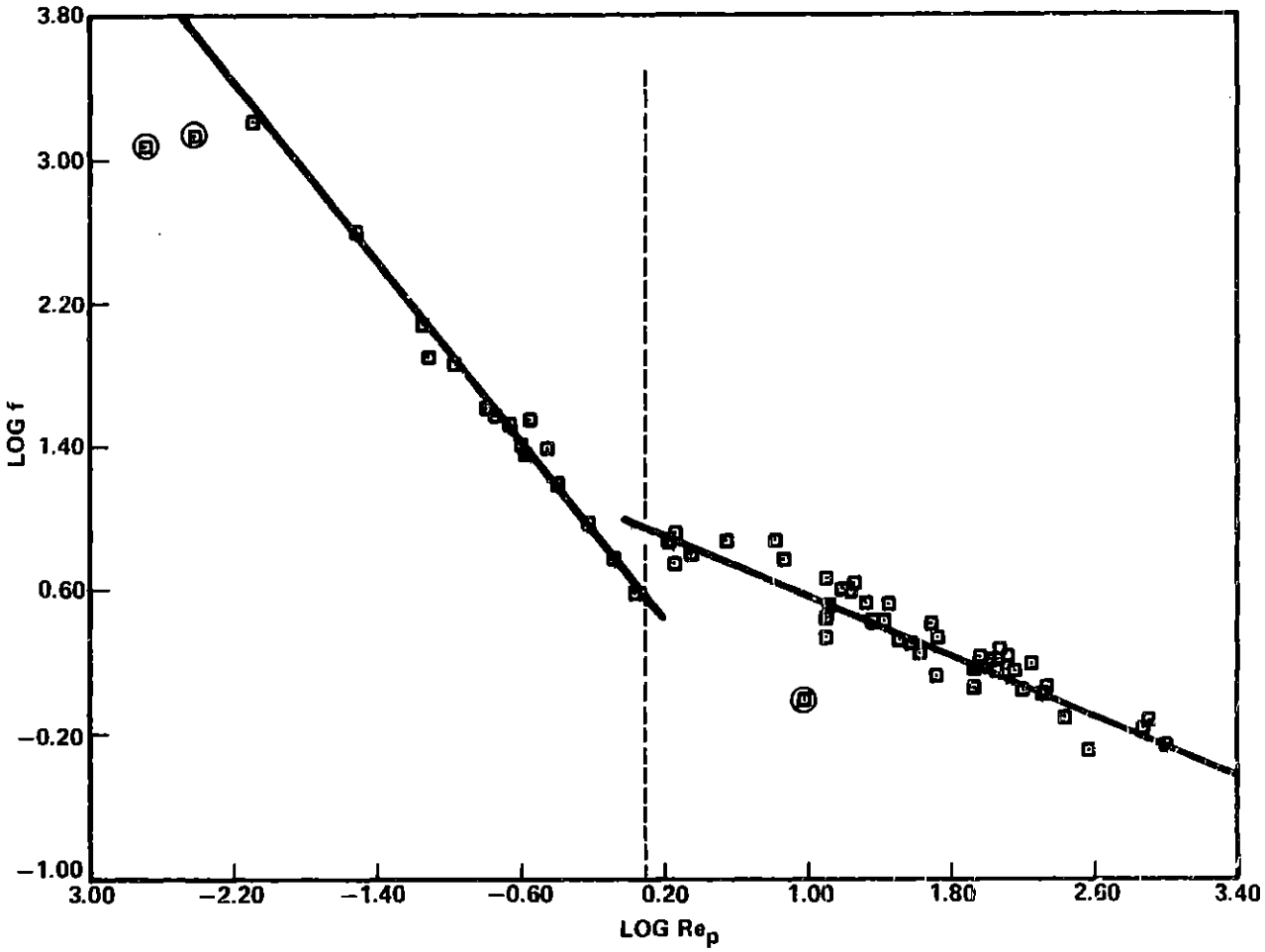

Figure 2-14. Least Squares Linear Fit of Filter Series Pressure-Flow Data

To apply the above results a least squares linear fit was done to the data of Figure 2-14. The three circled points were omitted in the fitting procedure which took place in the two regions log Re > .1 and log Re < .1. The somewhat arbitrary division point of log Re = .1 was decided by the clustering of the original data points. The choice, however, can also be justified by theory. For log Re = .1 the Reynold's number is 1.25. Reynold's numbers less than one indicate a very viscous Stoke's flow. Fluid behavior in this region is markedly different from that at higher Reynold's numbers.

For log Re < .1 the relationship between f and Re was $f = 5.1\ Re^{-1.2}$ which is nearly an inverse proportionality between the friction factor and the Reynold's number, i.e., $f \approx \frac{\text{const}}{Re}$. Substituting these approximate value into equation (2-34) gives

$$\Delta P = \frac{\text{const}\ \mu}{Vp\rho}\ \frac{\rho}{2}\ \frac{t}{p}\left(\frac{V}{\xi}\right)^2 = \text{const}\ \mu\ \frac{t}{p^2}\ \frac{V}{\xi^2} \qquad (2\text{-}36)$$

this pressure drop has a linear dependence on the fluid velocity and filter thickness and an inverse linear dependence on the hole area ($\approx p^2$). Fluid behavior is characteristic of a Stoke's flow where inertia terms are negligible (the mass density vanishes).

The upper region was fitted by the equation $f = 10.6\ Re^{-.42}$. The pressure drop dependency on velocity here goes as $\sim V^{1.6}$ and the density term remains. Here the flow is more inertia dependent.

2.4.1 Numeric Applications

The previous results will now be applied to the two types of filters found in the hydraulic system.

2.4.1.1 Pressure Drop Across a Pad Filter

The geometry of the pad filter is illustrated in Figure 2-15 and the pertinent parameter values are listed below.

$t = .011$ in.

$p = .0013$ in.

$\xi = .456$

$A = 1.04$ in.^{2}

$\nu = 1.24 \times 10^{-3}$ in.^{2}/sec

$\rho = 1.675 \times 10^{-4}$ lb-sec^2/in.^{4}

In the upper region the pressure drop across a pad filter is given by

$$\Delta P = .201\ Q^{1.58} \qquad (2\text{-}37)$$

where ΔP is given in psi and Q in gpm. The pressure flow characteristics of a pad filter are illustrated in Figure 2-16. The discontinuity in the curve at a flow rate of about .15 gpm is due to the uncertainty involved in the exact determination of the transition point between the two types of flows.

2.4.1.2 Pressure Drop Across a Valve Filter

The values for the pertinent parameters of the valve filter are listed below and its geometry is shown in Figure 2-17.

$t = .006$ in.

$p = .0004$ in.

$\xi = .361$

$A = .344$ in.^{2}

$\nu = 1.24 \times 10^{-3}$ in.^{2}/sec

$\rho = 1.675 \times 10^{-4}$ lb-sec^2/in.^{4}

The pressure drop across the valve filter in the upper region is given by

$$\Delta P = 4.86\ Q^{1.58} \qquad (2\text{-}38)$$

where again ΔP is in psi and Q in gpm. Figure 2-18 shows the pressure-flow characteristic. Note the discontinuity during transition to a different flow region.

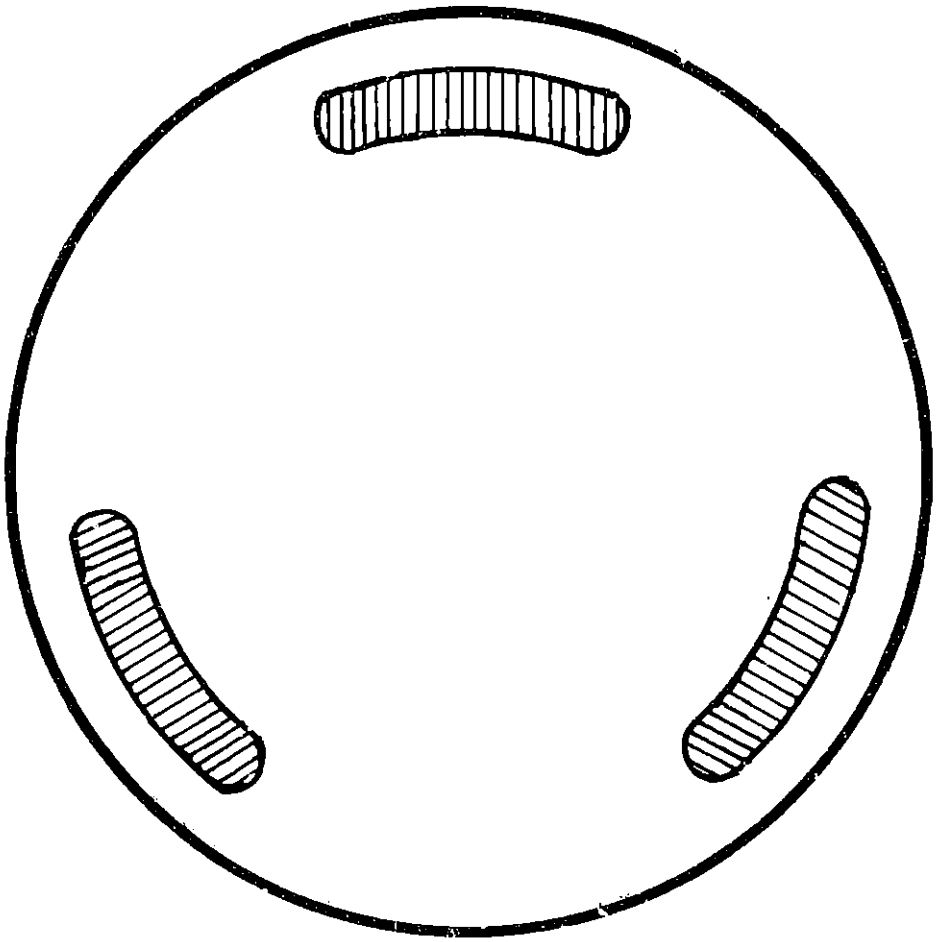

Figure 2-15. Geometry of Pad Filter

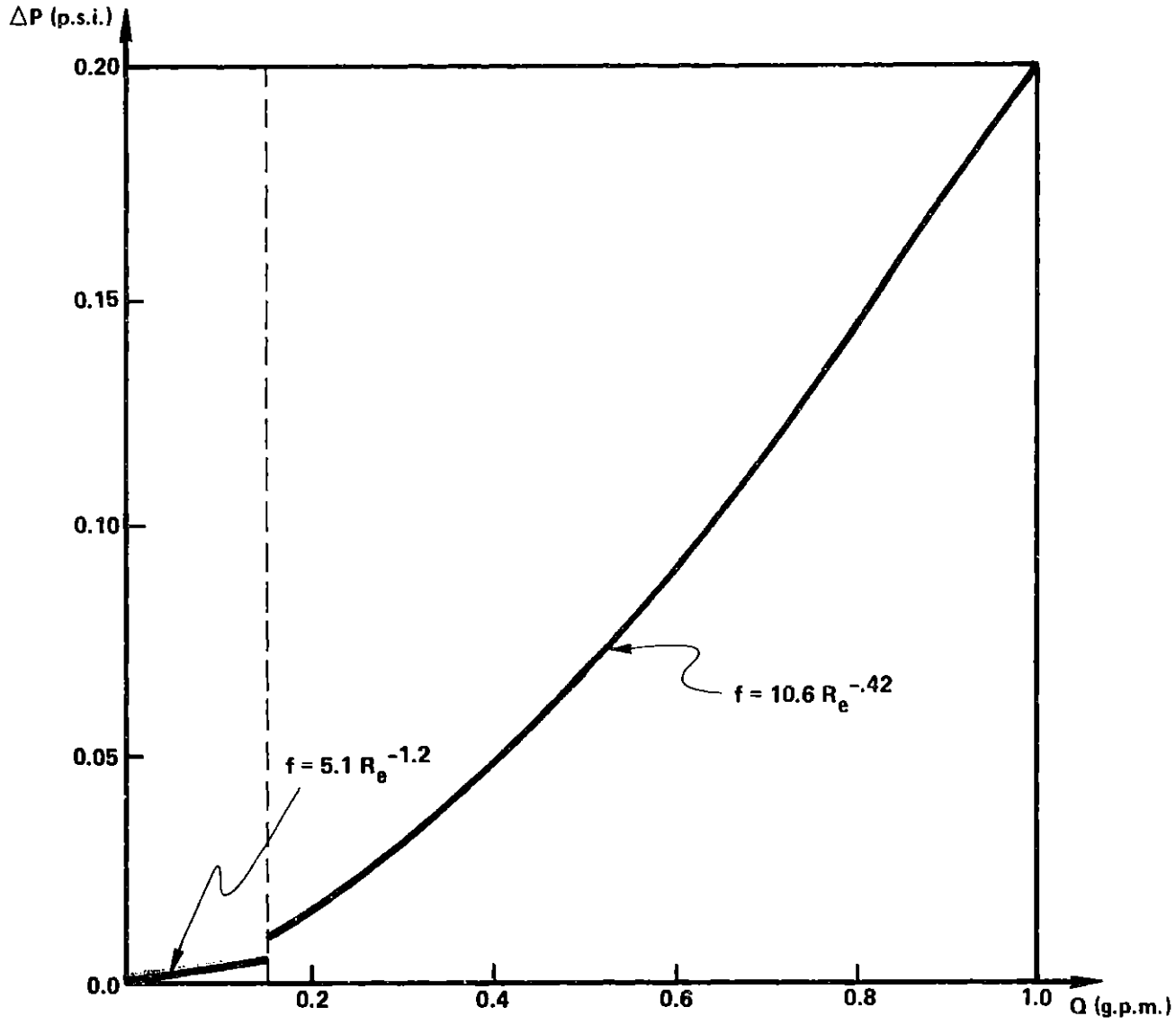

Figure 2-16. Pad Filter Pressure-Flow Characteristics

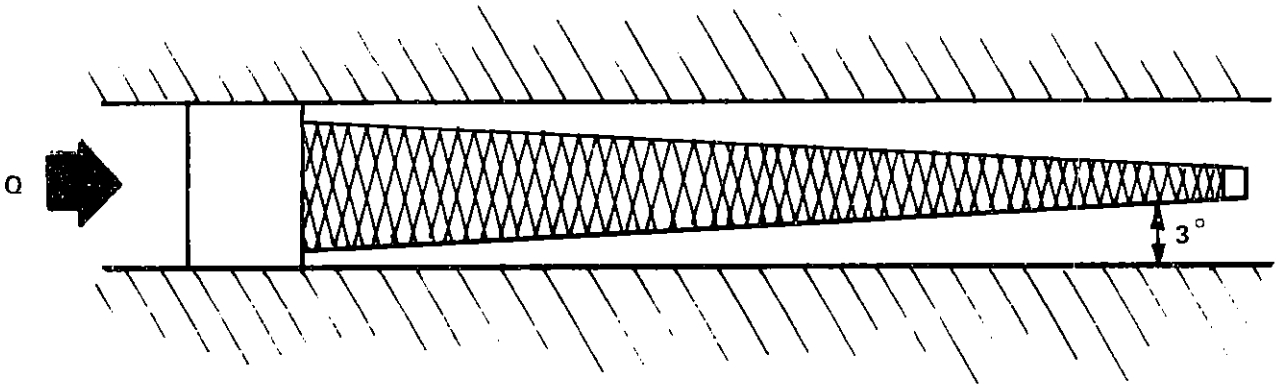

Figure 2-17. Geometry of Valve Filter

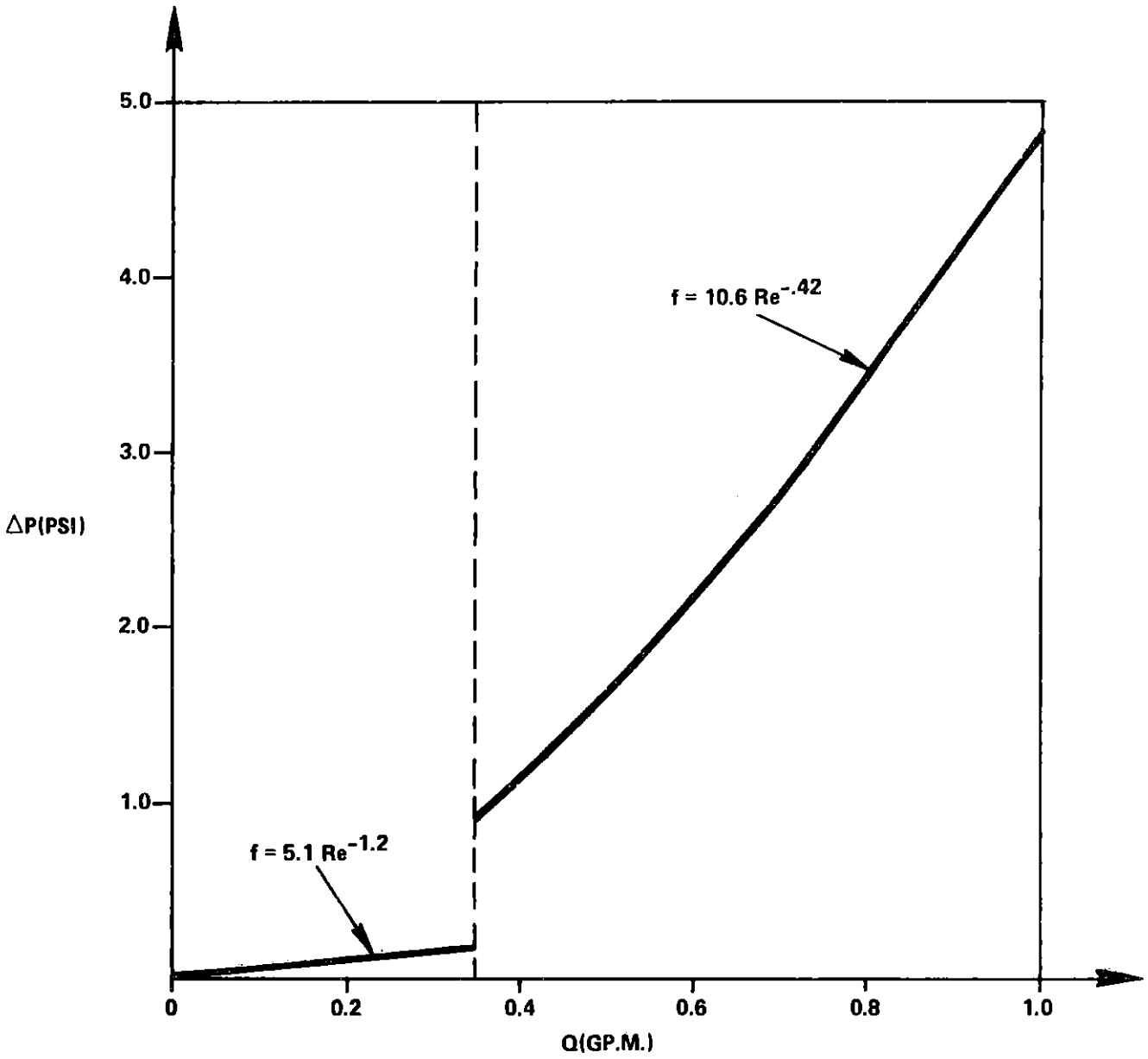

Figure 2-18. Valve Filter Pressure-Flow Characteristic

2.5 Sudden Contractions

Sudden reductions in flow cross sectional area produce an increased flow velocity and by Bernoulli's principles a corresponding pressure drop. One case in particular where this type of pressure drop is found is at the nozzles of the valves. Here a sudden area contraction is necessary to achieve the high flow rate which produces the reaction torque to control rotational ball motions. Two important features of the contraction determine the pressure drop; (1) the fractional area decrease and (2) the geometry itself of the contraction. First the effect of area reduction is examined.

Consider a flow Q along a passageway in which there is a cross-sectional area contraction from A_1 to A_2 $(A_1 > A_2)$. A corresponding pressure drop p_1-p_2 can be anticipated. Using Bernoulli's equation along a streamline gives

$$p_1 + \frac{\rho}{2}\left(\frac{Q}{A_1}\right)^2 = p_2 + \frac{\rho}{2}\left(\frac{Q}{A_2}\right)^2 \qquad (2\text{-}39)$$

Solving for the pressure drop along the contraction gives

$$\left(p_1 - p_2\right)_{\substack{\text{area}\\ \text{reduction}}} = \frac{\rho Q^2}{2}\left[\frac{1}{A_2^2} - \frac{1}{A_1^2}\right] \qquad (2\text{-}40)$$

Next the geometry of the contraction must be considered. A gradual contraction would incur only Bernoulli's pressure losses. A sudden contraction, however, acts as an orifice and accrues additional losses. The pressure drop across an orifice was given in section 2.2 and is repeated below for convenience.

$$\left(p_1 - p_2\right)_{\substack{\text{orifice}\\ \text{geometry}}} = \frac{\rho}{2}\left(\frac{1}{c_v^2} - 1\right)\frac{Q^2}{c_c^2 A_2^2} \qquad (2\text{-}41)$$

where again c_v and c_c can be found from fluids texts from geometry cosiderations.

The same flow which experiences the area reduction experiences the orifice geometry so the two resistances are in series and their pressure drops add. The total pressure drop due to the sudden contraction is given by

$$\left(p_1 - p_2\right)_{total} = \Delta P_{noz} \frac{\rho Q^2}{2}\left[\frac{1}{A_2^2} - \frac{1}{A_1^2} + \left(\frac{1}{c_v^2} - 1\right)\frac{1}{c_c^2 A_2^2}\right] \qquad (2\text{-}42)$$

2.5.1 Numeric Applications

Equation (2-42) will now be applied to the nozzle for this particular system. The geometry is shown in the upper portion of Figure 2-19 and the pertinent parameter values are given below.

$A_1 = 3.14 \times 10^{-2}$ in.

$A_2 = 2.57 \times 10^{-3}$ in.

$c_v = .98$

$c_c = 1.$

$\rho = 1.675 \times 10^{-4}$ lb-sec/in.

The resistance of the nozzle $R_{noz} = \frac{p_1 - p_2}{Q^2}$ is found to be $1.94 \times 10^2 \frac{psi}{gpm^2}$. A flow rate through the nozzle of .35 gpm (.7 gpm per valve) yields a pressure drop of 23.8 psi. A plot of the pressure drop across the nozzle ΔP versus the flow rate through the nozzle Q_{nozzle} is shown in Figure 2-19.

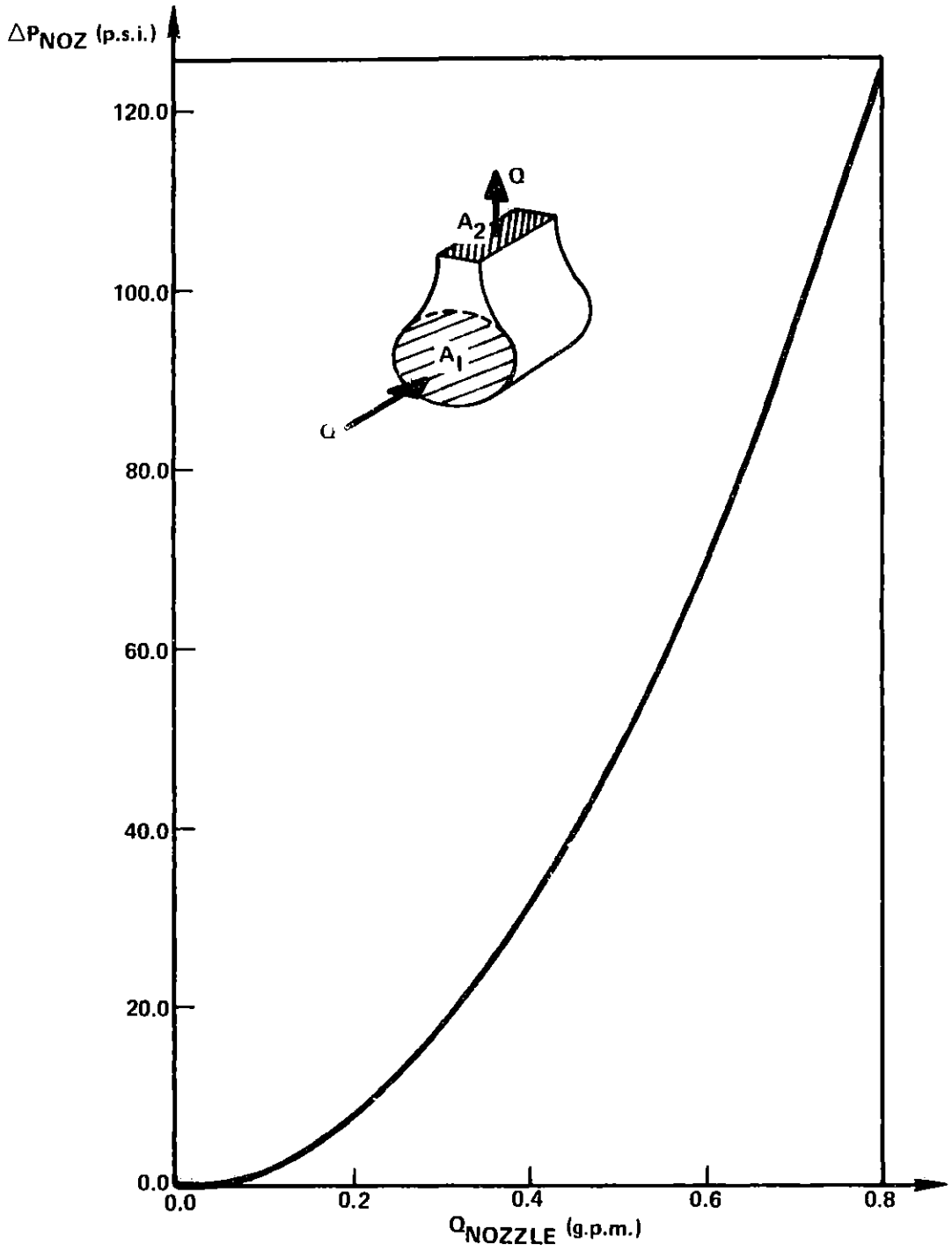

Figure 2-19. Jet Nozzle Pressure-Flow Characteristic

CHAPTER 3

TRANSLATIONAL MOTIONS AND SUSPENSION SYSTEM

3.1 Support Force of One Pad

As was seen from section 2.1, the pressure drop across the sill of a suspension pad varies with radius and gap. To find the support force provided by one pad we integrate the pressure across the pad and obtain the following expression:

$$F_{pad} = \pi R_p^2 P(R_p) + 2\pi \int_{R_p}^{R_s} P(r) r dr \qquad (3\text{-}1)$$

The equation for the pressure drop across the sill is

$$P(r) = \frac{6\mu \ln(R_s/r)}{\pi h_o^3 c_t} Q_{sill} \qquad (3\text{-}2)$$

For convenience a tilt coefficient c_t has been substituted for the bracketed quantity of equation (2-11) where

$$c_t \equiv 1 + \frac{3}{2}\left[\frac{\varepsilon}{2h_o}\left(1 + \frac{R_p}{R_s}\right)\right]^2 \qquad (3\text{-}3)$$

Substituting equation (3-2) into equation (3-1) and integrating, the expression for the pad force becomes

$$F_{pad} = \pi R_p^2 P(R_p) + \frac{3\mu}{h_o^3 c_t} R_p^2 Q_{sill}\left[\left(\frac{R_s}{R_p}\right)^2 + \ln\left(\frac{R_p}{R_s}\right)^2 - 1\right] \qquad (3\text{-}4)$$

Noting that the plenum pressure $P(R_p)$ and the flow across the pad sill Q_{sill} are both dependent on the pad gap and the rate of change of that gap we seek to eliminate these two quantities in favor of the gap and its time rate of change.

Continuity tells us that (assuming an incompressible fluid) the flow across the sill equals the flow through the pad orifice minus that flow which is stored within the pad gap and plenum as the clearance between the pad and outer shell changes with inner sphere translation. We have the following relationship.

$$Q_{sill} = Q_{orif} - Q_{stored} \tag{3-5}$$

The flow through the orifice is given by

$$Q^2_{orif} = \left[\frac{P_s - P(R_p)}{1/2\ \rho}\right]\left(c_d A_o\right)^2 \tag{3-6}$$

where, by comparison with equation (2-18),

$$c_d^2 \equiv \frac{c_c^2}{\left(\frac{1}{c_v^2} - 1\right)} \tag{3-7}$$

The flow stored can be expressed as

$$Q_{stored} = \pi R_s^2 \dot{h}_o \tag{3-8}$$

where $\dot{h}_o$ is the time rate of change of the gap.

Assuming that the pressure throughout the plenum is a constant, the plenum radius R_p can be substituted into equation (3-2) to get another equation for the plenum pressure

$$P(R_p) = \frac{6\mu}{\pi h_o^3 c_t} \ln \frac{R_s}{R_p} Q_{sill} \tag{3-9}$$

Substituting equation (3-8) into equation (3-5) gives an alternative expression for the flow across the pad sill.

$$Q_{sill} = Q_{orif} - \pi R_s^2 \dot{h}_o \tag{3-10}$$

We now have three equations, (3-6), (3-9), and (3-10) for the three unknowns Q_{orif}, $P(R_p)$ and Q_{sill}. Solving them simultaneously we get

$$P(R_p) = P_s - \frac{\rho Q_{orif}^2}{2(c_d A_o)^2} \tag{3-11}$$

where

$$Q_{orif} = \frac{-K + \sqrt{K^2 + \frac{2\rho}{(c_d A_o)^2}\left(P_s + K\pi R_s^2 \dot{h}_o\right)}}{\frac{\rho}{(c_d A_o)^2}}$$

and

$$K \equiv \frac{6\mu}{\pi c_t h_o^3} \ln \frac{R_s}{R_p}$$

To obtain the support force of one pad, the flow through the orifice and plenum pressure are calculated from equation (3-11) and substituted into equation (3-5) to determine Q_{sill}. These values are then back substituted into equation (3-4) giving the force.

A plot of the force versus pad displacement is given in Figure 3-1 for a pad tilt of 0.0 inches and gap rate of change of 0.0 in/sec. The effect of tilt is to decrease the support force of the pad. This effect is shown in Figure 3-2. The force is also lessened when the gap increases with time. The velocity effect is illustrated in Figure 3-3. This situation occurs when the ball is translating radially within the shell. Half of the suspension pads experience a gap increase with time and the remainder experience a gap decrease. The composite effect of all eight pads is investigated in the next section.

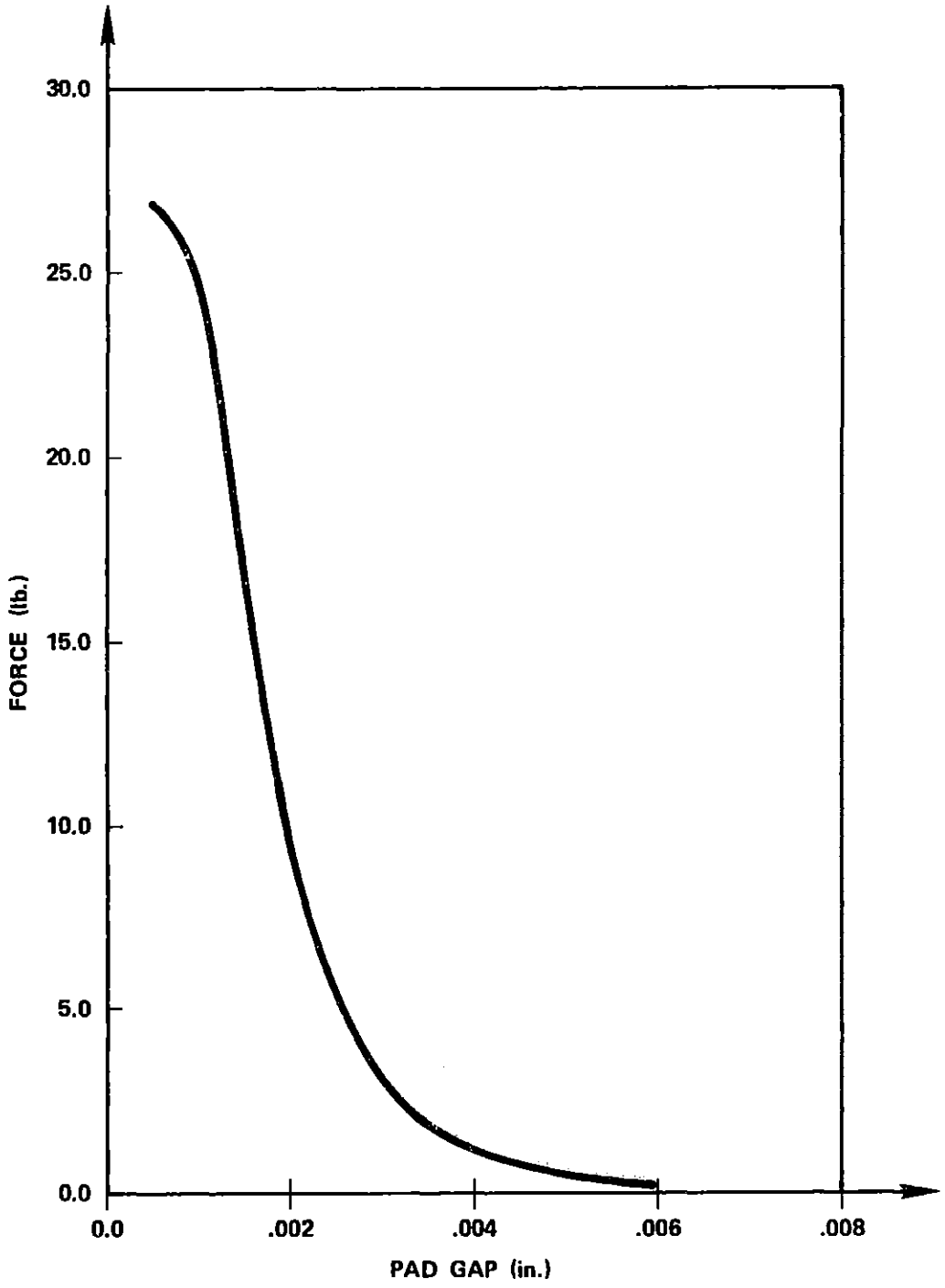

Figure 3-1. Support Force Versus Gap for One Pad

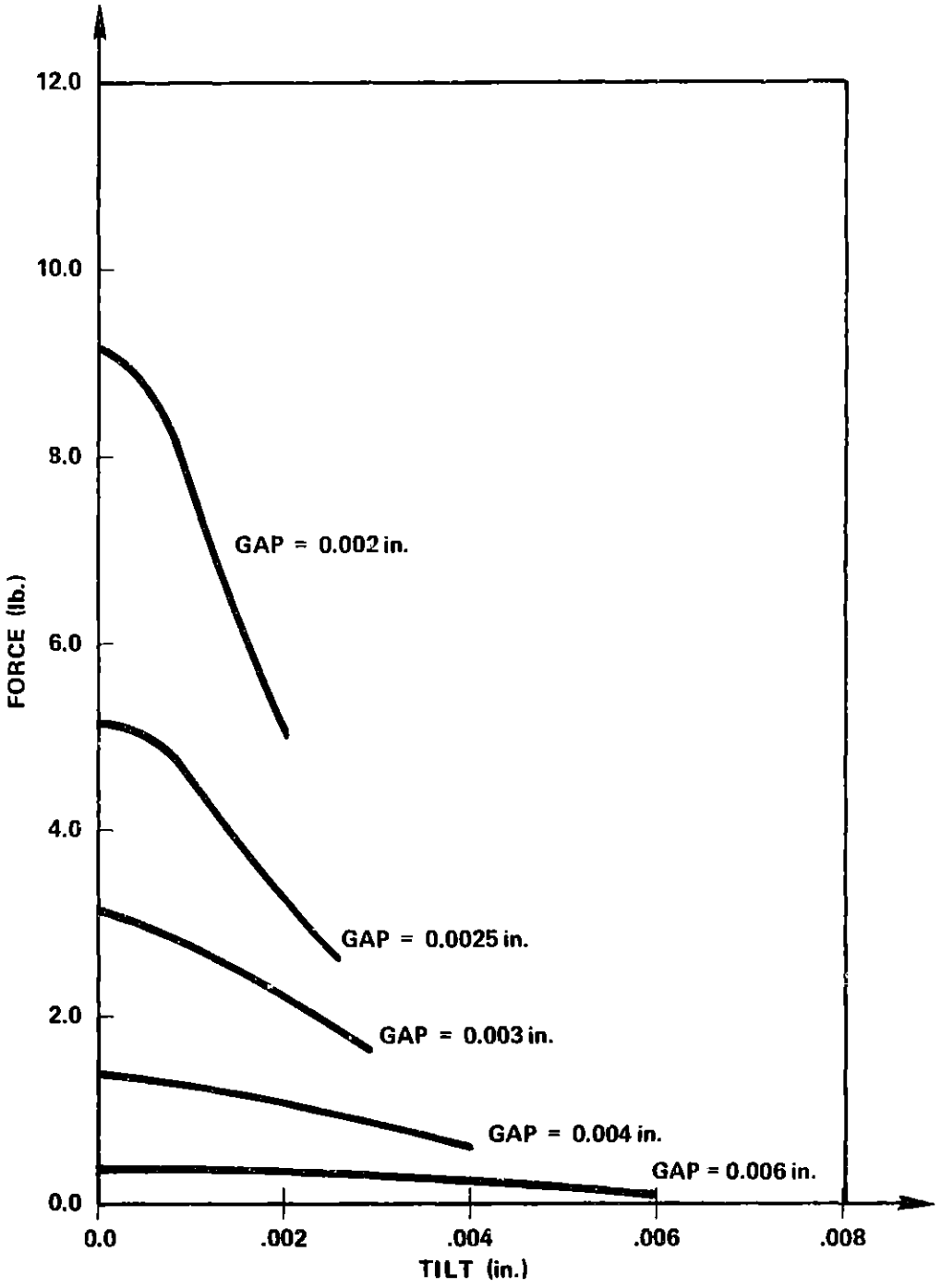

Figure 3-2. Pad Tilt Sensitivity

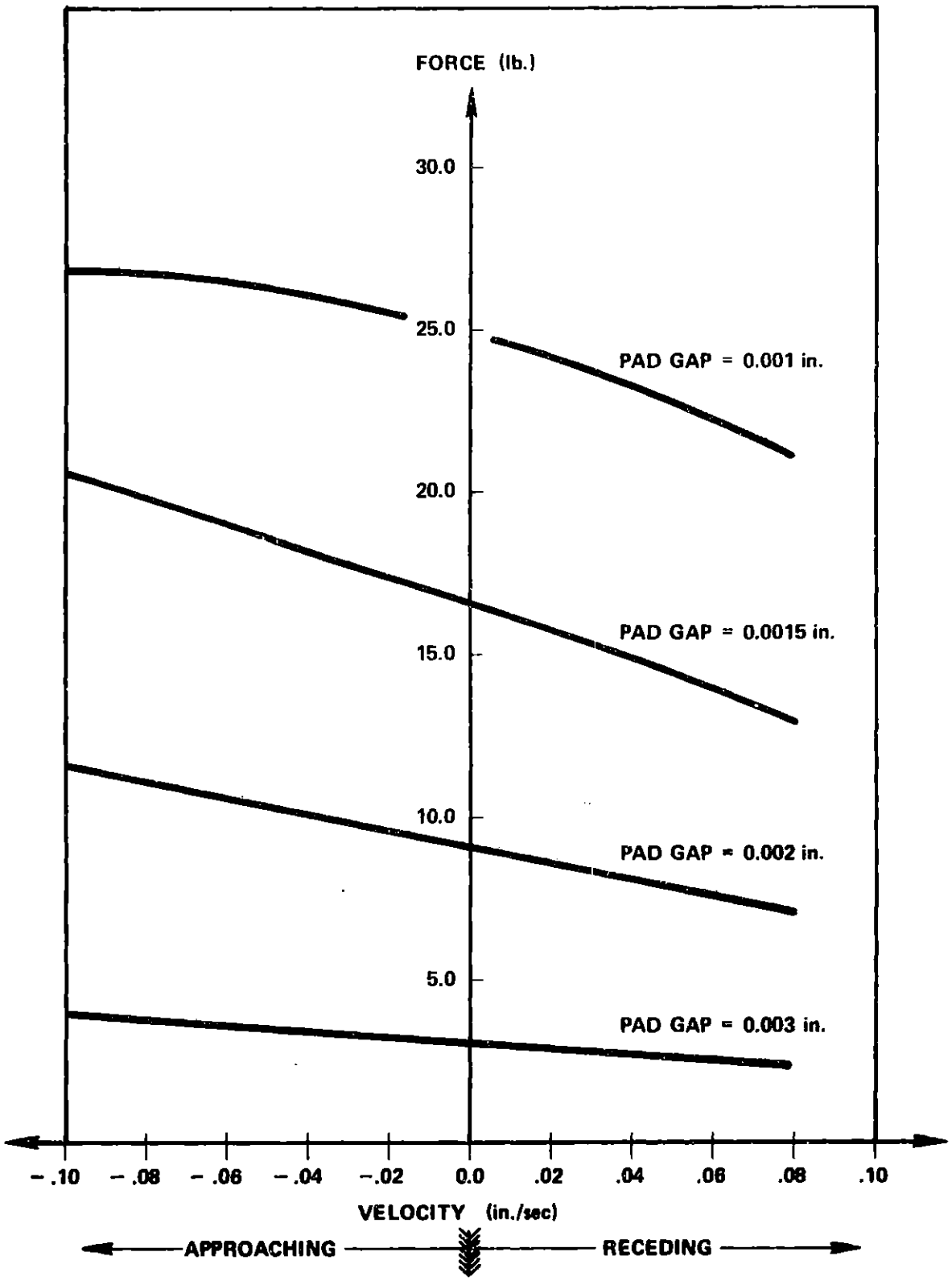

Figure 3-3. Pad Velocity Sensitivity

3.2 Force of Eight Suspension Pads

To understand the springlike performance of the eight suspension pads acting jointly we must grasp the geometry. Each pad is situated on the corner of a cube and exerts a force radially inward along a cube diagonal. Each force can be envisioned as a vector; its magnitude is determined by a pad gap, supply pressure, etc. as in the previous section and its direction is normal to the shell inner surface directly above the pad position, positive when pointing radially inward. The pad gap $\underline{h}$ and rate of change of gap $\dot{\underline{h}}$ can also be expressed as vectors parallel to the force vector $\underline{F}$, also positive when pointing radially inward. The vector direction for each pad can be defined by a unit vector $\hat{u}_n$ where n is the particular pad. In this way the three vectors concerned may be expressed as

$$\begin{aligned} F_n &= |\underline{F}_n|\hat{u}_n \\ h_n &= |\underline{h}_n|\hat{u}_n \\ \dot{h}_n &= |\dot{\underline{h}}_n|\hat{u}_n \end{aligned} \tag{3-12}$$

(See Figure 3-4).

To determine the composite effects of the force of all eight pads on the inner ball, the force, gap, and gap change vectors of each pad must be expressed in a common reference frame of the ball rather than the eight individual frames of the pads. For this purpose x-y-z- coordinates were used as the ball reference frame (see Figure 3-5). We pick the orthogonal axes z and x to serve as reference baselines from which to measure a latitude angle ϕ and a longitude angle θ for sphere displacement and velocity.

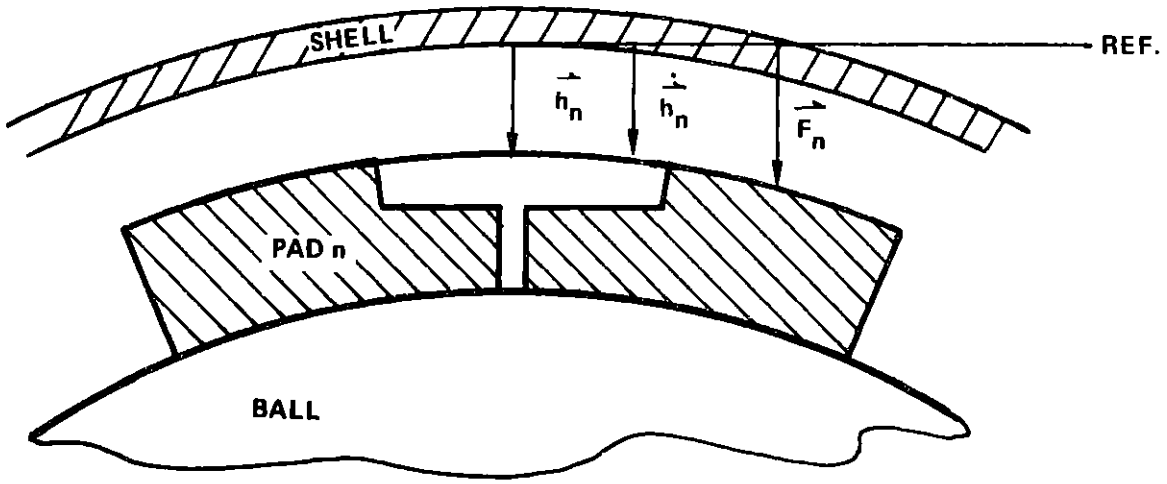

Figure 3-4. Displacement Velocity, and Force Vectors in Reference Frame of Pad

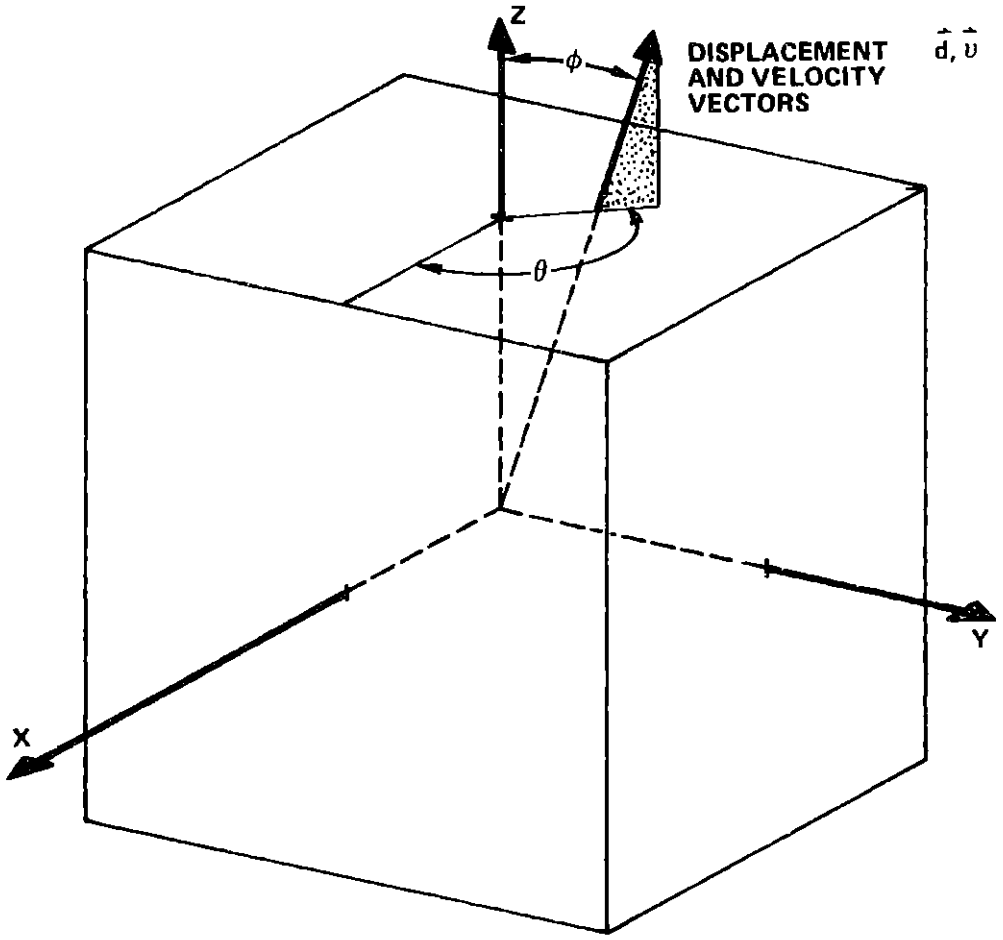

Figure 3-5. Coordinate Axes for Reference Frame of Ball

A ball displacement $\underline{d}$ in this frame is expressed in terms of its magnitude and direction as

$$\underline{d} = |\underline{d}|\{(\sin\phi\cos\theta)\ \hat{i} + (\sin\phi\sin\theta)\ \hat{j} + (\cos\phi)\ \hat{k}\} \tag{3-13}$$

where $\hat{i}$, $\hat{j}$, and $\hat{k}$ are the unit vectors in the x, y, and z directions respectively. Similarly, the ball velocity v is given by

$$\underline{v} = |\underline{v}|\ \{(\sin\phi\ \cos\theta)\ \hat{i} + (\sin\phi\ \sin\theta)\ \hat{j} + (\cos\phi)\ \hat{k}\} \tag{3-14}$$

The force contribution from a particular pad is desired in the direction of ball translation. The ball displacement $\underline{d}$ is converted into an equivalent pad gap at each pad with the following transformation

$$|\underline{h}_n| = \underline{d} \cdot \hat{u}_n + h_o \tag{3-15}$$

where h_o is the clearance of all pads when the ball is centered. Similarly the rate of change of pad gap can be related to the ball velocity:

$$|\dot{\underline{h}}_n| = \underline{v} \cdot \hat{u}_n \tag{3-16}$$

Knowing the pad gap and rate of change of that gap, the force for a pad can be calculated. The only component of this force desired though is that portion which is in the direction of translation of the ball. This value is found by taking the dot product of the pad force vector $\underline{F}_n$ and the ball displacement vector $\underline{d}$

$$F_n = \frac{\underline{F}_n \cdot \underline{d}}{|\underline{d}|} = |\underline{F}_n|\ \hat{u}_n \cdot \{(\sin\phi\cos\theta)\ \hat{i} + (\sin\phi\ \cos\theta)\ \hat{j} + (\cos\phi)\ \hat{k}\} \tag{3-17}$$

The total force comes from summing this quantity over all the pads

$$F_{TOT} = \sum_{n=1}^{8} F_n \tag{3-18}$$

Two configurations were investigated. They are shown in Figures 3-6 and 3-7. Figure 3-6 shows ball displacement and velocity along a cube diagonal. The corresponding latitude and longitude angles are $\phi = 54.74°$ and $\theta = 45°$. Figure 3-7 illustrates displacement parallel to a cube face. For this case $\phi = 0°$ and $\theta = 0$.

Figure 3-8 plots force versus displacement along a cube diagonal for various ball velocities. Figure 3-9 shows similar calculations for displacements and velocities along a cube face.

On a ball with eight suspension pads there are an infinite number of combinations of pad tilts. Each pad could be misaligned a different amount when it is placed on the ball so to define the effect of tilt on total suspension force is a foreboding task. To simplify matters, all pads were assumed to have the same tilt. Figure 3-10 plots the decay of the support force at increasing tilts for specified ball displacements along a cube face. The tilt effect is seen to be more pronounced at high ball eccentricities.

Figure 3-11 assumes zero tilt conditions on all pads. It illustrates the effect of ball velocity along a cube diagonal on the total suspension force of the pads.

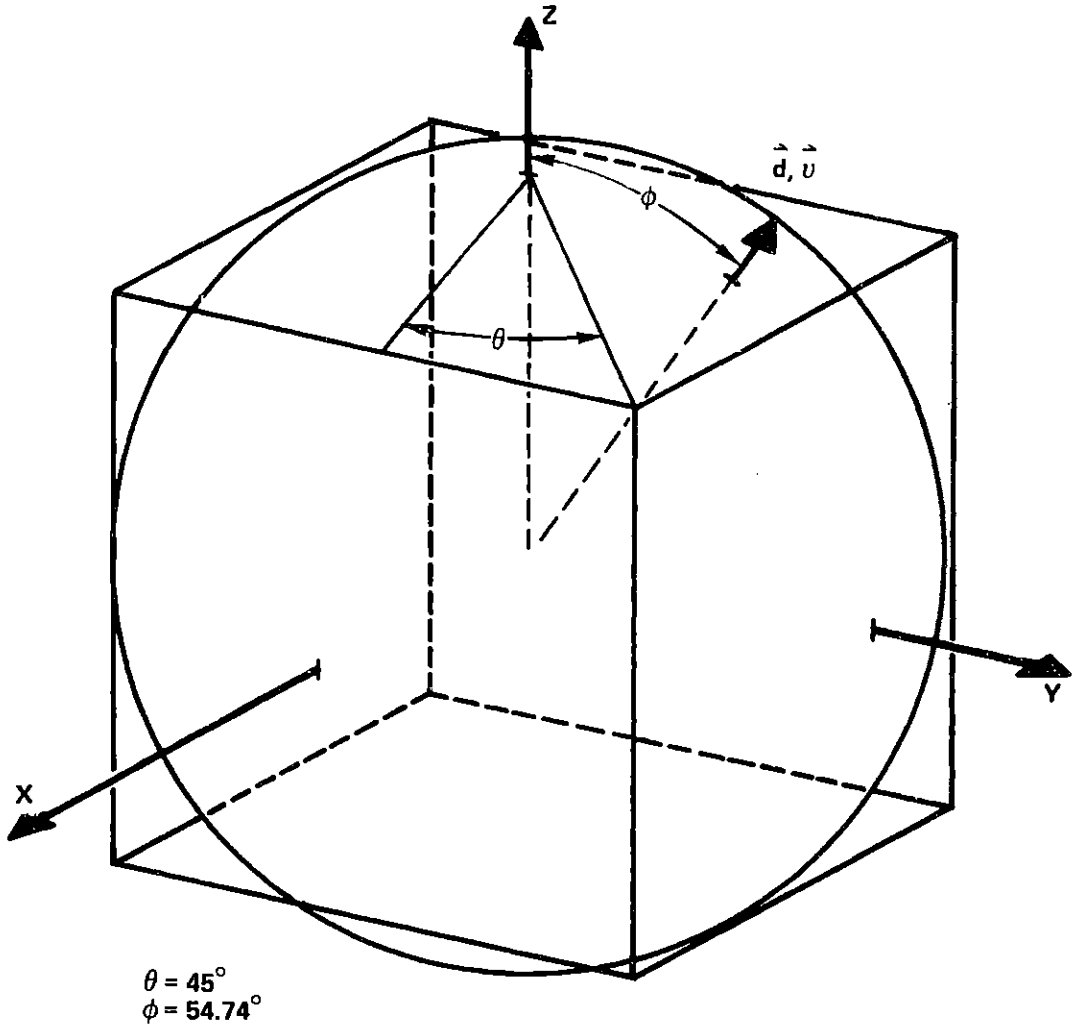

Figure 3-6. Ball Displacement and Velocity Along a Cube Diagonal

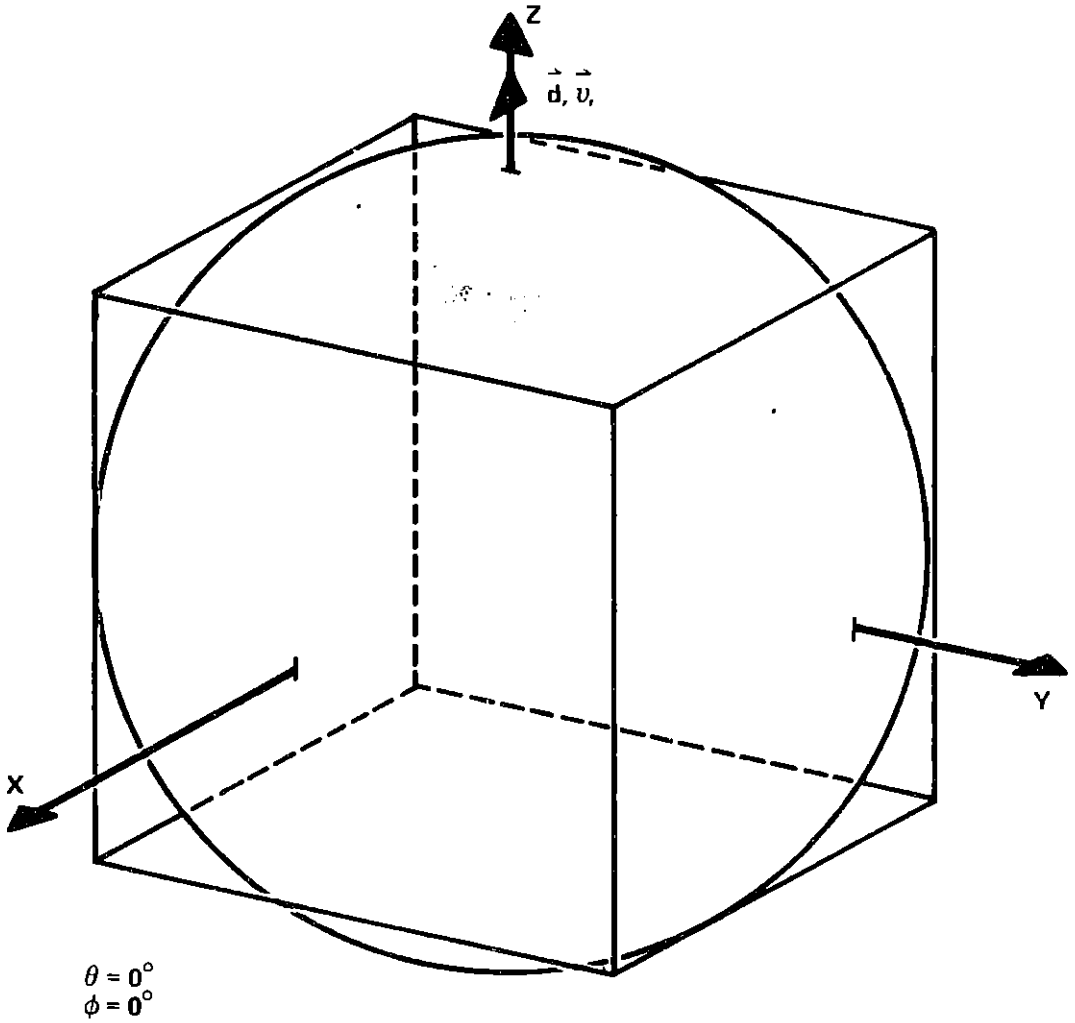

Figure 3-7. Ball Displacement and Velocity Along a Normal to a Cube Face

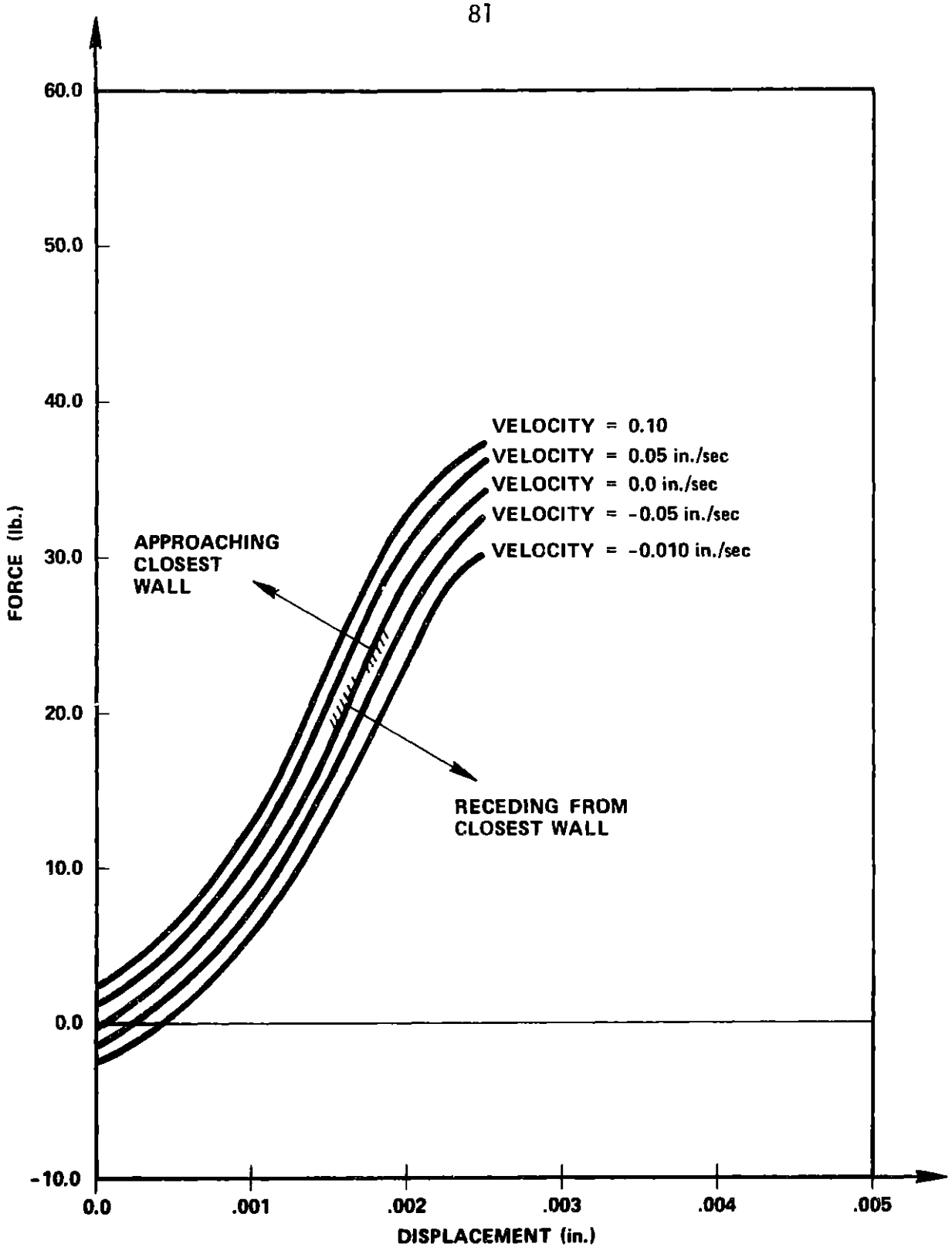

Figure 3-8. Support Force of Eight Pads Versus Ball Displacement Along a Cube Diagonal

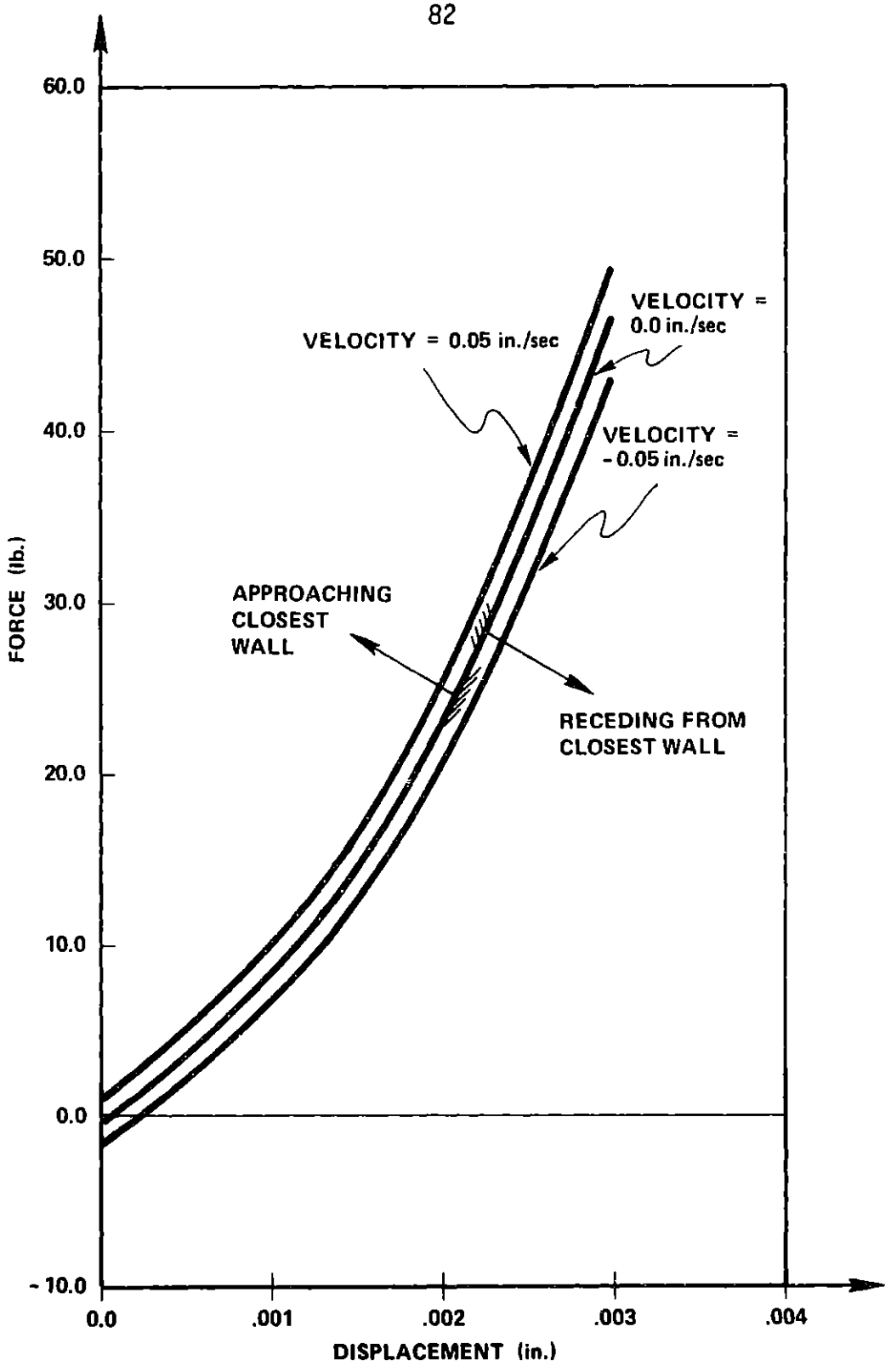

Figure 3-9. Support Force of Eight Pads Versus Ball Displacement Along a Normal to a Cube Face

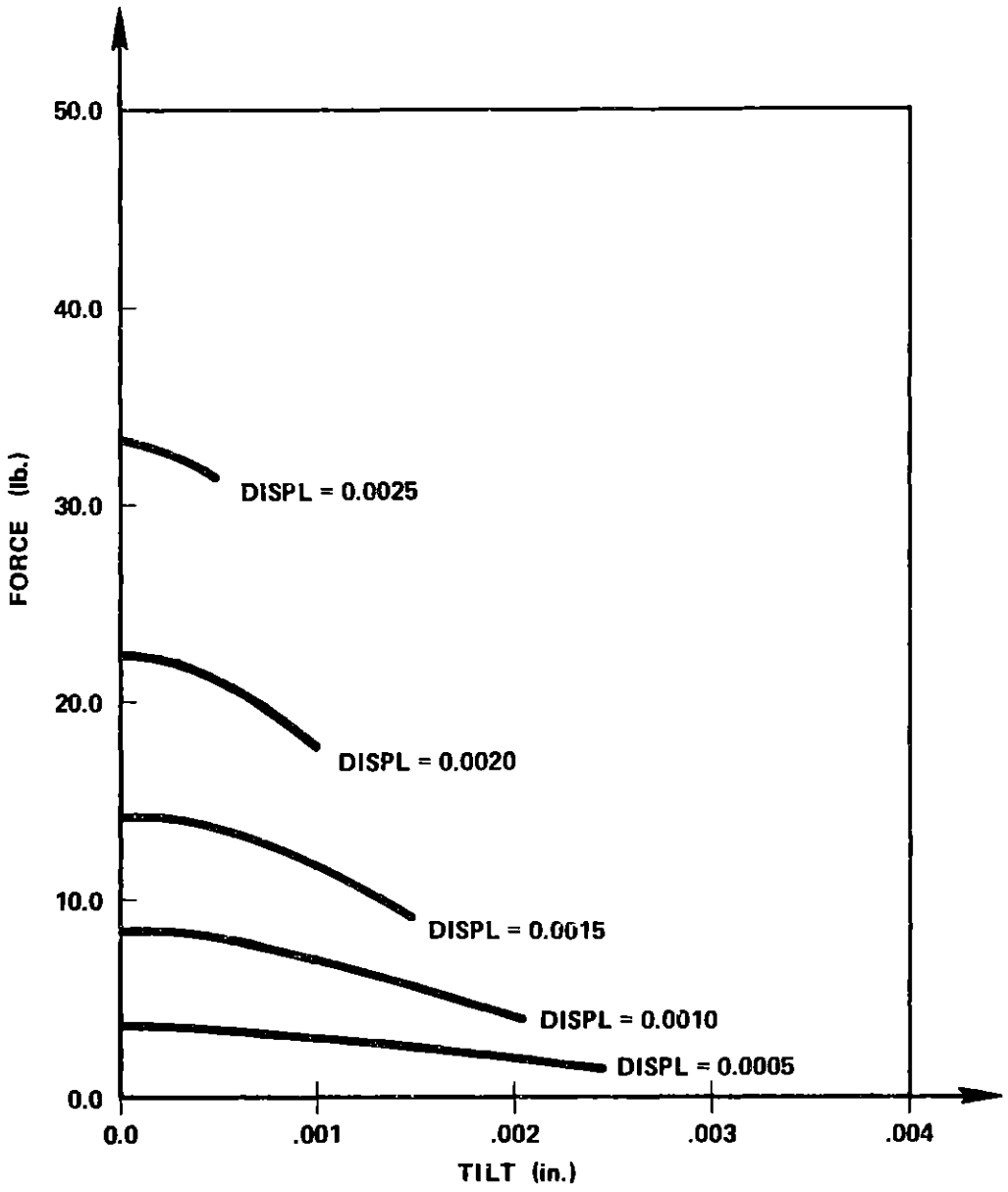

Figure 3-10. Tilt Effects on the Force of Eight Pads with Ball Displacement Along a Normal to a Cube Face

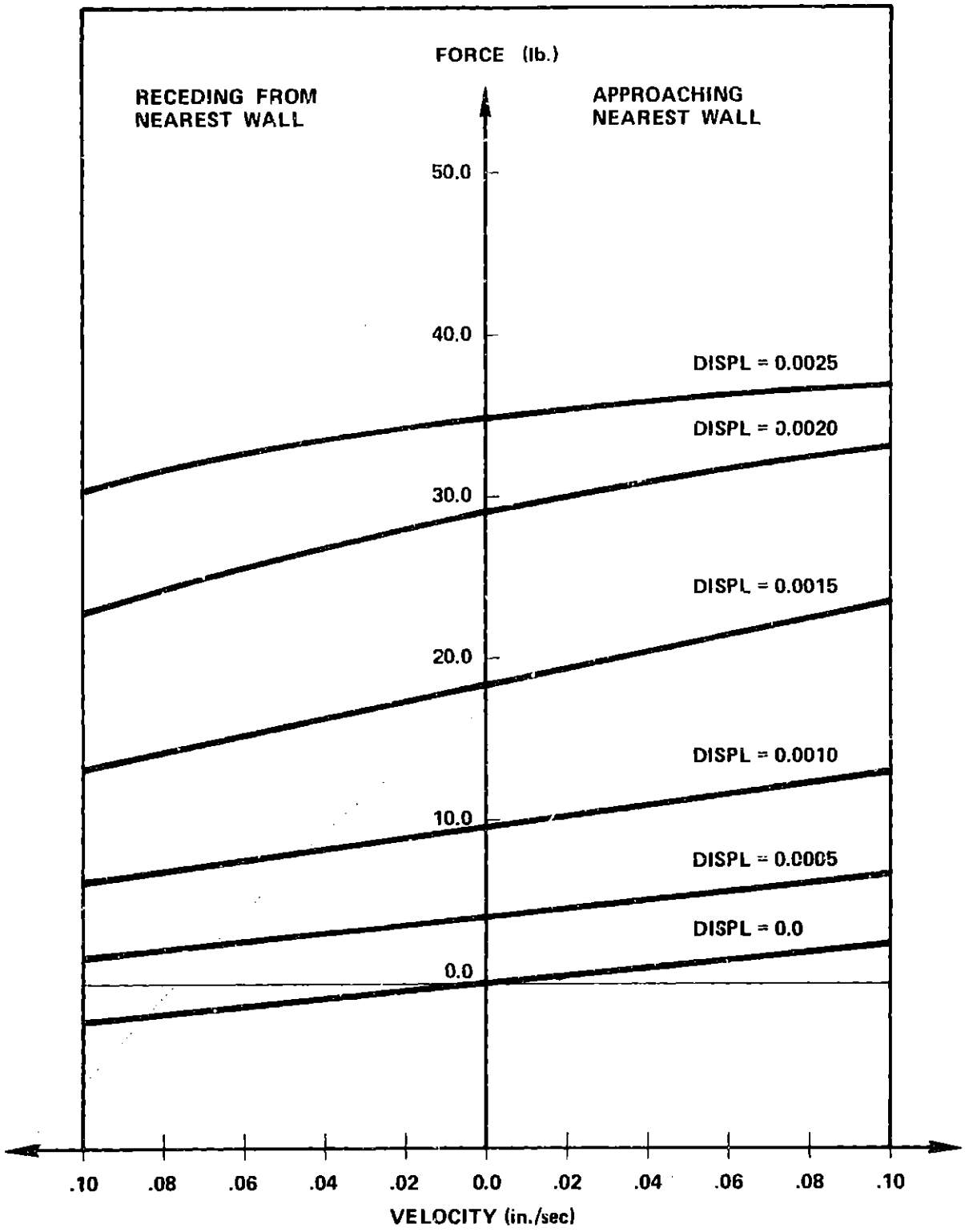

Figure 3-11. Velocity Effects on the Force of Eight Pads with Ball Displacement Along a Cube Diagonal

3.3 Differential Equation of Translational Motion

Knowing the spring force supplied by the eight suspension pads we would like to predict the translational subsystem's response to dynamic disturbances. The role played by the suspension pads in this analysis must be examined more closely. The previous section defined the force produced by the pads and showed it to be a function of the displacement of the ball from its centered position within the shell as well as the ball's rate of displacement. The effect of velocity and displacement can be represented as two separate elements in the model for the translational system. Displacement effects are attributed to a mechanical spring while velocity effects are attributed to a mechanical damper or dashpot. Any disturbances propagated to the inner ball must be reached via the outer shell so the model must include its mass as well. Figure 3-12 shows a schematic of the translational system.

The mass of the outer shell M_{out} is an easily determined quantity. The spring "constant" k and the damping "constant" b are in fact functions of the ball displacement from center x. They are determined in the previous section and it will be shown how they may be obtained from the graphs in that section. For the mass of the inner ball an effective mass M_{eff} must be used rather than merely the mass of the ball itself. The M_{eff} takes into account the inertia of the annular fluid which must be overcome as the fluid is squeezed around the ball when it moves eccentrically with respect to the outer shell.

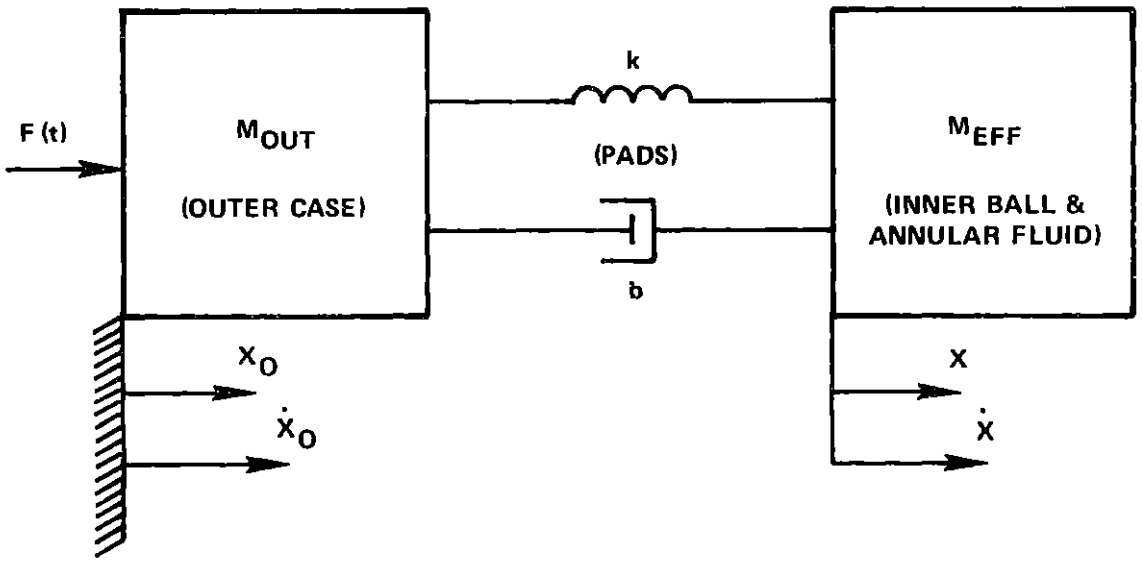

Figure 3-12. Lumped Element Model of Ball and Suspension Subsystem

From examining Figure 3-12 it can be seen that we have a third order system. There are three independent energy storage elements (the two masses and the spring) so one would expect one third order equation of motion or else more than one of lesser order. The relations for the system are:

$$M_{out}\,\ddot{x}_o + b(\dot{x}_o - \dot{x}) + k\,(x_o - x) = F\,(t)$$
$$M_{eff}\,\ddot{x} + b\,(\dot{x} - \dot{x}_o) + k\,(x - x_o) = 0 \qquad (3\text{-}19)$$

The second equation can be rewritten in the following form

$$M_{eff}\;\ddot{x} + b\dot{x} + kx = b\dot{x}_o + kx_o \equiv F_{input} \qquad (3\text{-}20)$$

Equation (3-20) is of the form of a second order system with a forcing function on the right hand side. The motions of the outer shell when subjected to F(t) can be interpreted as the forcing function. In reality the two masses do not act independently of each other but for the purposes of examining the dynamic responses of the inner ball some sort of forcing function $F_{input}\,(x_o, \dot{x}_o, t)$ may be assumed which is determined by the motions of the outer shell. Since the outer shell motions are random, to the inner ball the F_{input} function would also appear random although to a lesser degree.

Before interpreting equation (3-20) there must be some means of determining values for the M_{eff}, b, and k. The effective mass can be determined from considering the kinetic co-energy of the annular fluid as it moves out of the way of the translating inner ball.[5] Rather than including the inertia of the fluid as another parameter in the model

its effect is reflected in an increased mass of the inner ball. This effective mass increase is derived approximately in Appendix A and is given by

$$M_{eff} = \rho_s \frac{4}{3} \pi R^3 \left[1 + \frac{\rho}{\rho_s} \frac{1.2R}{h_o} \right] \tag{3-21}$$

where ρ_s is the density of the sphere, ρ the fluid density, R the ball radius, and h_o the annular gap. Assuming a neutrally buoyant sphere the fluid density and ball density are approximately equal. For $\rho = 1.675 \times 10^{-4}$ lb-sec^2/in.^{4}, R = 4.25 in., and h_o = .15 in. the effective mass becomes

$$M_{eff} = 1.88 \frac{\text{lb sec}^2}{\text{in.}} \tag{3-22}$$

which is 35 times the mass of the ball itself.

The spring coefficient k is a function of x. It is not a constant but may be considered so for a linearized system with small displacements. The slope of the force versus displacement curve for the sphere is the value for k. As an example, displacements along a cube diagonal will be considered. From Figure 3-8, k is found to be 4 lbs./.0005 in. or 8×10^3 lb./in. Note that this value could have been picked off any of the curves of Figure 3-8; they all have the same slope near zero displacement. The velocity effect of the force is taken into account by the damping coefficient b.

If one were to trace the path of the ball along Figure 3-8 as it oscillated within the outer shell one would proceed upward on one of the positive velocity curves. The ball would slow down as it approached the wall; i.e. the path would gradually change from the .10 velocity curve for example toward the zero velocity curve which it would finally reach at its peak excursion from center. As the ball recedes from the wall it would follow the negative velocity curves. The ball's oscillation would form a hysteresis loop on Figure 3-8.

The damping coefficient b is also a function of x. The slope yields the force versus velocity curve of Figure 3-11 yields its value. For oscillations about the center (displacement = 0) the slope of this curve is 2.3 lb/.10 in./sec or b = 23 lb-sec/in. At a .0005 displacement b = 25 lb-sec/in. so for very small displacements a b of 24 lb-sec/in. is reasonable.

It must be noted that these values have been taken with the ball centered. In an analysis investigating extreme conditions the ball can withstand without collision with the outer shell (and resultant loss of inertial reference) the k and b are conservative. Both the damping and spring coefficients increase at higher eccentricities. The system in effect becomes stiffer in that region.

Two parameters are important in understanding system performance. They are the damping ratio ξ and the natural frequency ω_n. The damping ratio is an indication of the speed of response of a system. The natural frequency states where the system resonance is likely to occur.

The damping ratio ξ is given by

$$\xi = \frac{b}{2\sqrt{k\ M_{eff}}} \tag{3-23}$$

For this system its value is about .1. The natural frequency is given by

$$\omega_n = \sqrt{\frac{k}{M_{eff}}} \tag{3-24}$$

For this system ω_n = 65.2/sec or 10.37 cps.

Figure 3-13 is a sample of the system's response for various values of k, b, and M_{eff}, when the forcing function is a sudden step in force as shown in the upper portion of the figure.[6] The present system would fail after about .05 seconds if the outer shell were disturbed in such a way that a step input of 14 lb of force was suddenly applied to the inner ball system. A step force of anything less and the ball would not collide with the outer shell. Any force greater and it would collide sooner. For example, a 20 lb step in force would result in a collision after only .03 seconds. Again it should be noted that these estimates are conservative. Since k increases at higher displacements, readings

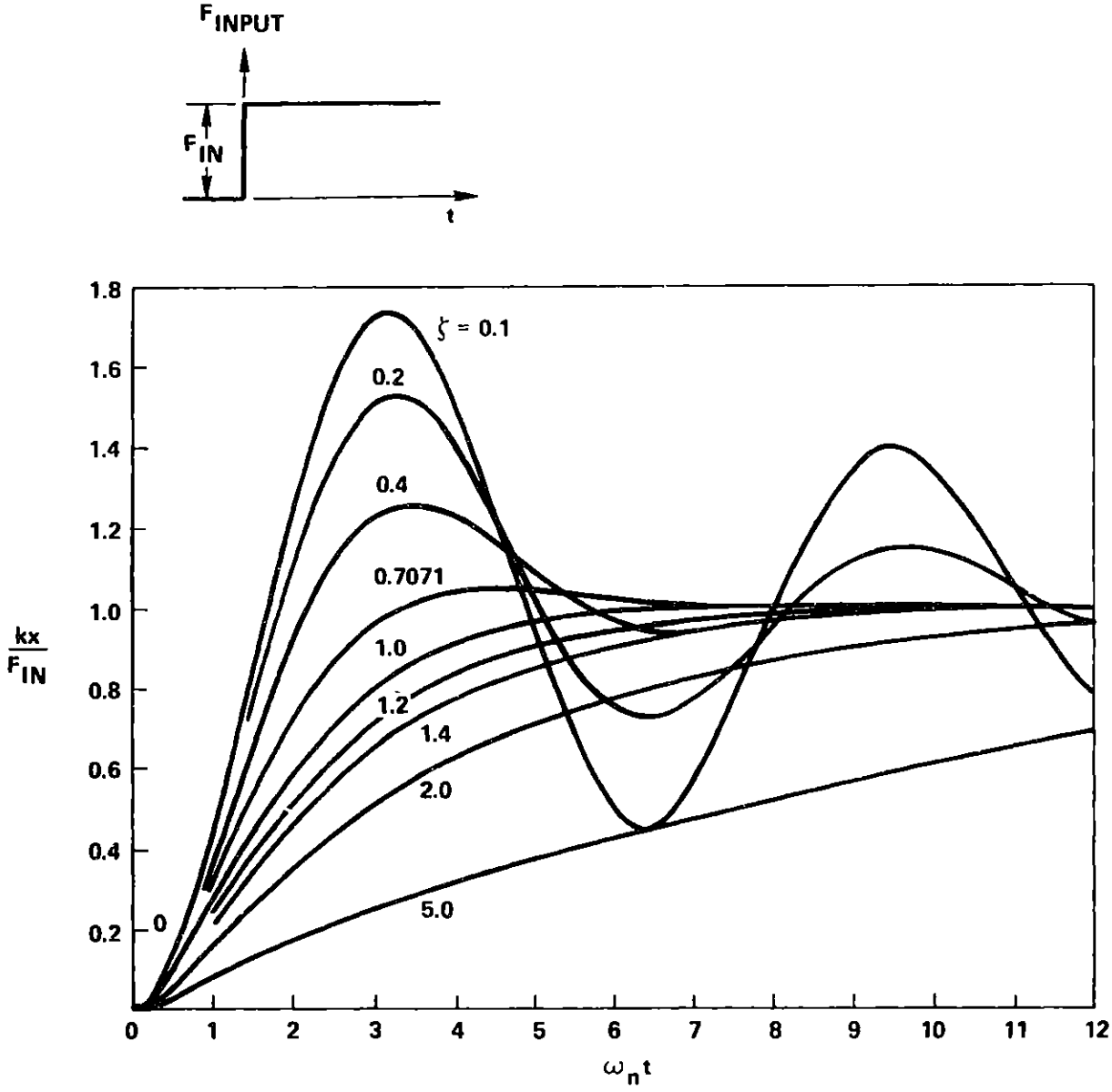

Figure 3-13. Complete Family of Transient Response Curves for a Second Order System Subjected to a Step Input

would be taken farther up along the ordinate scale of Figure 3-13. Higher values of b at greater displacements would entail reading off lower curves in the family.

Calculations done at a displacement of .002 in. would yield the following results:

$$k = 1.9 \times 10^4 \text{ lb/in.}$$

$$b = 125 \text{ lb sec/in.}$$

$$\omega_n = 100/\text{sec} = 16 \text{ cps}$$

$$\xi = .33$$

A step input force of 40.7 lb would cause collision after about .03 seconds. Any lesser force is admissible. A greater force would again cause collisions sooner.

One could also investigate what response could be expected if F_{input} were a sinusoidal function of the form

$$F_{input} = F_{in} \cos \omega t \tag{3-25}$$

where F_{in} is the amplitude of the force and ω the frequency. Care would need to be taken to avoid operating at resonance conditions. Again if this were a linear system resonance conditions would occur when the driving frequency at resonance ω_{res} is given by

$$\omega_{res} = \omega_n \sqrt{1 - 2\xi^2} \tag{3-26}$$

For this system evaluated at zero displacement conditions this frequency is 64.5/sec or 10.27 cps. At this driving frequency the peak ball excursion from center x_{max} (again assuming constant k and b) would be given by

$$x_{max} = \frac{F_{in} / k}{2\xi \sqrt{1-\xi^2}} \tag{3-27}$$

for $\xi < 1/\sqrt{2}$ and

$$x_{max} = F_{in}/k \tag{3-28}$$

for $\xi > 1/\sqrt{2}$.[7]

It is desired to get a rough idea of the order of magnitude of the force F_{in} the inner ball could withstand under resonance conditions. Equation (3-27) could be rewritten as

$$F_{in_{max}} = kh_o \, 2\xi \sqrt{1-\xi^2} \tag{3-29}$$

where the annular gap h_o has been substituted for the maximum allowable excursion of the inner ball relative to the outer shell. For this system the maximum allowable amplitude of a sinusoidal forcing function operating at the resonant frequency is 4.77 lb. when all pertinent parameters are evaluated at zero displacement. If ξ and k are evaluated at a .002 in. displacement the force amplitude can be as high as 35.5 lb.

The two values calculated above differ significantly. The system is sufficiently non-linear that the preceding analyses are useful only in determining order of magnitude estimates on system performance. To determine the true dynamic response of the translational system would require a computerized solution of the system's displacement-dependent damping and spring coefficients $b(x)$ and $k(x)$. The entire third order system which includes the outer shell, would need to be examined in its full non-linear glory.

CHAPTER 4

ROTATIONAL MOTIONS AND TORQUING SYSTEM

4.1 Brush Friction

Since the eight brushes are the means by which the inner ball maintains electrical contact with the outer shell they are a major source of retarding frictional torque. They are configured on the ball as the suspension pads are. The eight brushes can be pictured as being positioned on the corners of a cube encasing the inner ball and then projected onto the ball. Each pad-brush combination is equi-distant from its three closest neighboring pad-brush combinations.

The frictional torque attributed to one brush can be given by the tangential force produced on the outer shell surface by the brush, multiplied by the normal distance from the spin axis of the outer shell to the brush, i.e., the moment arm of the brush. The tangential force is represented by ηF_N where F_N is the normal contact force between the brush and the outer shell surface and η is an empirically determined coefficient of friction. The moment arm of each brush is dependent upon the location of the spin axis of the outer shell.

Figure 4-1 shows a possible configuration of the inner ball and spin axis. From this figure it can be seen that the moment arm of brush 1 for example is given by $R \sin\phi$ where ϕ is the polar angle of the brush from the spin axis used as reference. The frictional torque due to brush 1 is thus given by

$$T_{BRUSH} = \eta F_N R \sin \phi_1 \qquad (4\text{-}1)$$

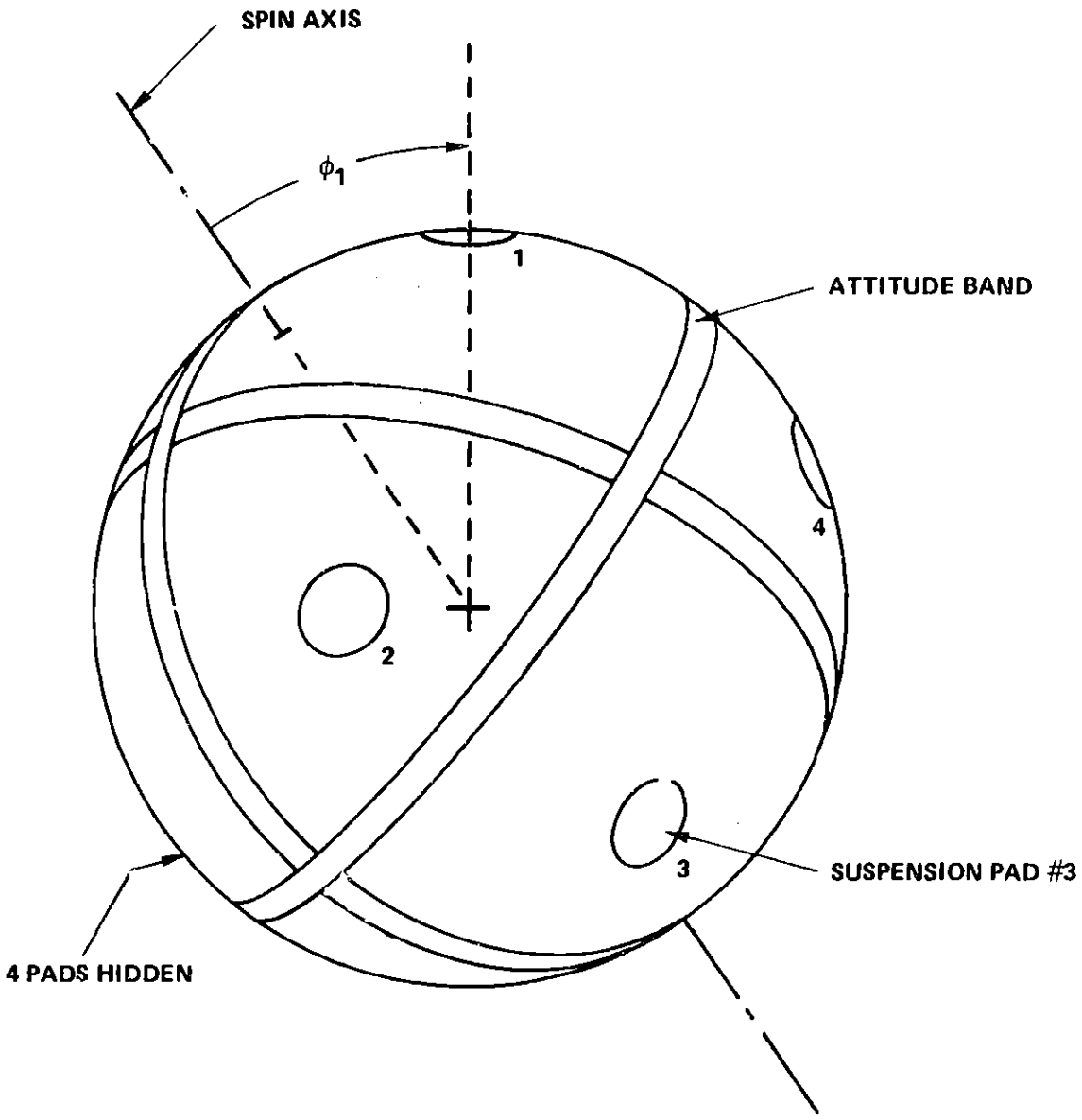

Figure 4-1. Possible Configuration for Ball Spin Axis

The total frictional torque due to brush contact is obtained by summing over all brushes assuming the normal contact force and the coefficient of friction η are the same for each brush.

$$T_{BRUSHES} = \eta F_N R \sum_{j=1}^{8} \sin\phi_j \tag{4-2}$$

Two extreme cases should be investigated: a) the spin axis penetrates the cube faces (Figure 4-2a) or b) the spin axis is located along a cube diagonal and penetrates two brushes (Figure 4-2b). For case (a) the polar angle for four brushes = (180° - 54.74°). Since the sin (54.74°) = sin (180° - 54.74°) the total frictional torque is given by

$$T_{BRUSHES_A} = 8\eta F_N R \sin (54.74°) = 6.53\eta F_N R \tag{4-3}$$

Case(b) with the spin axis on a cube diagonal works out similarly. The polar angle in this case is ϕ = 70.53° for three brushes, ϕ = (180° - 70.53°) for another three brushes, and 0° for two brushes. Total frictional brush torque is given by

$$T_{BRUSHES_B} = 6\eta F_N R \sin (70.53°) = 5.66\eta F_N R \tag{4-4}$$

For a normal force of .7 ounce, a ball radius of 4.25 inches, and η = .18 cases (a) and (b) work out to

$$\begin{aligned} T_{BRUSHES_A} &= 3.5 \text{ in. oz} \\ T_{BRUSHES_B} &= 3.03 \text{ in. oz} \end{aligned} \tag{4-5}$$

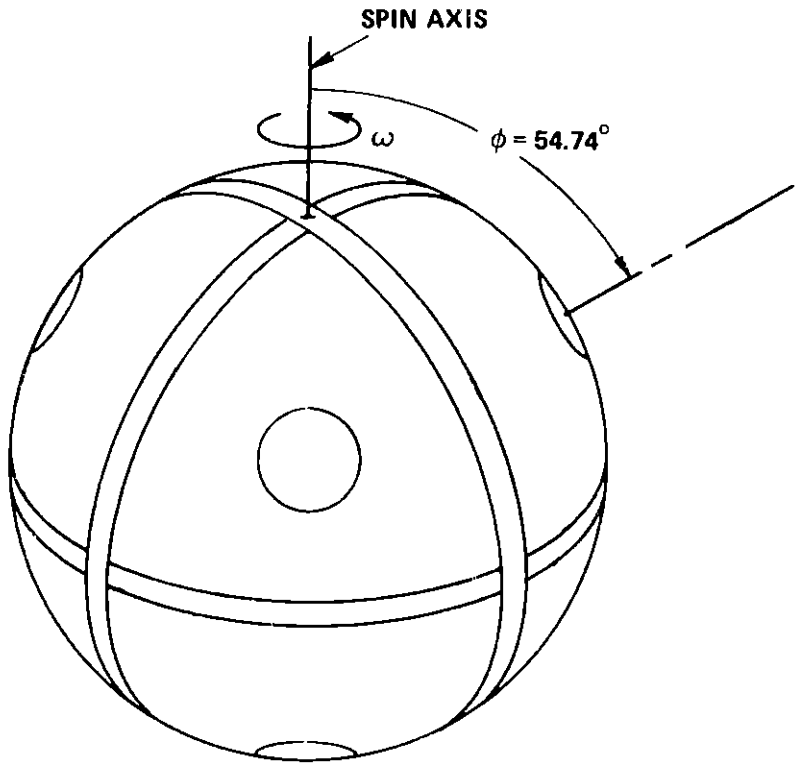

CASE A

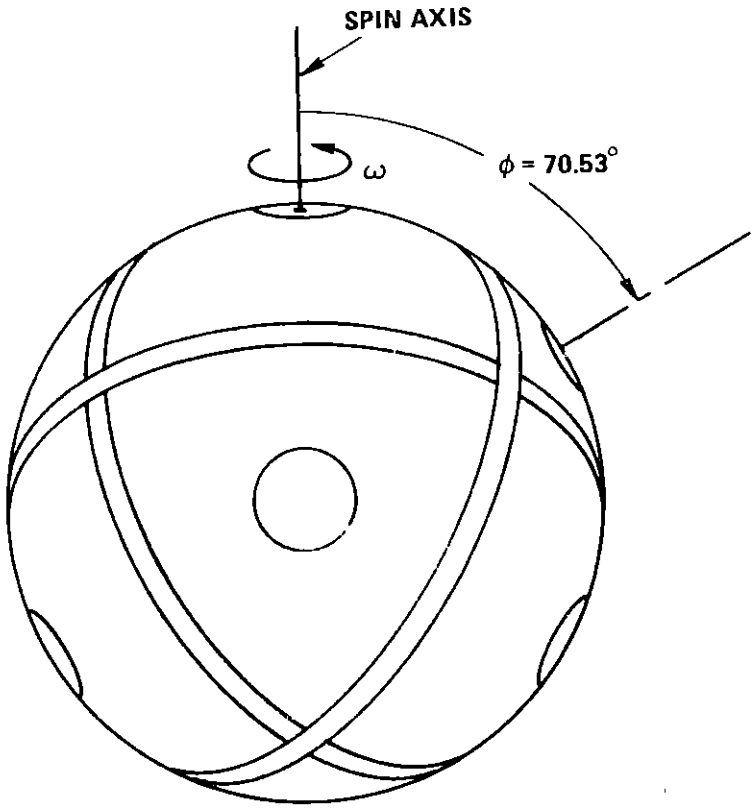

CASE B

Figure 4-2. Spin Axis Penetrating Cube Face and Along Cube Diagonal

This analysis for brush frictional torque is valid at any rotational speed of the outer shell. The static coefficient of friction's variation with sliding velocity is negligibly small. It may be assumed constant for both static and dynamic analyses.

4.2 Drag of Suspension Pads

Because the eight suspension pads protrude from the surface of the inner sphere they are subject to form and pressure drag as the outer shell pulls fluid past them. For the present configuration of eight pads and three torquer jet pairs, geometry tends to indicate the bulk of the jet streams from the torquer nozzles is directed along the attitude bands. The attitude bands divide the sphere surface into eight triangular sectors with one suspension pad centered within each. As the jet streams diffuse away from the attitude bands and toward the pad their velocities decrease. It seems a reasonable assumption, therefore, that the only velocity of major importance seen by the pads is that produced by the relative motion of the outer shell. The velocity of the fluid at the outer shell near a pad is given by the product of the outer shell's angular velocity relative to the inner ball ω and the moment arm of that pad $R \sin\phi$ where ϕ is the polar angle measured from the spin axis of the case to the pad. This is the same angle as described in section 4.1 on brushes and pictured in Figure 4-1. The velocity at the inner sphere is zero. Assuming a linear velocity distribution in the gap the average approach velocity as seen by a pad is given by

$$V_{REL} = \frac{R \sin\phi \, \omega}{2} \tag{4-6}$$

A suspension pad can be modeled as a cylinder positioned such that the projection of its long side is normal to the flow. The drag force D on such a cylinder is given by

$$D = \frac{\rho V_{REL}^2 \, A_{PROJ}}{2} C_D \tag{4-7}$$

where ρ is the fluid density, A_{PROJ} is the area of the cylinder projected normal to the flow (in this case the product of the pad height and diameter), and C_D is an empirically determined drag coefficient which is a function of the Reynold's number of the flow based on the cylinder diameter.

For a cylinder in a flow where the Reynold's number lies between 10^2 and 2×10^5 the coefficient of drag is approximately constant, i.e., $C_D \approx 1.2$ (see Figure 4-3).[8] Substituting this value and equation (4-6) into equation (4-7) gives

$$D = .15\rho A_{PROJ} R^2\omega^2 \sin^2\phi \tag{4-8}$$

To obtain the frictional drag torque for one pad, equation (4-8) must be multiplied by the moment arm $R \sin\phi$ to give

$$T_{PAD} = .15\rho A_{PROJ} R^3\omega^2 \sin^3\phi \tag{4-9}$$

The total frictional drag torque is obtained by summing equation (4-9) over all the pads.

$$T_{PADS} = .15\rho A_{PROJ} R^3\omega^2 \sum_{j=1}^{8} \sin^3\phi_j \tag{4-10}$$

As in section 4.1, two extreme cases are investigated. When the spin axis penetrates the center of a cube face (case a) four pads are at a polar angle of 54.74° and four at an angle of (180° - 54.74°). The drag torque produced by the pads becomes

$$T_{PADS\ A} = .653\rho A_{PROJ} R^3\omega^2 \tag{4-11}$$

For case b, the spin axis penetrates a cube diagonal and two pads are at a polar angle of 0°, three at angle of 70.53°, and three at an angle of (180° - 70.53°). For this case the drag torque becomes

$$T_{PADS\ B} = .754\rho A_{PROJ} R^3 \omega^2 \tag{4-12}$$

The assumption of a constant drag coefficient C_D of 1.2 was only valid for the region of Reynold's number between 10^2 and 2×10^5. One would like to know the relative rotation rate to which this Reynold's number range corresponds. If the Reynold's number Re is defined as

$$Re = \frac{V_{REL} d}{\nu} \cong \frac{R\omega d}{2\nu} \tag{4-13}$$

where d is the pad diameter and ν is the fluid dynamic viscosity, values for R, d, and ν may be substituted and a corresponding limiting value for ω found. For d = 1.4 inches, $\nu = 1.24 \times 10^{-3}$ in^2/sec, and R = 4.25 inches the limits $10^2 < Re < 2 \times 10^5$ correspond to .044/sec < ω < 83.57/sec or .007 cps < ω < 13.3 cps. The analysis is valid over the range of speeds of interest. A plot of case a) is given in Figure 4-4.

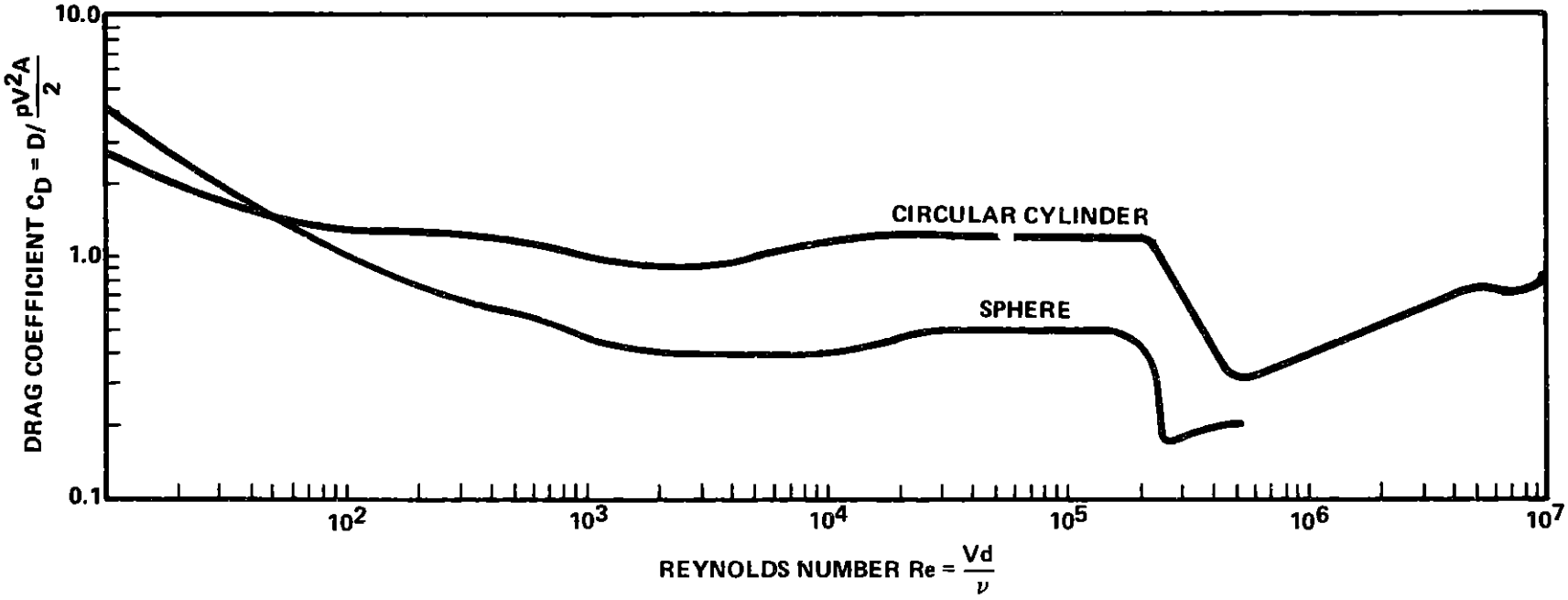

Figure 4-3. Drag Coefficient of Sphere and Cylinder as Function of Reynold's Number

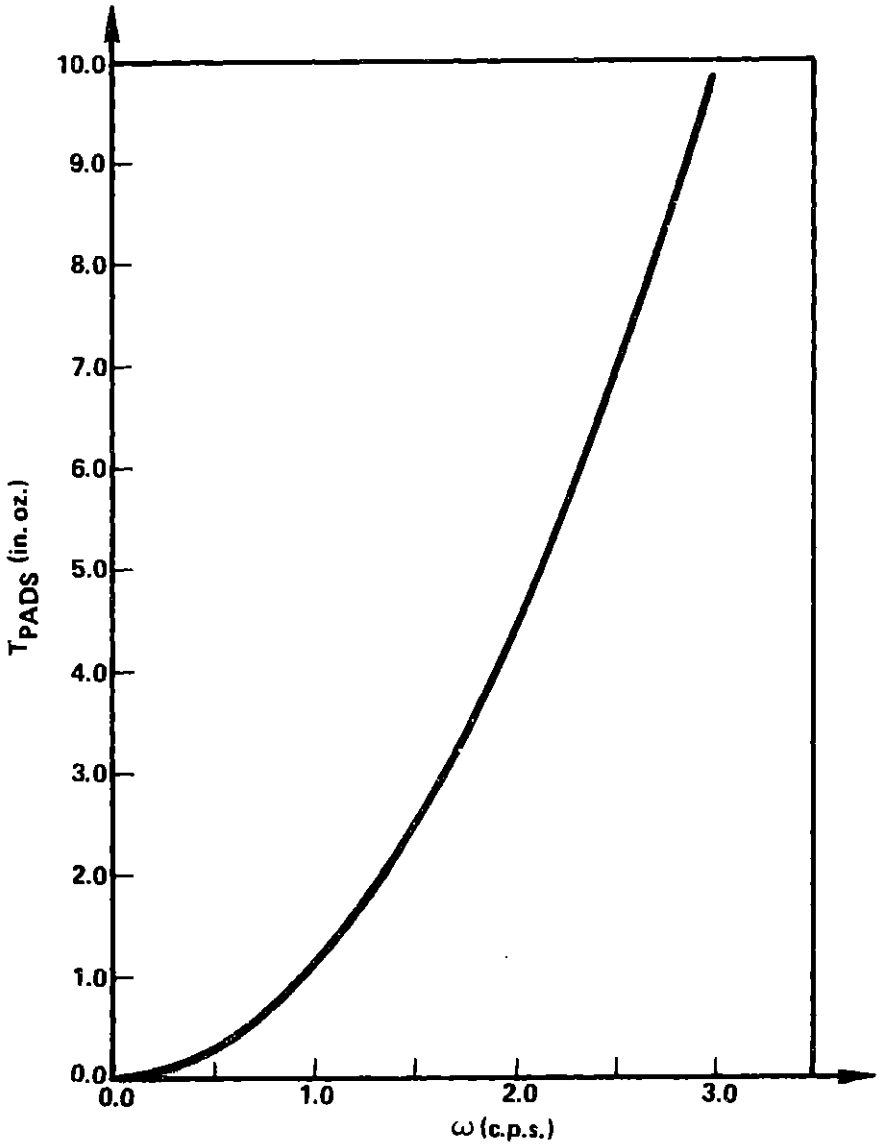

Figure 4-4. Profile Drag of Suspension Pads Versus Outer Shell Relative Rotation Rate

4.3 Parasitic Valve Drag

To prevent rotation of the inner ball a pair of torquer jets are located on each of three mutually perpendicular spin axes of the ball. These jets expel a high velocity fluid on the principle that the reaction forces produced by these jet pairs will counteract drag forces transmitted from the shell to the inner sphere via the annular fluid. These high velocity jet streams, however, excite the annular fluid and impart to it a higher momentum such that the annular fluid produces a parasitic drag torque on the inner sphere in a direction opposing the reaction torque of the jets. Calculation of this parasitic valve drag torque through integration of shear stress exerted on the inner sphere proved unsuccessful; rather, it was decided to investigate momentum changes of high velocity jet streams within the annulus and attribute these losses to the viscous dissipation on the inner ball and outer shell. To use this method a simplified model of the occurrences within the gap had to be made.

From observations of jet streams operating within a confined gap it was noticed that the jet would spread quickly to a finite width (about 2 inches on a 10-inch diameter ball) and remain at the width as it traveled circumferentially about the ball. This high velocity jet stream is primarily responsible for the induced drag on the inner ball. A stream velocity profile a few nozzle diameters downstream of the jet nozzle and another farther downstream where the jet's momentum has been dissipated are assumed and used to calculate momentum changes. With a model for jet geometry and velocity profiles within the jet stream, stall thrusts in the present system can be predicted at various measured flow rates through the nozzles.

4.3.1 Jet Geometry[9]

For the purposes of momentum calculations we need to know the cross-sectional area of the jet stream A_s and a characteristic stream velocity V_s. We can determine V_s by considering the control volume shown in Figure 4-5. As high velocity fluid emerges from the nozzle it entrains surrounding fluid to form a stream or trough of fluid with velocity higher than that of the surrounding fluid within the gap. Assuming dissipative forces are negligible in this spreading region the following momentum balance is employed.

$$\Sigma F = \oiint_{C.S.} \rho u^2 dA = \rho[V_s^2 A_s - V_j^2 A_j] \approx 0 \tag{4-14}$$

The stream velocity therefore is given by

$$V_s = \sqrt{\frac{A_j}{A_s}}\, V_j \tag{4-15}$$

and since the nozzle velocity equals the nozzle flow rate Q_j divided by the nozzle area

$$V_s = \frac{Q_j}{\sqrt{A_j A_s}} \tag{4-16}$$

To determine the stream area we refer to Figure 4-6 and note

$$A_s = \theta\,[(R + h)^2 - R^2] \tag{4-17}$$

which when linearized for $\frac{h}{r} << 1$ gives

$$A_s \cong 2\theta R h \tag{4-18}$$

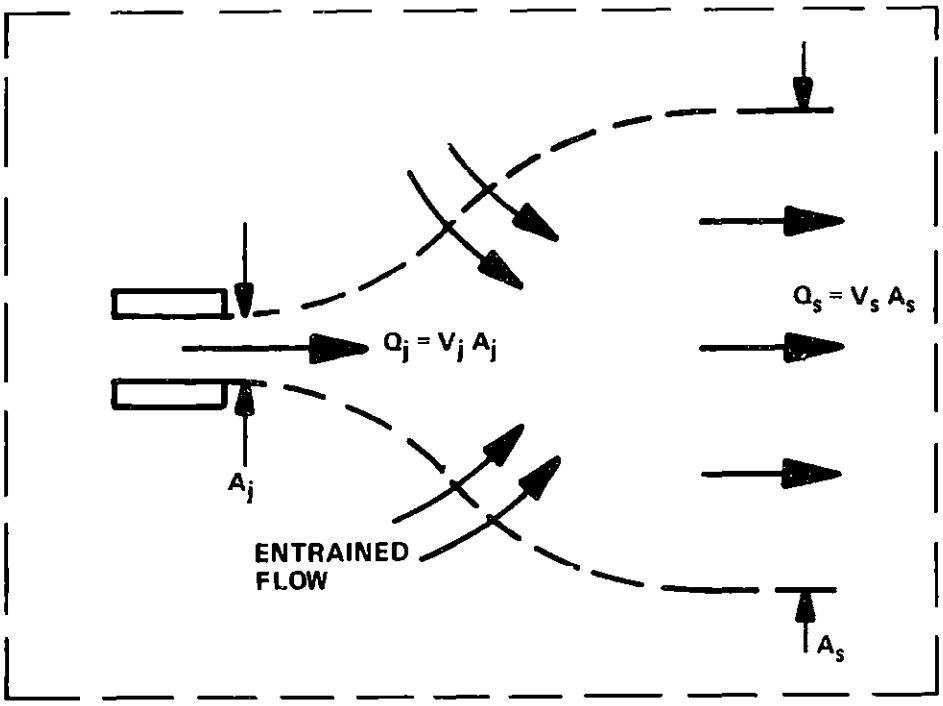

Figure 4-5. Control Volume for Jet Stream Momentum Analysis

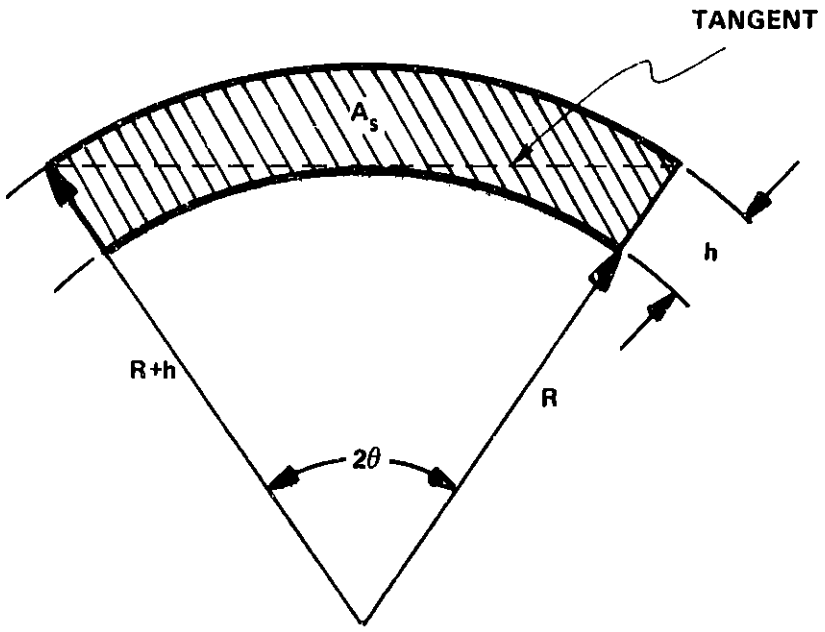

Figure 4-6. Geometric Approximation of Jet Stream Area

Trigonometry reveals that

$$\theta = \tan^{-1}\left[\frac{\sqrt{(R+H)^2 - R^2}}{R}\right] \tag{4-19}$$

which again when linearized for $\frac{h}{r} << 1$ yields

$$\theta \cong \sqrt{2\frac{h}{r}} \tag{4-20}$$

Combining (4-18) and (4-20) the stream area becomes

$$A_s = \sqrt{8Rh^3} \tag{4-21}$$

The pertinent parameters of jet geometry are therefore

$$V_s = \frac{Q_j}{\sqrt{A_j\sqrt{8Rh^3}}} \quad ; A_s = \sqrt{8Rh^3} \tag{4-22}$$

Further validation of the above approximations is given in Appendix B.

4.3.2 Momentum Calculations of Shear Force in Gap

The effectiveness of calculating surface shear forces using change of momentum principles lies in the successful choice of reasonable velocity profiles. The jet stream here was modelled as a quasi-two-dimensional channel flow between two parallel plates. The lower plate represents the inner sphere; the upper plate, the outer shell. (See Figure 4-7.) This planar assumption is quite reasonable since the gap h between the inner ball and outer shell is much much less than the radius of curvature R of the inner sphere. The flow is termed quasi-two-dimensional because the

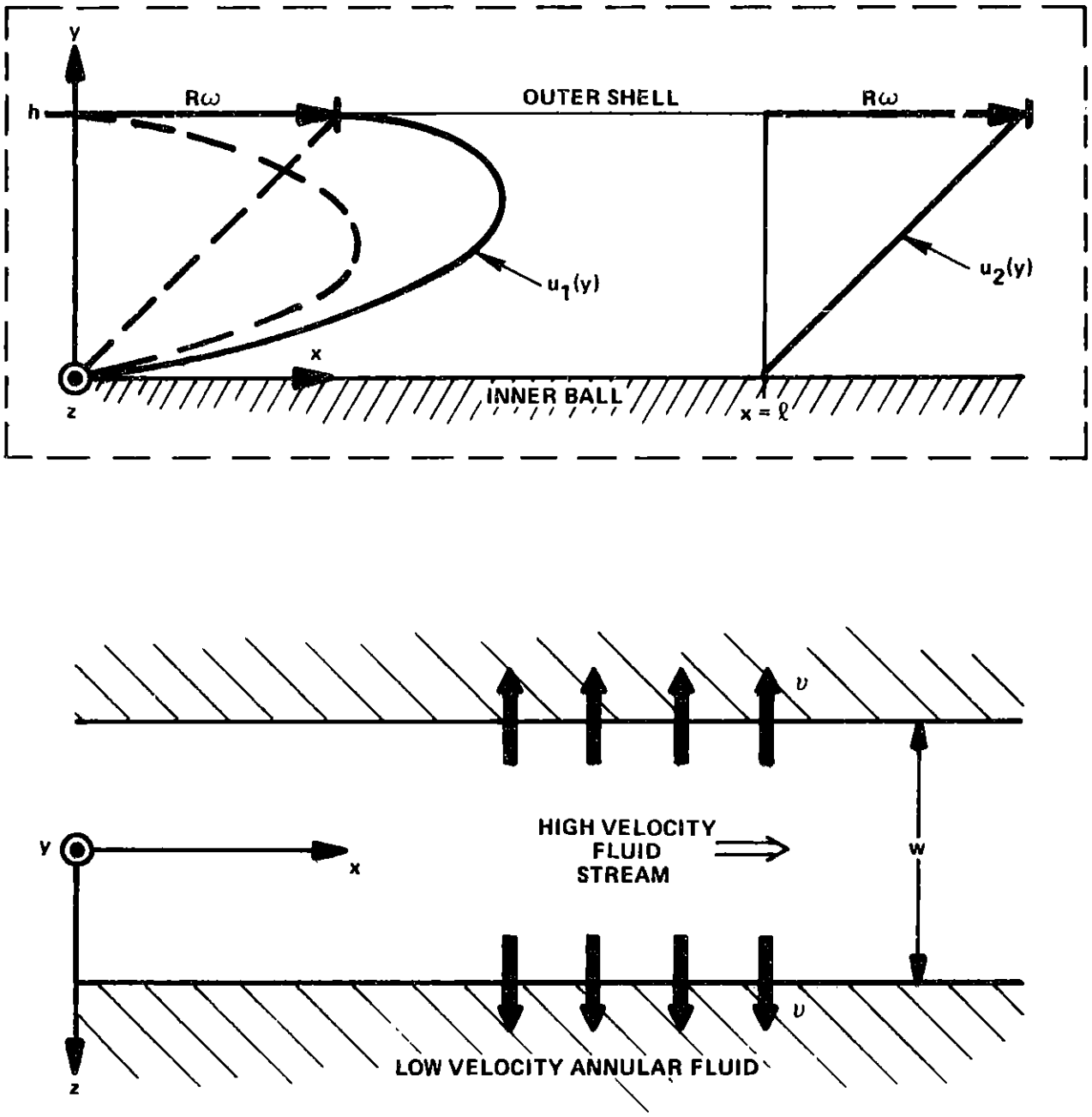

Figure 4-7. Assumed Velocity Profiles of Jet Stream

channel is assumed to have a finite width h along the z axis such that the stream cross-sectional area A_s is given by hw; however, end effects on the z faces are ignored.

Figure 4-7 shows the jet stream with its assumed velocity profiles and the control volume to be used for the analysis. The jet nozzle is squirted in from left of the figure. Profile 1 is taken several nozzle diameters downstream of the jet after the spreading region. It is envisioned as being formed by the superposition of a high velocity parabolic distribution from the jet and a linear distribution due to the rotation of the outer shell with respect to the inner ball at a relative velocity $R\omega$ where ω is the relative angular rotation rate of the shell in rad/sec. Far downstream the jet has lost most of its momentum and can no longer penetrate the annular fluid. The only velocity distribution remaining is that due to the relative motion between the inner ball and outer shell. The profiles are given by

$$u_1 = \frac{R\omega}{h} y + 6 V_s \left[\frac{y}{h} - \left(\frac{y}{h} \right)^2 \right] \qquad (4\text{-}23)$$

$$u_2 = \frac{R\omega}{h} y$$

The shear force may be calculated by integrating the momentum flux across the surfaces of the control volume, which in vector notation yields

$$F_x = \oiint_{C.S.} u \, (\rho \, \underline{V} \cdot d\underline{A}) \qquad (4\text{-}24)$$

or

$$F_x = w \int_0^h \rho \, u_2^2 \, dy - w \int_0^h u_1^2 \, dy + 2h \int_0^{\ell} \rho uv dx \qquad (4\text{-}25)$$

Since we are past the region where entrainment occurs we may use continuity of flow and dimensional analysis to determine the relative importance of the y direction velocity v.

The continuity equation for an imcompressible two-dimensional flow is

$$\frac{\partial u}{\partial x} + \frac{\partial v}{\partial y} = 0 \tag{4-26}$$

Noting that u scales as the average stream velocity, V_s, the x dimension scales with the stream length ℓ, and y dimension scales with the gap h we get

$$\frac{V_s}{\ell} \sim \frac{v}{h} \tag{4-27}$$

or since $\frac{v}{V_s} \sim \frac{h}{\ell}$ and $\frac{h}{\ell} << 1$ we can claim $v << V_s$ and v is therefore negligible. (Note this assumption is not valid in the spreading region since here ℓ is of the order h.) The momentum balance then reduces to

$$F_x = \rho w \int_0^h \left(u_2^2 - u_1^2 \right) dy \tag{4-28}$$

Substituting the profiles (equation (4-23)) and integrating we get

$$F_x = \rho V_s^2 w h \left(\frac{R\omega}{V_s} + \frac{6}{5} \right) \tag{4-29}$$

and since $wh = A_s$ the relation reduces to

$$F_x = \rho V_s^2 A_s \left(\frac{R\omega}{V_s} + \frac{6}{5} \right) \tag{4-30}$$

where V_s and A_s were given by equations (4-21) and (4-22). An alternate form based on equation (4-16) is

$$F_x = \rho \frac{Q_j^2}{A_j} \left(\frac{R\omega}{V_s} + \frac{6}{5} \right)$$

4.3.3 Transformation of Shear Force into Drag Torque

The shear force calculated in the previous section is the total force exerted on both the inner ball and the outer shell. It is necessary to determine what fraction of that force acts on the inner sphere. One cannot á priori claim that the force is equally divided between the inner and outer members since the assumed velocity profiles clearly show different slopes at each surface. A ratio of the outer force F_{out} to the inner force F_{in} can be found by taking a ratio of the shear stress on the outer surface to the shear stress on the inner surface since in the planar model the areas they act on are equal.

$$\frac{F_{out}}{F_{in}} = \frac{\tau_{out}}{\tau_{in}} \qquad (4\text{-}32)$$

The ratio of outer to inner shear stress can be found by investigating the ratios of the slopes of the velocity profiles at the outer and inner surfaces.

Differentiation of equation (4-23) yields

$$\frac{du_1}{dy} = \frac{R\omega}{h} + \frac{6V_s}{h}\left[1 - 2\frac{y}{h}\right] \tag{4-33}$$

$$\frac{du_2}{dy} = \frac{R\omega}{h}$$

We are now in the position to assume a distribution of our shear stress. For simplicity let us assume a linear one

$$\tau_{out} = (\tau_2 - \tau_1)_{out}\ \frac{x}{\ell} + \tau_{1\ out} \tag{4-34}$$

$$\tau_{in} = (\tau_2 - \tau_1)_{in}\ \frac{x}{\ell} + \tau_{1\ in} \tag{4-35}$$

where the subscripts 1 and 2 refer to stress at the point of the correspondingly numbered assumed velocity profiles. Since we are dealing with a Newtonian fluid we may set the shear stresses 1 and 2 proportional to the slope of the velocity profiles at these points such that

$$\tau_{1\ in} = \mu_{mom} \left.\frac{du_1}{dy}\right|_{y = 0} \tag{4-36}$$

$$\tau_{2\ in} = \mu_{mom} \left.\frac{du_2}{dy}\right|_{y = 0} \tag{4-37}$$

$$\tau_{1\ out} = \mu_{mom} \left.\frac{du_1}{dy}\right|_{y = h} \tag{4-38}$$

$$\tau_{2\ out} = \mu_{mom} \left.\frac{du_2}{dy}\right|_{y = h} \tag{4-39}$$

The constant of proportionality in this case is μ_{mom} which may be termed a "momentum viscosity".

One might ask at this point why the shear stresses were not just calculated directly from the slope of the velocity distribution instead of using the momentum method. Similar calculations for the shear stresses using the usual viscosity coefficient of the fluid yielded results far too low. This is due to the fact that the jet stream may not be purely laminar. Error may also have been introduced in the assumed velocity distributions which becomes magnified when differentiated. Since integration is a smoothing process the momentum method is preferable since it integrates over the assumed velocity profiles only in the form of a ratio. Since it is very probable that any percentage errors made are of the same order of magnitude they should cancel or at least be diminished in the ratio.

The ratio of the outer to inner shear force is given by integrating the shear stress along the shear length ℓ

$$\frac{F_{out}}{F_{in}} = \frac{\int_0^{\ell} \left[\tau_{2\ out} \frac{x}{\ell} + \left(1 - \frac{x}{\ell}\right) \tau_{1\ out} \right] dx}{\int_0^{\ell} \left[\tau_{2\ in} \frac{x}{\ell} + \left(1 - \frac{x}{\ell}\right) \tau_{2\ in} \right] dx} \tag{4-40}$$

After substitution of equations (4-36) through (4-39) and integration, the ratio reduces to

$$\frac{F_{out}}{F_{in}} = \frac{R\omega - 9V_s}{R\omega + 9V_s} = \frac{\frac{R\omega}{9V_s} - 1}{\frac{R\omega}{9V_s} + 1} \tag{4-41}$$

the unknown quantities μ_{mom} and ℓ conveniently cancelling in the ratio.

A plot of equation (4-41) is shown in Figure 4-8. At very high $\omega >> \frac{9V_s}{R}$ the curve is asymptotic to 1, which indicates that in the limit of no jet stream we have a linear profile.

Noting the identity

$$\frac{F_{out}}{F_{in}} + \frac{F_{in}}{F_{in}} = \frac{F_{total}}{F_{in}} \tag{4-42}$$

we may manipulate to get the following expression

$$F_{in} = \frac{1}{1 + \frac{F_{out}}{F_{in}}} \; F_{total} \tag{4-43}$$

To obtain the shear torque on the linear member we need only multiply by the moment arm R.

$$T_{in} = \frac{1}{1 + \left| \frac{\frac{R\omega}{9V_s} - 1}{\frac{R\omega}{9V_s} + 1} \right|} \rho \frac{Q_j^2}{A_j} R \left\{ \frac{R\omega}{V_s} + \frac{6}{5} \right\} \tag{4-44}$$

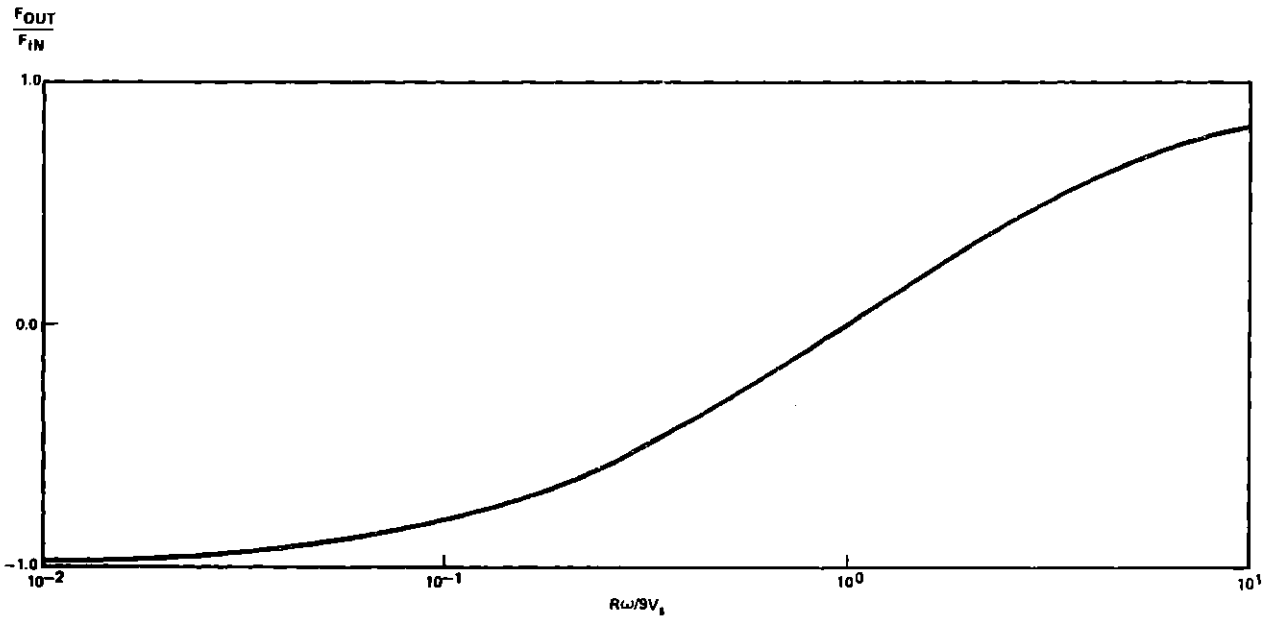

Figure 4-8. Drag Force Distribution Versus Normalized Relative Rotation Rate of Outer Shell

4.3.4 Calculation of Stall Thrust

Consider the system consisting of the inner ball and outer shell to have reached a steady state in which the relative velocity between the two members is zero. When the valves are ejecting fluid at a particular flow rate, the thrust required to maintain the ball in this equilibrium position is termed stall thrust. The stall thrust can be obtained from equation (4-44) by setting ω equal to zero and dividing by the moment arm R

$$F_{stall} = \frac{3}{5} \rho \frac{Q_j^2}{A_j} \qquad (4\text{-}45)$$

Calculated values for the stall thrust about a spin axis are compared with measured values in Figure 4-9. The current design has four jets per axis. The thrust of the combined force of all four jets is plotted versus the total flow to all four nozzles. Figures 4-10 and 4-11 are similar plots for older designs with only two jets per axis.

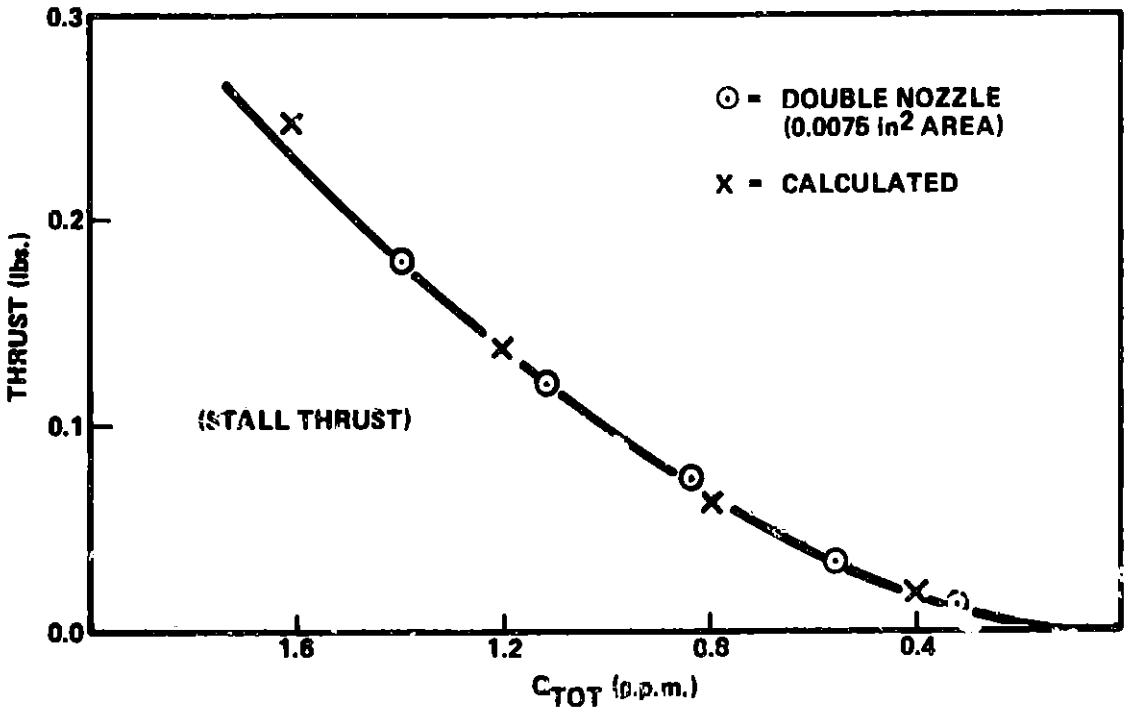

Figure 4-9. Stall Thrust Versus Total Jet Pair Flow for Current Double Nozzle Design

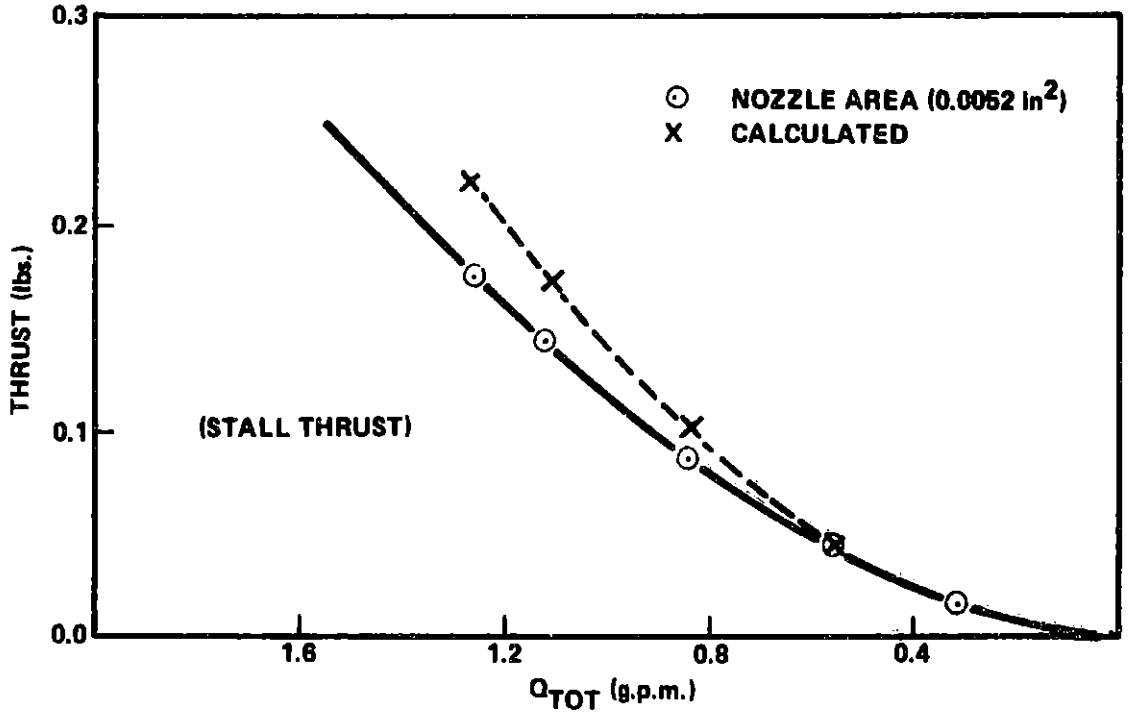

Figure 4-10. Stall Thrust Versus Total Jet Pair Flow for .0052in.^{2} Nozzle Area

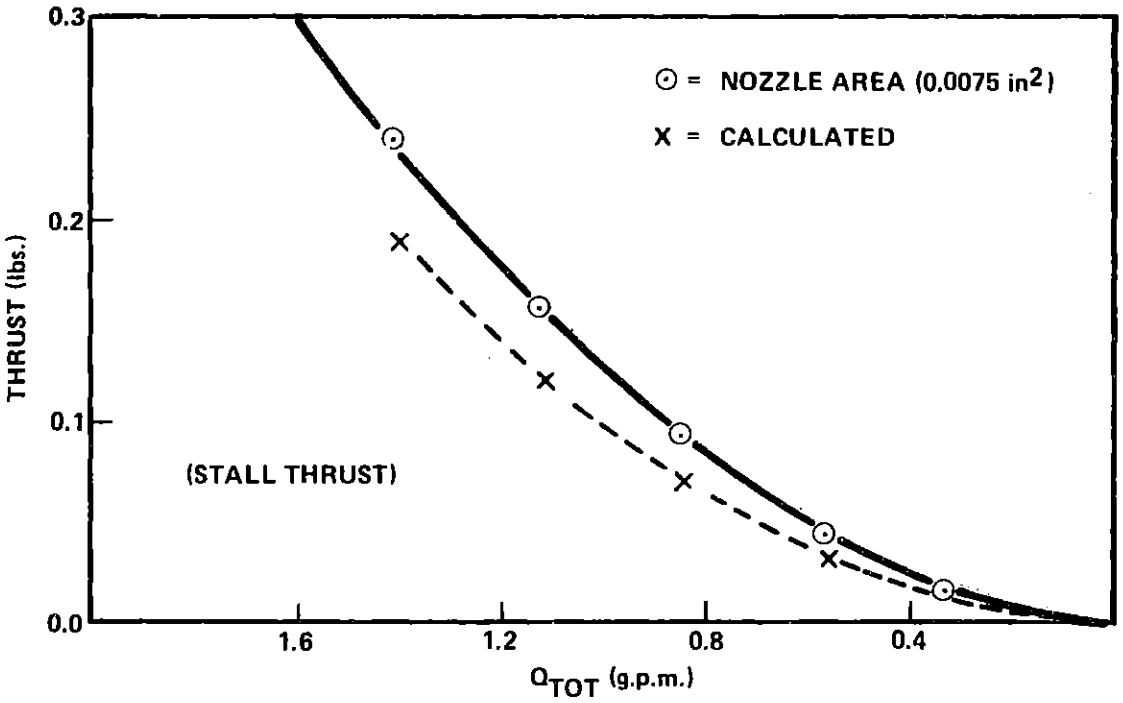

Figure 4-11. Stall Thrust Versus Total Jet Pair Flow for .0075in.^{2} Nozzle Area

4.4 Steady State Torquing Ability and Load Line

Based on equation (4-44) a steady state load line can be established for the system's available torque. The system's available torque is given by the ideal valve torque minus that torque which produces a parasitic drag on the inner sphere or

$$T_{avail} = T_{ideal} - T_{in} \tag{4-46}$$

Since the ideal valve torque T_{ideal} is given by

$$T_{ideal} = \rho \frac{Q_j^2}{A_j} R \tag{4-47}$$

equations (4-47) and (4-44) can be substituted into (4-46) to yield

$$T_{avail} = \rho \frac{Q_j^2}{A_j} R \left[1 - \frac{1}{1 + \left| \frac{\frac{R\omega}{V_s} - 1}{\frac{R\omega}{V_s} + 1} \right|} \left\{ \frac{R\omega}{V_s} + \frac{6}{5} \right\} \right] \tag{4-48}$$

The bracketed term may be called an annulus recovery coefficient (ARC) and is plotted versus the non-dimensional parameter $\frac{R\omega}{V_s}$ in Figure 4-12.

As can be seen from the figure the data points are fitted very well by a straight line with the equations

$$ARC = .4 - .6 \frac{R\omega}{V_s} \tag{4-49}$$

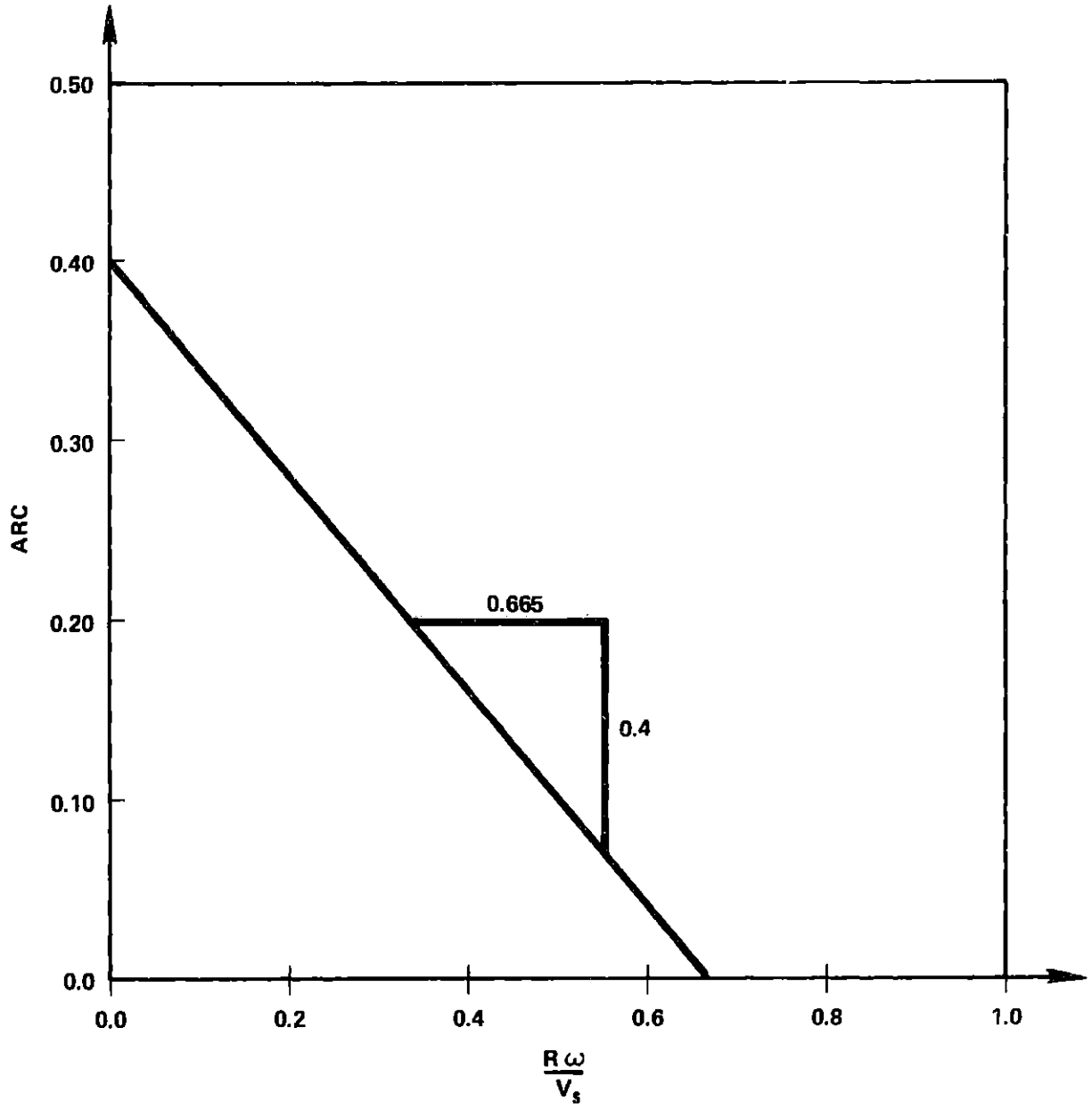

Figure 4-12. Annulus Recovery Coefficient Versus Normalized Relative Rotation Rate of Outer Shell

Substitution of equivalent system parameters for V_s in equation (4-49) gives

$$ARC = .4 - .6\left(\frac{2\pi R\sqrt{A_j\sqrt{8Rh^3}}}{Q_j}\right)\omega \qquad (4\text{-}50)$$

where the 2π has been added so that ω may be given in cps.

The available torque may be found by substituting equation (4-50) into equation (4-48)

$$T_{avail} = \frac{\rho Q_j^3}{A_j} R\,(ARC) = \frac{\rho Q_j^2}{A_j} R\left[.4 - .6\left(\frac{2\pi R\sqrt{A_j\sqrt{8Rh^3}}}{Q_j}\right)\omega\right] \qquad (4\text{-}51)$$

Once the available torque of the system is known it is compared with the system load line to determine its adequacy or inadequacy. The load which the torquing system must sustain is composed of torques from the form drag of the suspension pads, the frictional drag of the brushes, and the viscous drag of the outer shell pulling the annular fluid along with it as it rotates. The pad and brush torques were found in previous sections. The viscous shear torque due to the concentric rotation of a shell outside a sphere is negligibly small compared with the first two. (For this system the shear torque would be .02 in-oz at a speed of 2 cps.) The solid lines in Figure 4-13 show the available torque and load line for the present system (ball radius = 4.25 in.).

At first one's instinct is to have a large radius ball so that the valve thrusts are acting at a large moment arm, giving a larger torque. From a hydraulics point ov view, however, it is advantageous to have a small ball. The slope of the available torque curve is directly proportional to the slope of the ARC versus $\frac{R\omega}{V_s}$ curve (Figure 4-12). Equation (4-50) shows that this slope increases with $R^{5/4}$. A steep slope implies that the available torque falls off rapidly with speed so a shallower slope

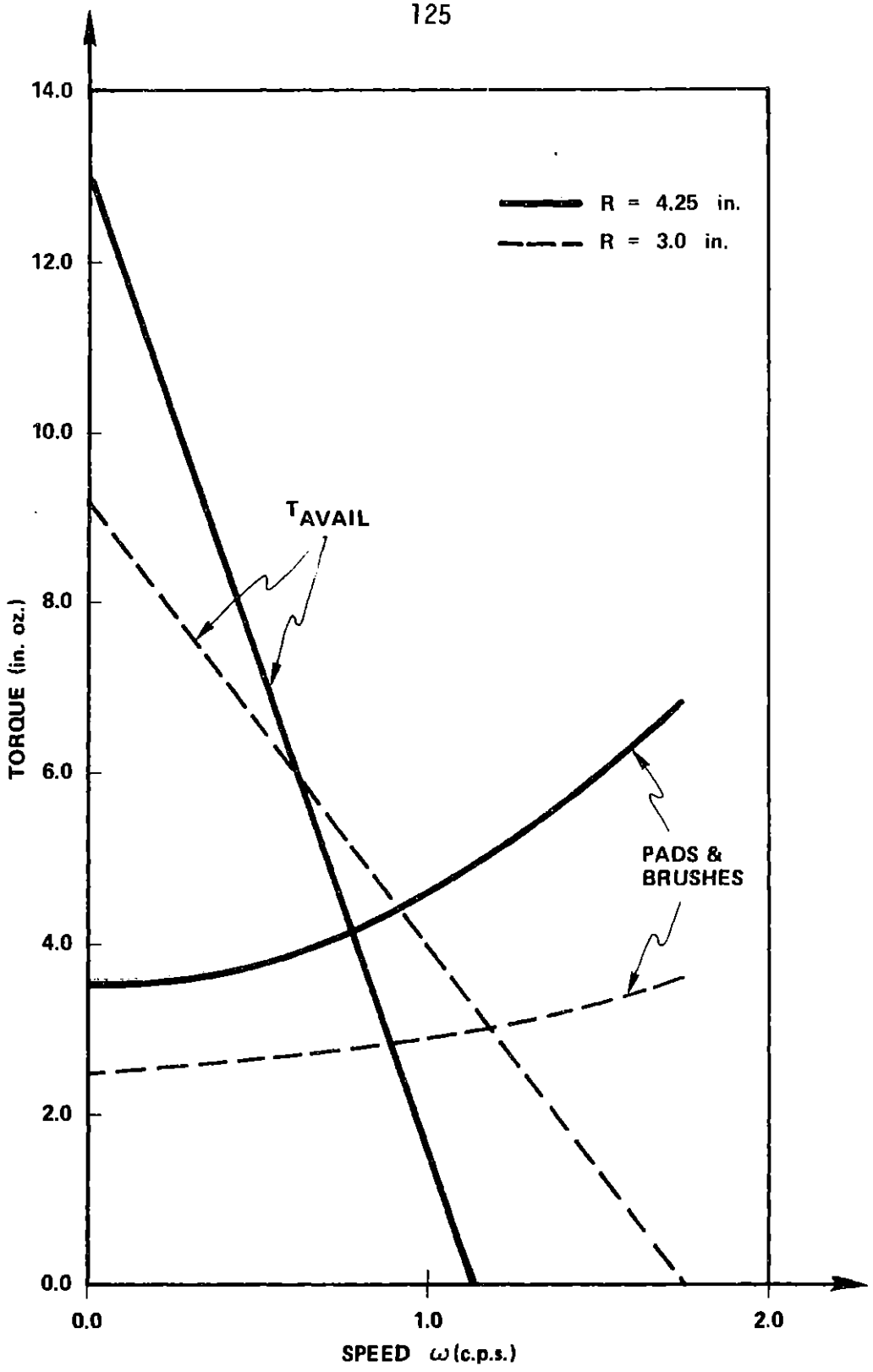

Figure 4-13. Load Line for Torquing Subsystem Showing Effect of Ball Radius. Load Due to Parasitic Drag of Jet Wake Has Been Subtracted from Ideal Valve Torque to Give an Available Torque Rather Than Added to the Load of the Pads and Brushes

is desirable. The form drag of the pads increase as R^3 (see Section 4.2) so again a small radius is favored. The dashed lines in Figure 4-13 represent the same hydraulic system operating on a 3-inch radius ball. The hydraulics acting on a 4.25-inch radius ball are adequate to about .76 cps. The same system acting ona 3-inch radius ball has a range of adequacy which extends to about 1.2 cps. A 30% decrease in ball radius produced a 58% increase in range of performance.

Figure 4-14 illustrates the effect of the annular gap h on the load line and available torque. Since the ARC varies as $h^{3/4}$ (see Equation (4-51)) the slope of the available torque versus speed becomes less steep at smaller gaps. To maintain the pad clearance necessary for a specified suspension force, the suspension pads would not need to protrude as far out from the sphere surface as they would if the gap were larger. Since the form drag is proportional to the area of these pads projected normal to the flow, a pad which protrudes less accures less drag torque. It is true that the laminar shear due to the rotation of the outer shell about the inner sphere is inversely proportional to the gap and this drag contribution would, therefore, increase at smaller gaps. However, again this contribution is negligible. (For a .075 inch gap this shear torque would rise to only .04 in-oz at a speed of 2 cps.) A decrease in the annular gap, therefore, proves beneficial rather than detrimental. From Figure 4-14 it is seen that an annular gap of .15 inch yields a system adequate to .76 cps (solid lines). The dashed lines show an annular gap of .075 inch increases the range of system to 1.25 cps. A 50% decrease in gap produced a 64% increase in system performance.

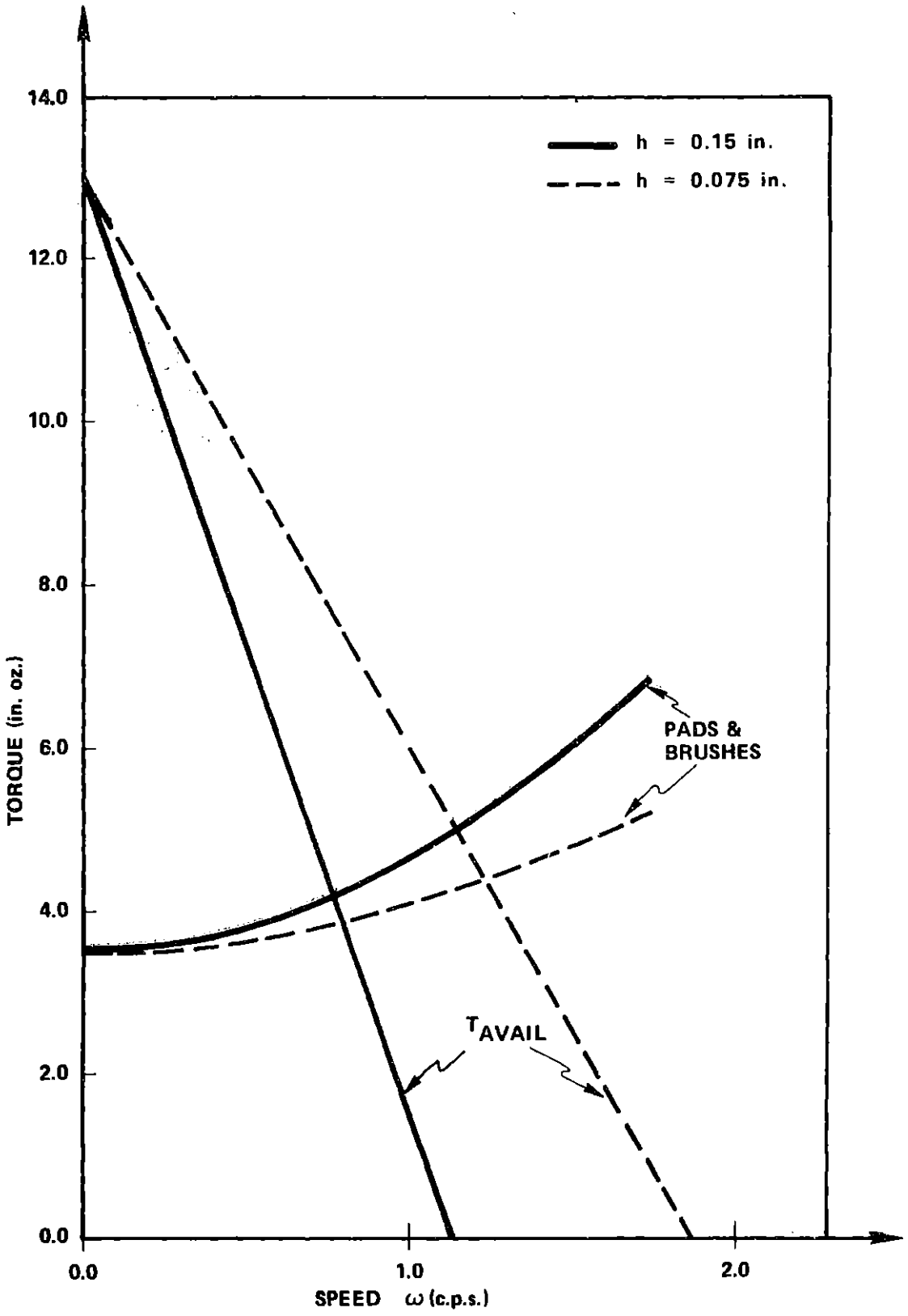

Figure 4-14. Loadline for Torquing Subsystem Showing Effect of Annular Size Gap

4.5 Rotational Dynamics

A steady state load line analysis of a system provides much useful information; but a dynamic analysis is also needed to determine the system's behavior as it approaches the steady state values previously calculated. Since the objective of the entire torquing system is to eliminate rotational motions of the ball with respect to an inertial frame, it would be advantageous to know the time variance of these angular motions. This section considers rotation about one axis with one torquer jet pair in full torquing operational mode. The axis chosen is perpendicular to the face of the imaginary cube superscribed about the sphere so that the torquing axis of the jet pair coincides with the spin axis of the sphere.

An electric analog modeling the rotational system is shown in Figure 4-15. As set forth in the introduction, torque corresponds to current, angular velcoity to voltage, capacitance to inertances, etc. The symbols used follow the conventions set up in Figure 1-8. The ball is modeled as a spherical mass with rotary moment of inertia J about the spin axis and angular velocity Ω_B. The pads are modeled as a rotary damper whose torque T_{pads} is given by a constant B times the square of the relative angular velocity between the ball and shell, ω. The brushes act as a torque source of magnitude, $T_{brushes}$, while the shell is an angular velocity source of strength Ω_C.

The chosen model for the jets requires some explanation. As derived in the previous section, the available torque of the jets can be given by

$$T_{avail} = T_{ideal}\left(.4 - .6\ \frac{R\omega}{V_s}\right) \qquad (4\text{-}52)$$

where a previously defined R was the ball radius V_s the jet stream velocity relative to the ball, and ω the relative velocity between the ball and shell.

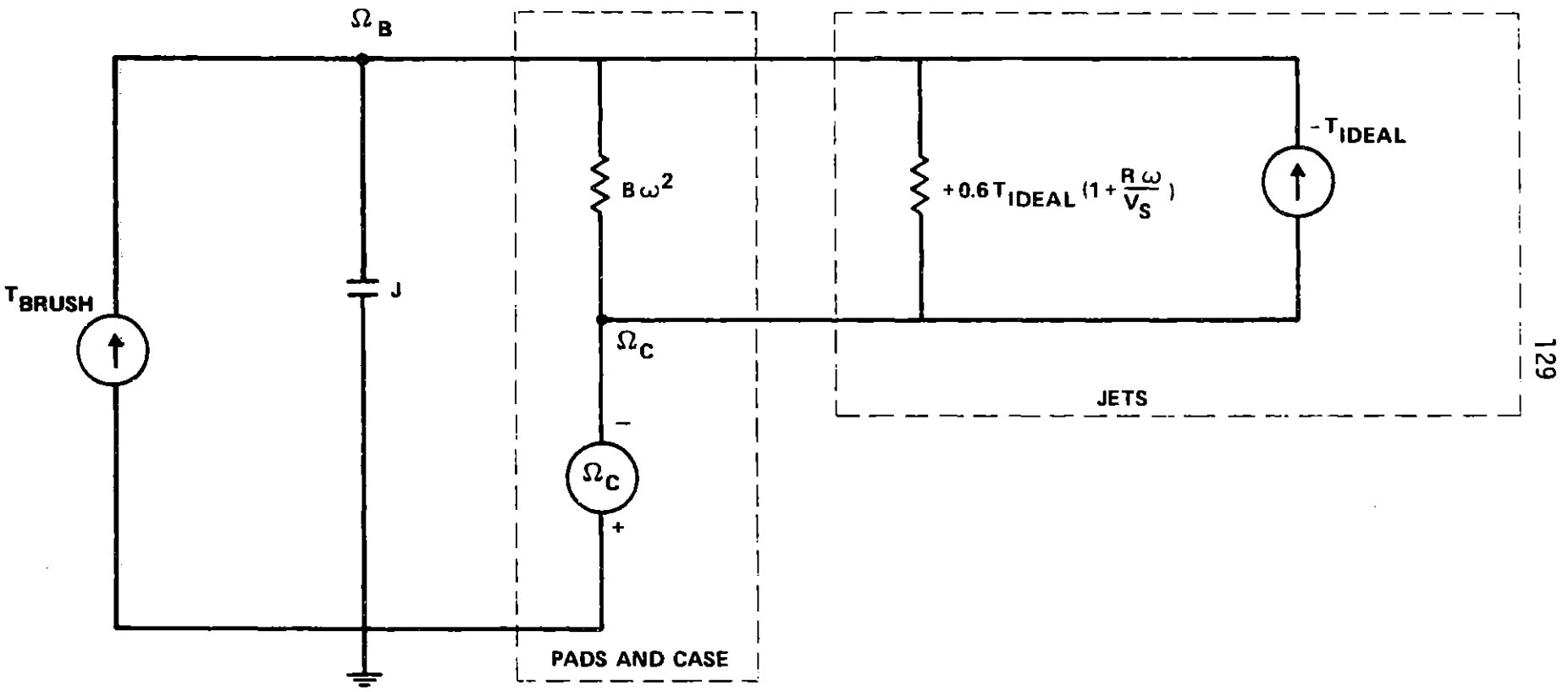

Figure 4-15. Electrical Analog of Rotational System

This equation can be rewritten as

$$T_{avail} = T_{ideal} - .6\,T_{ideal}\left(1 + \frac{R\omega}{V_s}\right) \tag{4-53}$$

In this format it is easier to see how the jets may be modeled as a torque source in parallel with a resistance. The reason for the minus sign in the analog circuit is that the reaction torque of the jets is in a direction opposite to that of the pads and brushes. A schematic torque balance diagram is shown in Figure 4-16.

Based on the torque balance of Figure 4-16 the differential equation of rotational motion for this system is

$$J\dot{\Omega}_B = T_{pads} + T_{brushes} + T_{jets} \tag{4-54}$$

Using the relationships from Figure 4-15 the equation becomes

$$J\dot{\Omega}_B = B(\Omega_C-\Omega_B)^2 + T_{brushes} - T_{ideal} + .6T_{ideal}\left[1 + \frac{R}{V_s}(\Omega_C-\Omega_B)\right] \tag{4-55}$$

Defining the relative velocity $\Omega_C-\Omega_B$ as ω we see that

$$\omega = \Omega_C-\Omega_B \tag{4-56}$$

$$\dot{\omega} = \dot{\Omega}_C-\dot{\Omega}_B = -\dot{\Omega}_B$$

since the case velocity Ω_C is assumed constant with time. Substituting into equation (4-55) and manipulating gives

$$\dot{\omega} = -\frac{B}{J}\omega^2 - \frac{.6T_{ideal}}{V_s}\frac{R}{J}\omega + \frac{T_{ideal} - T_{brush}}{J} - \frac{.6T_{ideal}}{J} \tag{4-57}$$

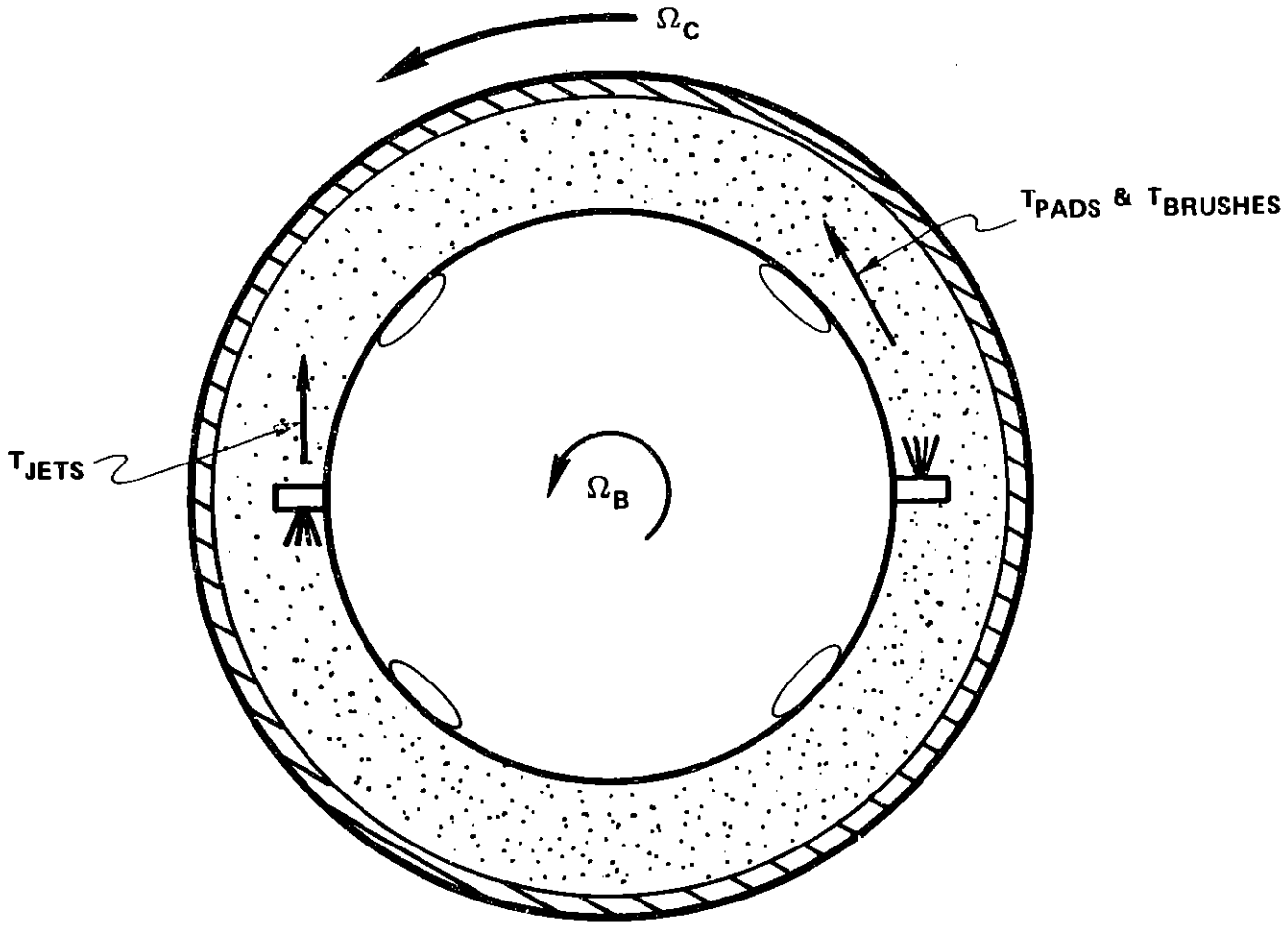

Figure 4-16. Torque Balance Diagram for Rotational System

It is at this point that some deviation from the static mode for the jets must be made. At the instant the jets are turned on full, the sphere is subjected to the fully ideally calculated reaction torque. This situation occurs because at that point in time, the wake of the jet stream has not been established and therefore cannot exert the parasitic drag force on the sphere as described in Section 4.3. To account for this circumstance the model must be extended. The simplest simulation to approximate this phenonmenon is to assume that the ball feels the full ideal torque, T_{ideal}, for a specified amount of time, t'. At times greater than t' the ball feels the available torque as prescribed in Section 4.3. In other words, for t<t' the rightmost resistance of Figure 4-14 is assumed to be non-existent. Figure 4-17 shows the approximation to the jet torque assumed.

Equation (4-57) then becomes two equations, one for each time regime. They are, for 0<t<t'

$$\dot{\omega} = -\frac{B}{J}\omega^2 + \frac{T_{ideal} - T_{brush}}{J} \tag{4-58}$$

and for t'<t

$$\dot{\omega} = -\frac{B}{J}\omega^2 - \frac{.6T_{ideal}}{J}\frac{R}{V_s}\omega + \frac{.4T_{ideal} - T_{brush}}{J} \tag{4-59}$$

Both of these equations are of the form

$$\dot{\omega} = \alpha\omega^2 + \beta\omega + \gamma \tag{4-60}$$

and are separable.

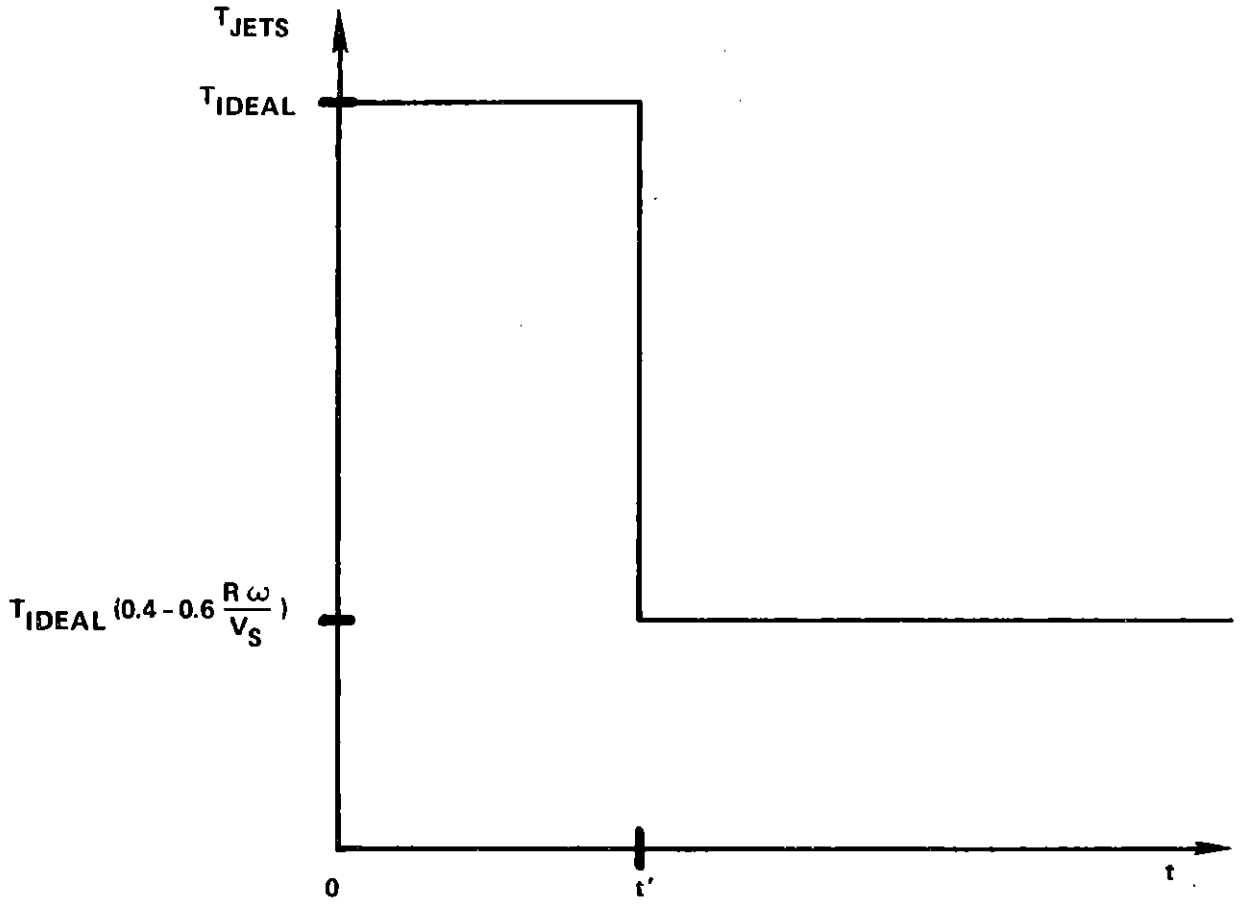

Figure 4-17. Jet Torque as a Function of Time

The values for the constants, α, β, γ and δ must be found from the system constants B, J, T_{ideal}, $T_{brushes}$, R, and V_s.

All calculations are done on a 4.25 inch radius ball. The damping constant of the pads B can be obtained from equation (4-11). It can be seen that

$$B = .653\ \rho\ A_{proj}\ R^3 \tag{4-11}$$

A good estimate for the rotary moment of inertia of the ball J can be found from the equation for the moment of inertia for a sphere. The mass of the ball was found from the product of its volume and density. Since the ball is approximately neutrally buoyant, the fluid density is about equal to the ball density. Hence,

$$J = \frac{2}{5}\left(\rho\ \frac{4}{3}\ \pi R^3\right)\ R^2 = \frac{8}{15}\ \pi\rho R^5 \tag{4-65}$$

The ideal torque of the jets was given by equation (4-47) as

$$T_{ideal} = \rho\ \frac{Q_j^2}{A_j}\ R \tag{4-47}$$

while the brush torque was given by equation (4-5) as

$$T_{brushes} = 6.53\ \eta F_n R \tag{4-5}$$

The stream velocity is given by

$$V_s = \frac{Q_j}{\sqrt{A_j \sqrt{8Rh^3}}} \tag{4-22}$$

For this system the numeric values for these constants become

$$\begin{aligned} B &= 1.8 \times 10^{-3} \text{ in.lb sec}^2 \\ J &= .388 \text{ in. lb sec}^2 \\ T_{ideal} &= 32 \text{ in. oz} = 2 \text{ in. lb} \\ T_{brushes} &= 3.5 \text{ in. oz} = .22 \text{ in. lb} \\ R &= 4.25 \text{ in.} \\ V_s &= 46 \text{ in./sec} \end{aligned} \tag{4-66}$$

The values α, β, γ and δ may now be found. A comparison of terms between equations (4-58) and (4-60) and substitution of the values computed from equation (4-66) show that

$$\begin{aligned} \alpha &= -\frac{B}{J} = -4.639 \times 10^{-3} \\ \beta &= 0 \\ \gamma &= \frac{T_{ideal} - T_{brushes}}{J} = 4.588/\text{sec}^2 \\ \delta &= 2.918 \times 10^{-1}/\text{sec} \end{aligned} \tag{4-67}$$

For $0 < t < t'$. For these values of α, β, γ and δ the $\tanh^{-1}$ solution may be used when

$$-3.145 \times 10^{1}/\text{sec} < \omega < 3.145 \times 10^{1}/\text{sec} \qquad (4\text{-}68)$$

and the ln solution when

$$\omega < 3.145 \times 10^{1}/\text{sec} \qquad (4\text{-}69)$$

Since the lower limit of integrations is Ω_C (at $t = 0$, $\Omega_B = 0$) the $\tanh^{-1}$ is chosen. Equation (4-61) becomes

$$t = \frac{-2}{\delta}\left[\tanh^{-1}\left(\frac{2\alpha\omega+\beta}{\delta}\right) - \tanh^{-1}\left(\frac{2\alpha\Omega_C+\beta}{\delta}\right)\right] \qquad (4\text{-}70)$$

which when solved for ω becomes

$$\omega = \frac{1}{2\alpha}\left\{\delta\tanh\left[\frac{-\delta t}{2} + \tanh^{-1}\left(\frac{2\alpha\Omega_C+\beta}{\delta}\right)\right] - \beta\right\} \qquad (4\text{-}71)$$

Note that as $t \to \infty$ the solution asymptotically approaches

$$\omega \to \frac{-\beta-\delta}{2\alpha} = 3.145 \times 10^{1}/\text{sec} \qquad (4\text{-}72)$$

so there is no danger of going beyond the region of validity of the solution chosen.

Equation (4-71) is a solution to equation (4-61) only for $t < t'$. We evaluate (4-71) at $t = t'$ and use the value for ω as the lower limit of the integral for times greater than t' when the jet torque experiences the step reduction. For $t > t'$ the constants α, β, γ and δ must be re-evaluated. A comparison of terms between equations (4-59) and (4-60) when the values of equation (4-66) are substituted yields

$$\begin{aligned} \alpha &= -\frac{B}{J} = -4.63 \times 10^{-3} \\ \beta &= \frac{-.6T_{ideal}}{J}\frac{R}{V_s} = -2.857 \times 10^{-1}/\text{sec} \\ \gamma &= \frac{.4T_{ideal}-T_{brushes}}{J} = 1.495/\text{sec}^2 \\ \delta &= 3.307 \times 10^{-1}/\text{sec} \end{aligned} \tag{4-73}$$

For these values of α, β, γ and δ the $\tanh^{-1}$ solution is valid when

$$-6.644 \times 10^{1}/\text{sec} < \omega < 4.850/\text{sec} \tag{4-74}$$

and the ln solution when

$$4.850/\text{sec} < \omega \tag{4-75}$$

Our choice of solution will depend upon the value of ω at $t = t'$.

Up until now a value for t' has not been chosen. Physically there can be no specific time t' when the drag of the jet wake takes effect. Rather, the drag gradually increases as the jet wake covers more sphere surface area. An approximation, however, is that the drag effect can be ignored until the two jet wakes cover one half the ball circumference or that each jet must have traveled one quarter of the way around the ball. Dividing this distance by the velocity of the jet stream will give the time elapsed until this situation occurs.

$$t' = \frac{\frac{1}{4} 2\pi R}{V_s} = .145 \text{ sec} \tag{4-76}$$

Substitution of this value for t' into equation (4-71) gives ω at this time, ω', which depends upon the case velocity. A few values are given below for particular case velocities.

$$\begin{aligned} \Omega_C &= 3\pi \frac{\text{radians}}{\text{sec}} & \omega' &= 10.028 \frac{\text{radians}}{\text{sec}} \\ \Omega_C &= 2\pi \frac{\text{radians}}{\text{sec}} & \omega' &= 6.919 \frac{\text{radians}}{\text{sec}} \\ \Omega_C &= \frac{3\pi}{2} \frac{\text{radians}}{\text{sec}} & \omega' &= 5.360 \frac{\text{radians}}{\text{sec}} \\ \Omega_C &= \pi \frac{\text{radians}}{\text{sec}} & \omega' &= 3.799 \frac{\text{radians}}{\text{sec}} \end{aligned} \tag{4-77}$$

For case velocities 3π radians/sec, 2π radians/sec and $3\pi/2$ radians/sec the ln solution must be used. When $\Omega_C = \pi$ the $\tanh^{-1}$ solution must be used. Let us consider the solution for $\Omega_C \geq \frac{3\pi}{2} \frac{\text{radians}}{\text{sec}}$ since it is the higher case velocities which are more critical.

Integration of equation (4-61) between t' and t yields

$$t-t' = \frac{1}{\delta} \ln\left[\frac{2\alpha\omega + \beta - \delta}{2\alpha\omega + \beta + \delta}\right]_{\omega'}^{\omega} \tag{4-78}$$

Defining the constant

$$K \equiv \frac{2\alpha\omega' + \beta - \delta}{2\alpha\omega' + \beta + \delta} \tag{4-79}$$

equation (4-78) can be solved for ω to give

$$\omega = \frac{\frac{-\beta-\delta}{2\alpha} + \frac{\beta+\delta}{2\alpha} K e^{\delta(t-t')}}{1 - K e^{\delta(t-t')}} \tag{4-80}$$

As $t \to \infty$ reaches its steady state value.

$$\omega \to \frac{-\beta-\delta}{2\alpha} = 4.85 \text{ radians/sec} \tag{4-81}$$

A plot of equation (4-80) is shown in Figure (4-18) for different case velocities. As seen in the figure the case velocity does not affect the time asymptotic steady state value for the relative rotation rate between the ball and shell ω. (Had the $\tanh^{-1}$ solution been used as would have been necessary for the lower case velocity values it too would have approached this asymptotic value for ω. The only difference in the two solutions is that each approaches the value from a different direction due to different initial conditions impoed by ω'.) This steady state value checks with that which would have been obtained by setting $\dot{\omega} = 0$ in equation (4-60) and using the quadratic formula to solve for ω.

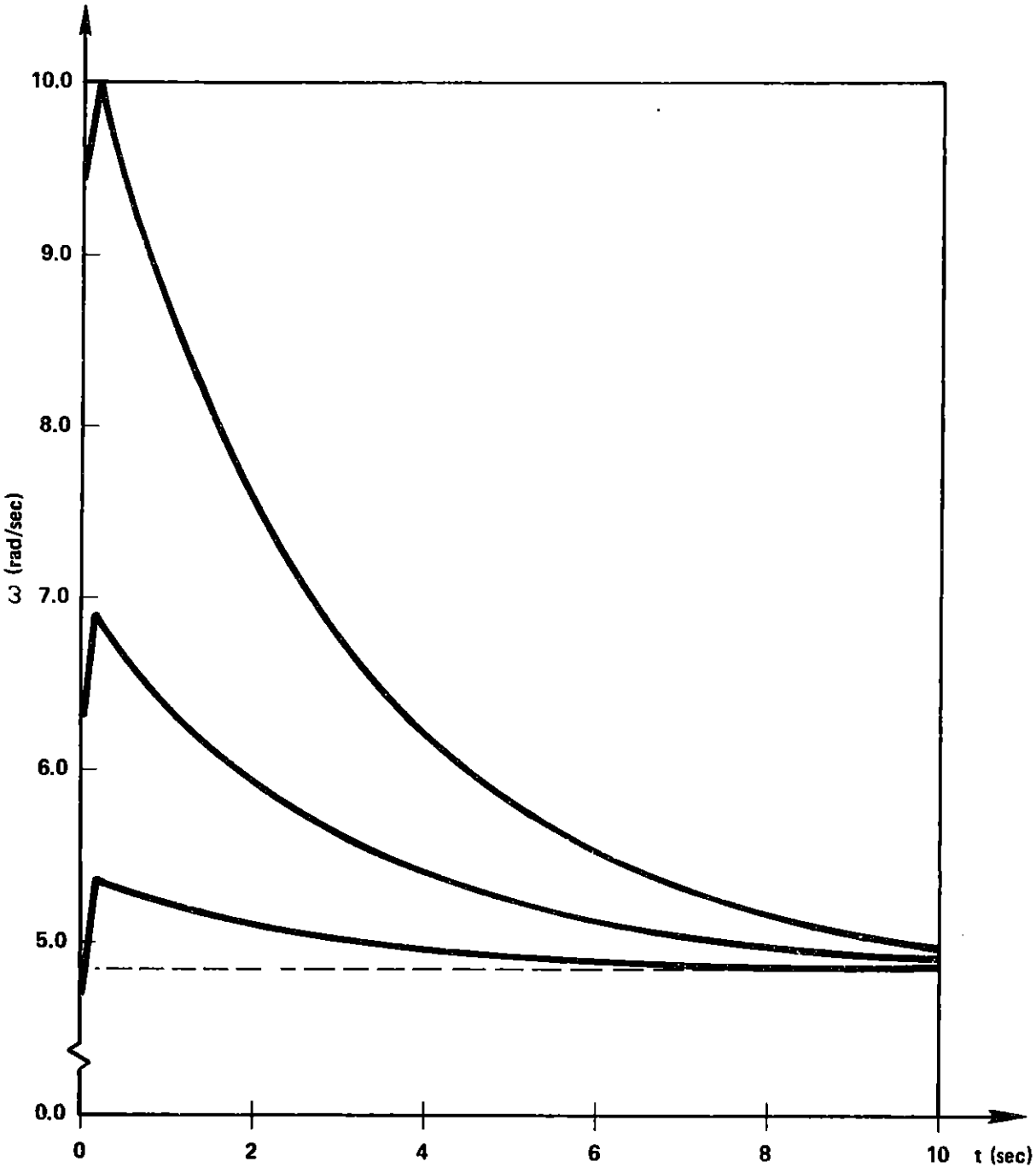

Figure 4-18. Relative Rotation Rate Between Ball and Shell as a Function of Time

Since it is the absolute motion of the ball itself which is of concern a more useful plot would be that of the ball rotational velocity Ω_B versus time. The ball velocity was given by equation (4-56) as $\Omega_C - \omega$. Figure 4-19 replots the information in a more intuitive form. To determine the position of the ball versus time these plots have to be integrated.

It is interesting to note the significance of the short initial time period $0 < t < t'$ when the jets produce an ideal torque value. From Figure 4-19 the ball velocity looks approximately linear with the time during this period and can be written as

$$\Omega_B \cong \frac{.65}{.145} t = -4.33\ t \qquad (4\text{-}82)$$

Integrating this equation from 0 position ($\theta_B = 0$) at time t_o to the ball position θ_B at time t' gives

$$\theta_B = -.045 \text{ radians} = -2.6° \qquad (4\text{-}83)$$

This implies that the ball has rotated slightly in a direction opposite that of the outer shell rotation. It, therefore, has a slight advantage when it begins to rotate in the opposite direction in its attempt to track the outer shell. To ignore the effect of the short duration of T_{ideal} is to throw out this favorable bias.

The ball velocity for $\Omega_C = \frac{3\pi}{2}$/sec never crosses above the t axis; i.e., it never becomes positive, never is in the same direction as the outer shell. This is indicative that at lower case velocities the jet torque is too strong. This can be compensated by shutting it off at appropriate times and turning it back on when needed. Conversely, the curves for $\Omega_C = 3\pi$/sec and 2π/sec

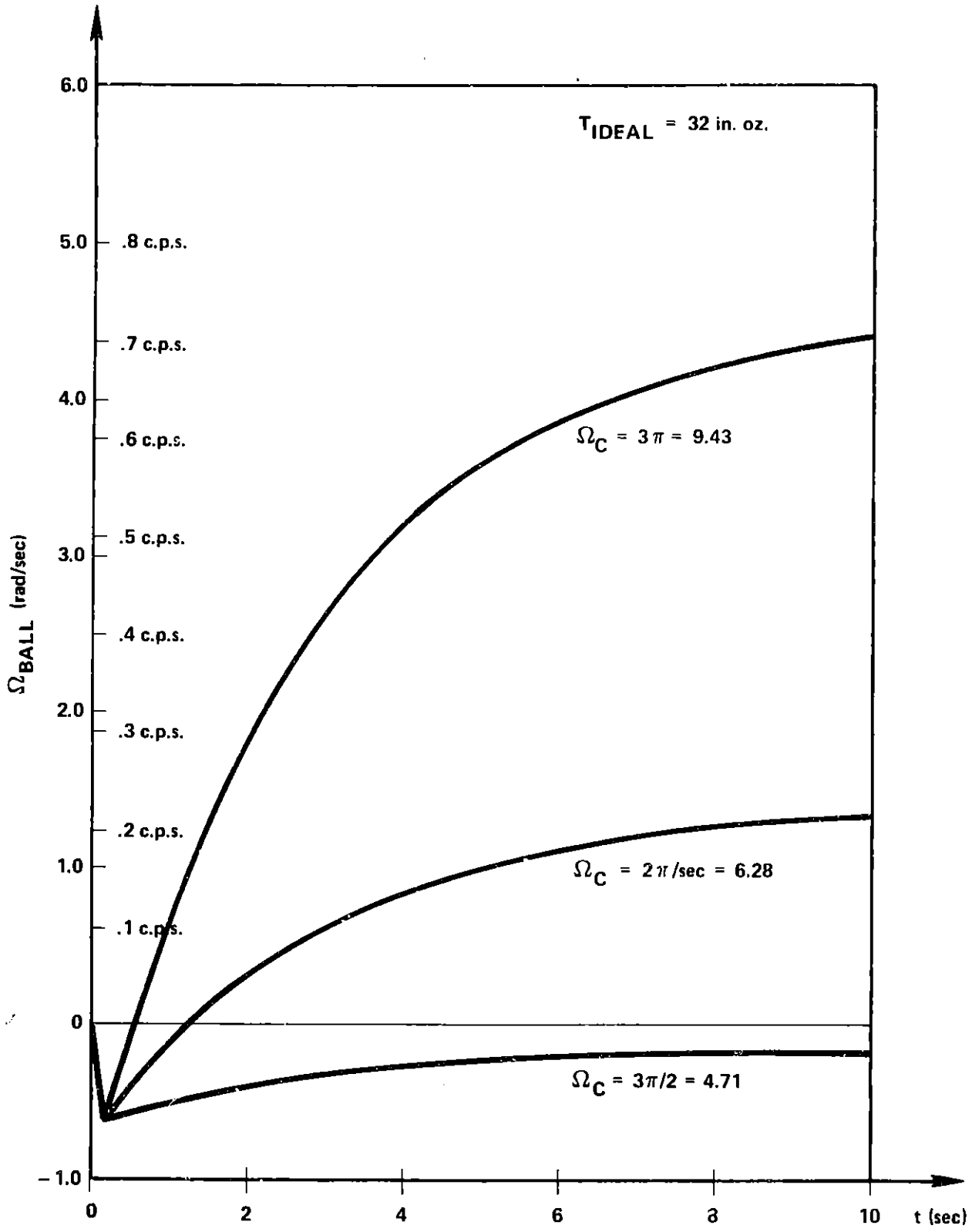

Figure 4-19. Angular Velocity of Ball Versus Time

show that the jets are inadequate for such high case rotation rates. This information reinforces that found in the previous section from the load line graphs (Figures 4-13 and 4-14).

CHAPTER 5

POWER REQUIREMENTS AND PUMP DESIGN

5.1 Modeling the Pump

The pressure needed to deliver a specified flow to all the components of the hydraulic system is supplied via a centrifugal pump called a "turbo-pump". The torquing power to operate the pump impeller comes from two identical eight-pole three-phase induction motors acting on the extended pump impeller which doubles as the rotor for the motor. (See Figure 1-7.) A model for the pump is needed in order to see its interaction with the system components. The purpose of this model is to show tendencies within the system. It is not intended for use in pump optimization. The detailed design and modeling of pump performance is a complicated procedure and beyond the scope of this work.

The pump as modeled in this work is composed of two major parts: (1) the impeller-rotor, and (2) the diffuser. The pump impeller raises the pressure of the fluid passing through it and then passes the fluid on to the diffuser (not shown in Figure 1-7). The diffuser channels the flow away from the impeller blades through passageways of constantly increasing cross-sectional area. The fluid velocity is lowered while pressure increases due to the Bernoulli transformation of kinetic engergy into pressure energy.

5.1.1 Pump Characteristics

Any pump has a certain pressure-flow characteristic which is dependent upon its speed of operation. Figure 5-1 shows an example of what these characteristics might look like for a random pump. The family of curves shown in Figure 5-1 could be reduced to one characteristic curve for a

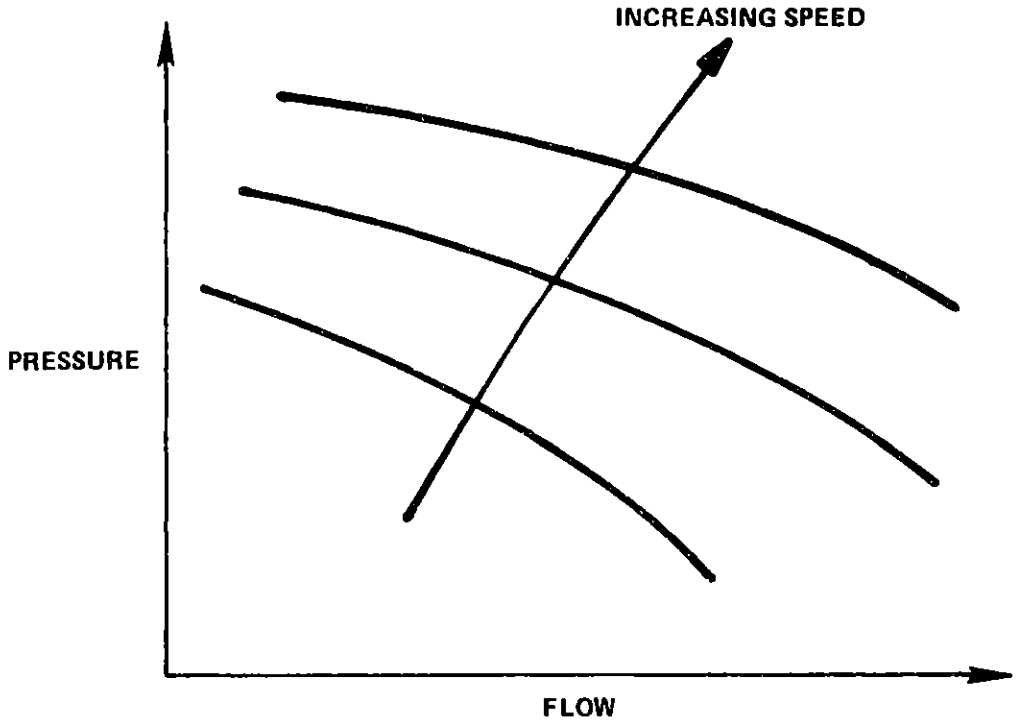

Figure 5-1. Pressure-Flow Characteristics for a Typical Pump

particular pump by plotting a non-dimensional pressure ψ versus a non-dimensionalized flow ϕ. (These quantities will be defined in equations (5-5) and (5-6)). One set of measurements then would be all required to determine ψ as a function of ϕ and thus predict pump performance under conditions other than those measured. The pressure head H across the impeller and the flow rate Q through the impeller must therefore be stated in terms of thier respective non-dimensionalized counterparts ψ and ϕ.

The pressure head raised across the impeller blades is given by

$$H = \rho \, (r_2 \Omega \, v_{\theta_2} - r_1 \Omega v_{\theta_1}) \tag{5-1}$$

where r_1 and r_2 are the impeller inner and outer radii respectively, v_{θ_1} and v_{θ_2} are the tangential velocities at the inner and outer radii and Ω is the impeller rotational velocity.

A schematic of this system's impeller is given in the upper portion of Figure 5-2. Beneath is shown a velocity vector diagram corresponding to flow past one impeller blade. The angle the blade makes with respect to the radius is approximately constant and is denoted by the vane angle β_v. The radial velocity at radii r_1 and r_2 are denoted by v_{r1} and v_{r2}. The fluid velocity relative to the blade is v_{rel}. From the vector diagram of Figure 5-2 it can be seen that

$$v_{\theta_1} = r_1 \Omega - v_{r1} \tan \beta_v \tag{5-2}$$

$$v_{\theta_2} = r_2 \Omega - v_{r2} \tan \beta_v$$

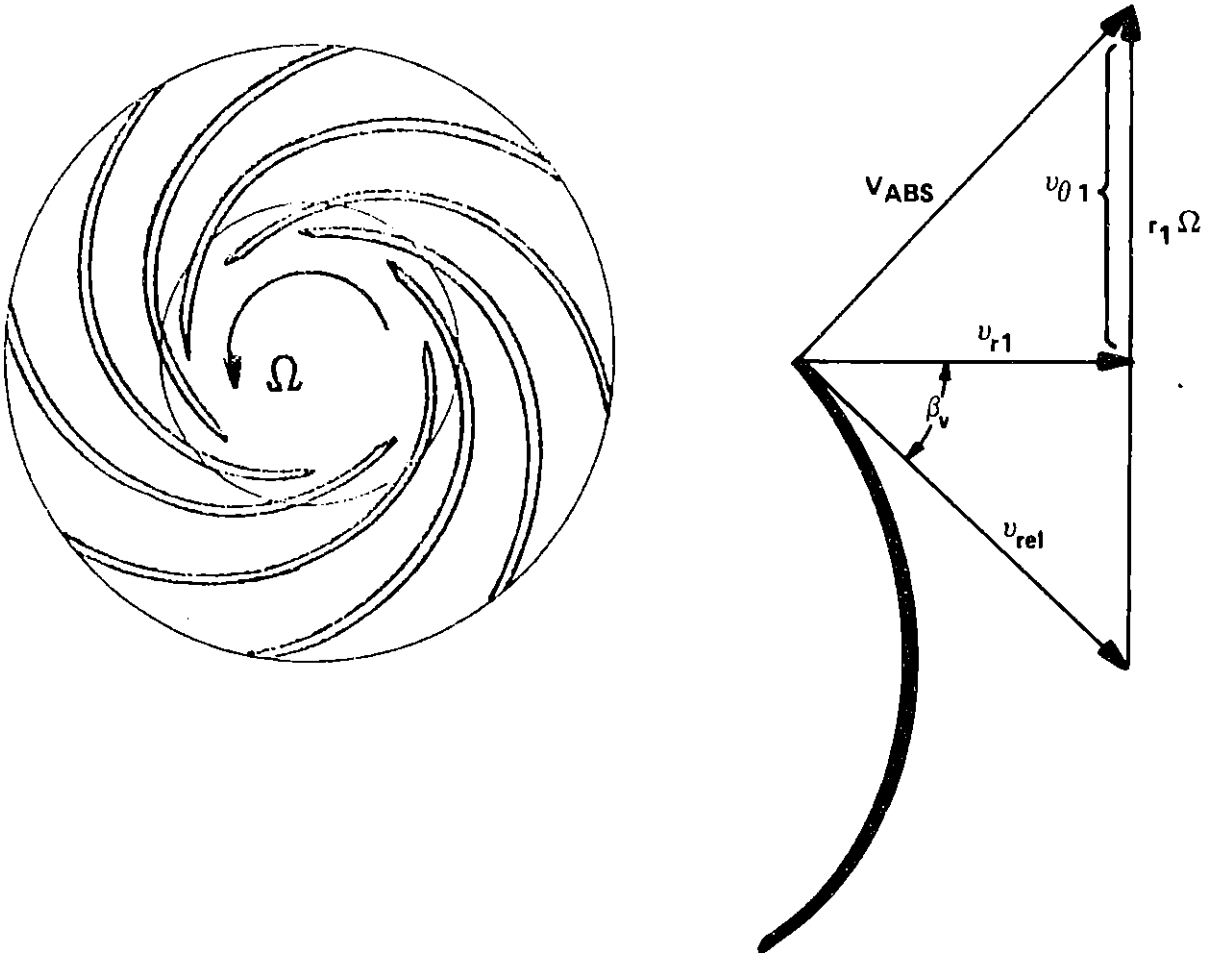

Figure 5-2. Pump Impeller and Corresponding Fluid Velocity Triangle

From continuity principles and the assumption of an incompressible flow the radial fluid velocities can be given by the radial volumetric flow Q divided by the cross-sectional area at the point in question:

$$v_{r1} = \frac{Q}{2\pi r_1 b_1}$$
$$v_{r2} = \frac{Q}{2\pi r_2 b_2} \qquad (5\text{-}3)$$

where the b's are the widths of the impeller blades or depths normal to the figure. Substituting equations (5-2) and (5-3) into (5-1) and manipulating gives the following formula for the pressure head H:

$$H = \rho r_2^2 \Omega^2 \left\{ 1 - \left(\frac{r_1}{r_2}\right)^2 - \frac{Q \tan \beta_v}{2\pi r_2^2 \Omega b_2} \left(1 - \frac{b_2}{b_1}\right) \right\} \qquad (5\text{-}4)$$

This formula is of the form

$$H = a_1 (\Omega^2) - a_2 (\Omega) Q \qquad (5\text{-}5)$$

where a_1 and a_2 are constants for a specific value of Ω. The pressure flow relation is thus a family of lines whose y intercept a_1 and slope $-a_2$ depend on the pump speed Ω.

The pressure can be made non-dimensional by dividing by $\rho r_2^2 \Omega^2$ to give

$$\psi = 1 - \left(\frac{r_1}{r_2}\right)^2 - \frac{Q \tan \beta_v}{2\pi r_2^2 \Omega b_2} \left(1 - \frac{b_2}{b_1}\right) \qquad (5\text{-}6)$$

The flow coefficient can be normalized to the blade tip velocity and outer cross-sectional area product $(2\pi r_2 b_2)\ (r_2\Omega)$ or

$$\phi \equiv \frac{Q}{2\pi r_2^2 b_2 \Omega} \tag{5-7}$$

Equation (5-7) can be substituted into equation (5-6) to give a ψ - ϕ relationship

$$\psi = 1 - \left(\frac{r_1}{r_2}\right)^2 - \phi \tan \beta_v \left(1 - \frac{b_2}{b_1}\right) \tag{5-8}$$

The ψ - ϕ relationship above is a linear one of the form

$$\psi = a_1 - a_2 \phi \tag{5-9}$$

where by direct comparison between equations (5-8) and (5-9) the constants a_1 and a_2 are seen to be

$$\begin{aligned} a_1 &= 1 - \left(\frac{r_1}{r_2}\right)^2 \\ a_2 &= \tan \beta_v \left(1 - \frac{b_2}{b_1}\right) \end{aligned} \tag{5-10}$$

Thus the family of straight lines of equation (5-4) reduces to one straight line with y intercept a_1 and slope $-a_2$. For this system a_1 = .758 and a_2 = 1.407 and the ψ - ϕ relation is shown in Figure 5-3. The dashed lines in the figure indicate that the model fails at very low and very high flow rates.

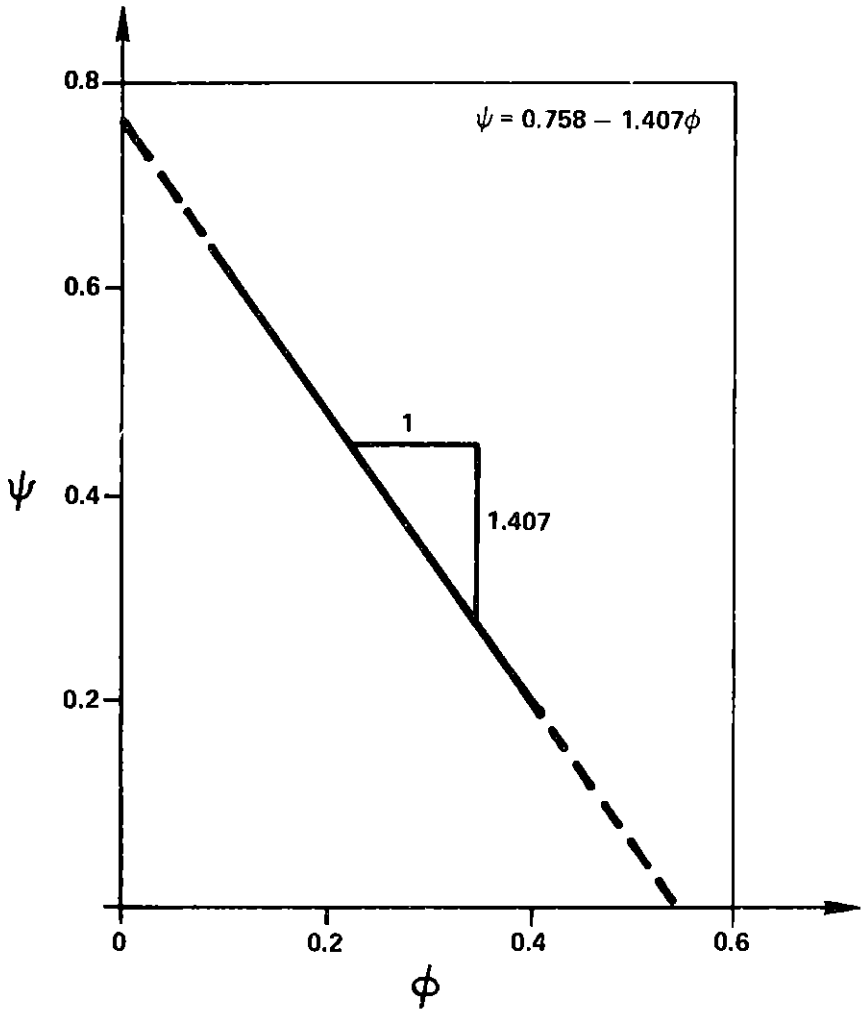

Figure 5-3. Pump Nondimensional Head Versus Nondimensional Flow Characteristic

Another important parameter in the non-dimensional analysis of a pump is its specific speed N_s which is given by

$$N_s = \frac{\Omega Q^{1/2}}{(H/\rho)^{3/4}} = \frac{(\pi\phi\varepsilon_2)^{1/2}}{\psi^{3/4}} \tag{5-11}$$

ε_2 here is a geometric ratio given by the cross-sectional flow area at the impeller outer tip divided by the impeller size

$$\varepsilon_2 = \frac{A_2}{\pi r_2^2} \tag{5-12}$$

Assuming thin impeller blades A_2 is approximately given by $2\pi r_2 b_2$ and ε_2 reduces to

$$\varepsilon_2 = 2\,\frac{b_2}{r_2} \tag{5-13}$$

The characteristic or optimum specific speed of a pump is typically measured during operation at peak efficiency. (Efficiency for a pump is the ratio of the output fluid power $\dot{H}Q$ to the input mechanical power or torque velocity $T\Omega$.) It is an indication of the relative magnitude of the angular momentum of the fluid versus the pressure head. Knowledge of the specific speed of a pump gives a good indication of the shape of the impeller blades as seen in Figure 5-4.[11]

The introduction of the optimum specific speed is intended to give some insight into the rationale behind the pump design for this system. The specific speed for the turbopump calculated from the above pump model is .59.

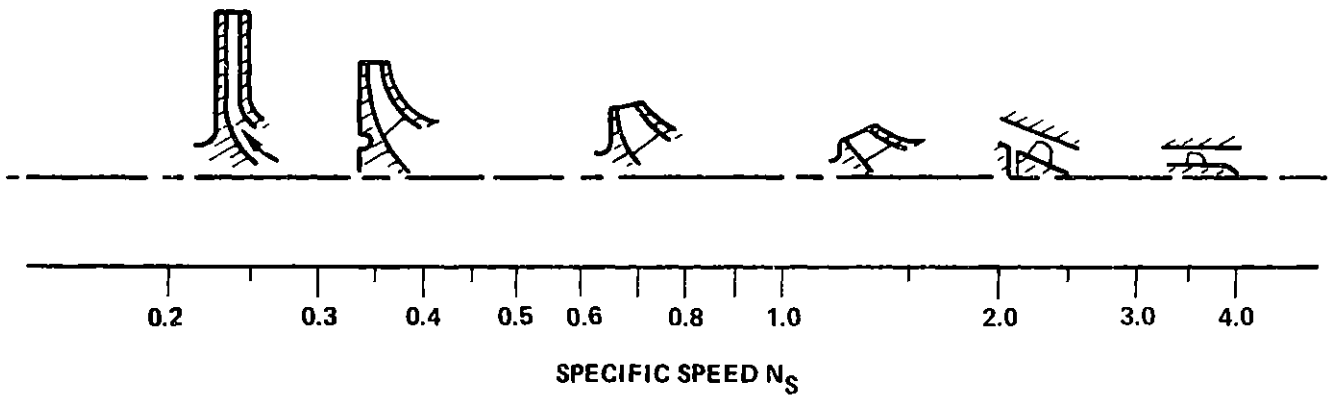

Figure 5-4. Typical Proportions for Commerical Pump Designs at Various Values of Specific Speed. The Specific Speed is Given in Dimensionless Terms and is Based on the Rotative Speed in Rad/Sec

(The measured value was about .67.) A comparison of Figures 5-2 and 5-4 shows the similarity in blade shape.

In the non-dimensional analysis of a pump one more important parameter should be considered. It is known as the Reynold's number and serves to indicate the relative importance of inertia to viscous forces acting within a pump. The Reynold's number is typically evaluated at the outer tip of the impeller baldes and is given by

$$Re = \frac{r_2^2 \Omega}{\nu} \tag{5-14}$$

Calculation of the Reynold's number for a pump is an indication of the variations of ψ, ϕ, and the pump efficiency η_p. For a Reynold's number of about 5×10^5 or greater ψ, ϕ, and η_p are essentially independent of the Reynold's number, and may be expressed as a function of ϕ only. The Reynold's number for the turbopump at a speed of 16,000 rpm is 1.95×10^5 which is only slightly below the value necessary to neglect Reynold's number effects. The model gives linear relationships between ψ and ϕ, and H and Q, because these effects are neglected. At Reynold's numbers lower than 5×10^5 viscous forces begin to come into play and not as high as head H can be obtained. The head lost due to firction h_ℓ is a nonlinear function of the flow so when this is subtracted from the ideal head the result is no longer linear. (See Figure 5-5.)[12] Therefore the linear ψ-ϕ characteristic of Figure 5-3 is not valid at low and high flow extremes.

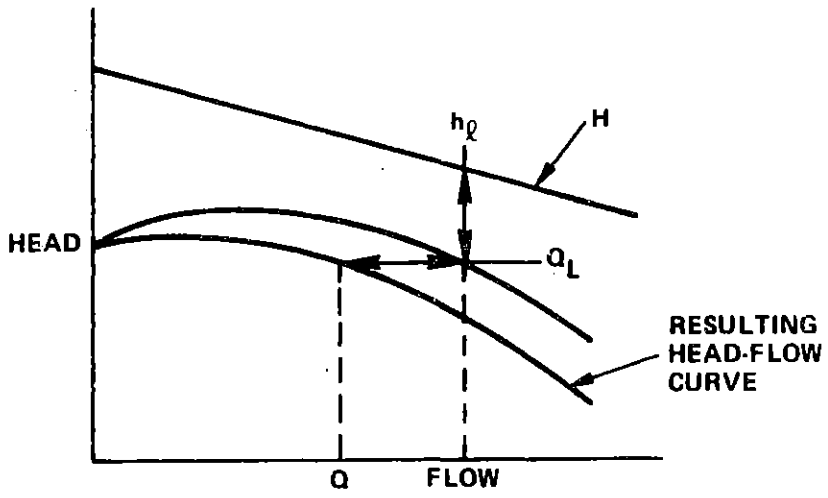

Figure 5-5. Construction of Pressure-Flow Characteristic

For the rough purposes of this model the Reynold's number effect has been neglected. The lowest speed at which the pump is operated is about 8,500 rpm and the highest about 16,000 rpm. The Reynold's number range is thus

$$1.04 \times 10^5 < Re < 1.95 \times 10^5$$

To compensate for the head losses at these fairly high Reynold's numbers the model ignores pressure gains across the diffuser. In reality the diffuser does not truly compensate for head losses across the entire range of pump operation. At high flows viscous energy losses decrease and there is sufficient kinetic energy in the fluid that the diffuser is able to use this to approximately recover the viscous head losses. At low flow rates, however, viscous losses are greater and the diffuser does not have enough kinetic energy to recover the losses. Although for pump design purposes the compensating diffuser approximation is certainly not valid, it is adequate to give a pump characteristic to be used in studying pump-system interactions. The effect of the diffuser would only change the slope of the $\psi - \phi$ curve slightly.

5.2 Pump Loadline

The previous section gave a model for predicting pump pressure-flow characteristics at different operational speeds. A loadline for the pump must now be calculated which gives the composite pressure-flow relation for all the hydraulic components. Each point on this curve dictates the specific pump operational speed necessary to support the load.

The hydraulic system complete with its interactions with the mechanical aspects of the ball was shown in Figure 1-9. For the purposes of this discussion we are interested only in the fluid resistive part of the network seen by the pump; i.e., the fine lines on Figure 1-9.[13] This portion of the figure may be simplified somewhat by collapsing certain resistances into equivalent resistances with different pressure-flow relations according to the basic rule that for series resistances the pressures add and for resistances in parallel, the flows add. This was done. The pad orifice and pad sill resistances were converted to an equivalent pad resistance labeled P. The two parallel subsections each consisting of a valve filter, nozzle, thrust bearing, and radial bearing were reduced to an equivalent resistance for the two half-valves labeled 2HV. The two parallel turbopump thrust bearings were similarly reduced.

For the moment let us look only at the pad and valve pressure-flow characteristic for one half of the sphere. We are prevented from reducing these components further to just one equivalent resistance by the existence of the equalizing resistance in the

circuit which makes the analysis indeterminate; i.e., it can not be solved explicitly and an iterative solution is needed. To avoid using an iterative procedure, however, we will try to bound the solution by considering what the equivalent pressure flow relation would be for these components if (1) the equalizing passage were not there (open circuited) or (2) the passages provided no resistance to flow (short circuited). Figure 5-6 illustrates the equivalent network under each of these conditions. Each of these cases is now determinant.[14]

The pressure-flow relation characterizing the load line for the entire system was affected only very slightly by the two methods of calculation above. At an ideal valve torque of 32 in.-oz (.35 gpm flow through each nozzle) the short circuit calculation predicted that a pump pressure of 25 psi would induce a total flow through the components of 5.67 gpm. The open circuit calculation under the same pump pressure and nozzle flow conditions yielded a total flow which was only .05% lower than that calculated by the short circuit method. The effect of the equalizing passages is therefore negligible and either method for the calculation of the system load line is adequate to within the ranges of validity of the component models. The load line calculated by the open circuit method, however, will always predict a higher pressure at a specified flow than will the short circuit calculation so it perhaps is the more conservative of the two methods.

The load line calculated by the open circuit method is plotted in Figure 5-7. Also shown is the family of pump characteristics at different operational speeds as found from equation (5-4). Again

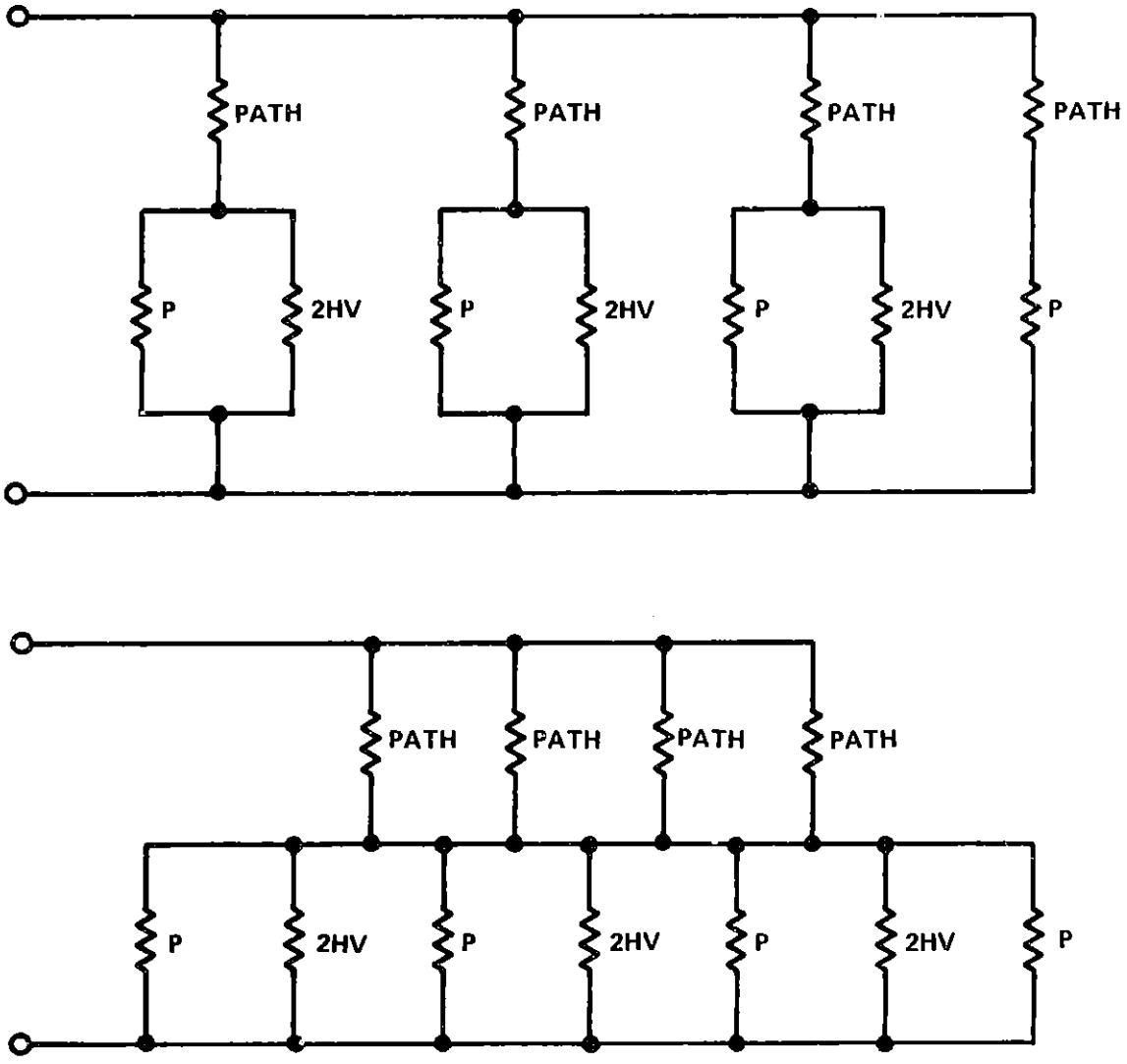

Figure 5-6. Simplified Hydraulic Circuit for Suspension and Torquing Subsystems of One Half of the Ball

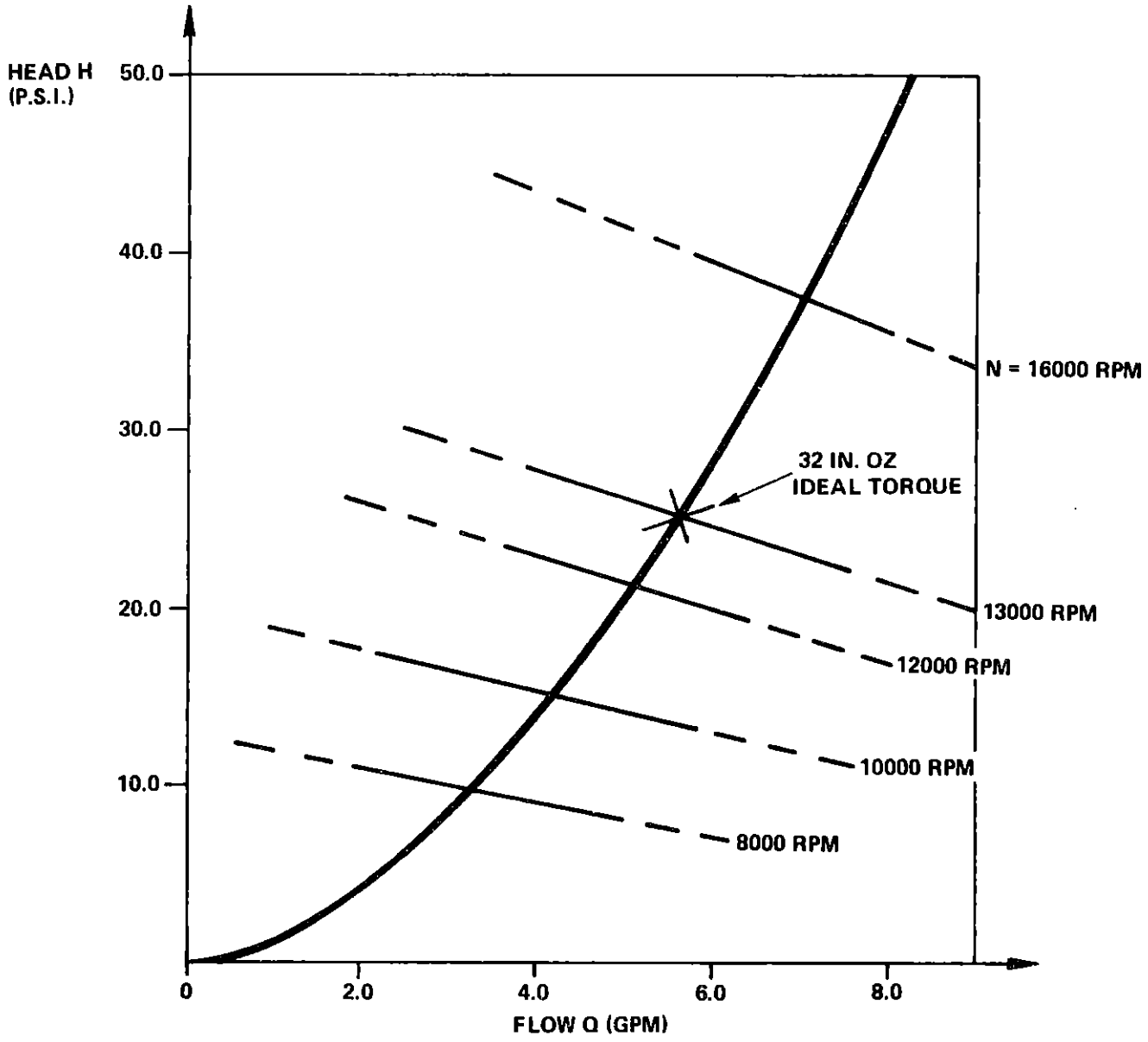

Figure 5-7. System Hydraulic Loadline

the dashed lines indicate the model begins to fail at both very high and very low flow rates. The intersection of the load line and pump characteristic dictates the operational speed of the pump under those particular flow conditions. One point in particular is shown. For an ideal valve torque of 32 in.-oz the pump must run at a speed of 13,000 rpm.

The question arises as to the effect of ball translation on this load line. This effect is also very slight. At 25 psi and 32 in.oz of valve torque a ball displacement of .002 in. along a cube diagonal produces only .1% decrease in total flow.

REFERENCES

[1]J. Lowen Shearer, Aruthur T. Murphy, and Herbert H. Richardson, Introduction to System Dynamics (Reading, Ma: Addison-Wesley Publishing Company, 1971), pp 48, 86, 93, 94.

[2]Phillip Mighdoll, "A First Order Analysis of Tilted Pool Bearings", CSDL Internal Memorandum, February 8, 1972.

[3]Rolf H. Sabersky, Allan J. Acosta, and Edward G. Hauptmann, Fluid Flow (New York: The MacMillan Company, 1971), pp 91, 92.

[4]Michigan Wire Cloth, Performance Data on Metal Filter Cloth (Michigan: Michigan Dynamics, Inc.).

[5]Henry M. Paynter, Private communications regarding effective ball mass (March 10, 1976).

[6]J. Lowen Shearer, Arthur T. Murphy, and Herber H. Richardson, p. 312.

[7]J. Lowen Shearer, Arthur T. Murphy, and Herbert H. Richardson, p. 367.

[8]Rolf H. Sabersky, Allan J. Acosta and Edward G. Hauptmann, p. 169.

[9]Phillip Mighdoll, "An Improved Model of the Torque-Speed Characteristic of Enclosed Reaction Jet Torquers", CSDL Internal Memorandum, June 26, 1969.

[10]The Chemical Rubber Company, Handbook of Chemistry and Physics, (Ohio: The Chemical Rubber Company, 1969), p. A-166, Forms 97, 98.

[11]Rolf H. Sabersky, Allan J. Acosta, and Edward G. Hauptmann, p. 429.

[12]D. H. Norrie, An Introduction to Incompressible Flow Machines, (New York: American Elsevier Publishing Company, Inc. 1963), p. 75.

[13]Charles Stark Draper Laboratories, Outline of Hydraulic Subsystem Presentation. (June, 1975) p. 6.

[14]Henry M. Paynter, Private communication regarding indeterminant non-linear circuit analysis (March 26, 1976).

BIBLIOGRAPHY

Boyce, William E., and DiPrima, Richard C. Elementary Differential Equations. New York: John Wiley & Sons, Inc., 1969.

Charles Stark Draper Laboratories. Outline of Hydraulic Subsystem Presentation. June 1975.

The Chemical Rubber Company. Handbook of Chemistry and Physics. Cleveland, Ohio: The Chemical Rubber Company, 1969.

Crandall, Stephen H., Karnopp, Dean C., Kurtz, Edward F., Jr., and Pridmore-Brown, David C. Dynamics of Mechanical and Electromechanical Systems. New York: McGraw-Hill Book Company, 1968.

Michigan Wire Cloth. Performance Data on Metal Filter Cloth. Detroit, Michigan: Michigan Dynamics, Inc.

Mighdoll, Phillip. A First Order Analysis of Tilted Pool Bearings. CSDL Internal Memorandum, February 8, 1972.

Mighdoll, Phillip. An Improved Model of the Torque-Speed Characteristic of Enclosed Reaction Jet Torquers. CSDL Internal Memorandum, June 26, 1969.

Mighdoll, Phillip. "Properties of FC-77" from 3M Company Inert Fluorochemical Liquids. CSDL Internal Memorandum, November 6, 1969.

Norrie, D. H. An Introduction to Incompressible Flow Machines. New York: American Elsevier Publishing Company, Inc., 1963.

Pao, Richard H.F. Fluid Dynamics. Columbus, Ohio: Charles E. Merrill Books, Inc., 1967.

Paynter, Henry M. Class Notes from M.I.T. Course 2.141 Modeling and Simulation of Dynamic Systems. Spring, 1975

Paynter, Henry M. Private communication regarding effective ball mass. March 10, 1976.

Paynter, Henry M. Private communication regarding indeterminant non-linear circuit analysis. March 26, 1976.

Sabersky, Rolf H., Acosta, Allan J., and Hauptmann, Edward G. Fluid Flow. New York: The MacMillian Company, 1971.

Shapiro, Ascher H. Class Notes from M.I.T. Course 2.25 Advanced Fluid Mechanics. Fall, 1975

BIBLIOGRAPHY (Continued)

Shearer, J. Lowen, Murphy, Aruthur T., and Richardson, Herbert H. Introduction to System Dynamics. Reading, Ma: Addison-Wesley Publishing Company, 1971.

Whitney, Daniel E. Static and Dynamic Performance of Ball Bearing Hydrostatic Support Pad. CSDL Engineering Note E-2589, July, 1971.

APPENDIX A

EFFECTIVE BALL MASS

When the inner ball translates within the outer shell its mass appears greater than its actual density-volume product. This phenomenon is due to the fact that in order to move the ball relative to the outer shell the force required must accelerate not only the actual mass of the ball itself but also the mass of the annular fluid which must be redistributed to allow ball eccentric positioning. The combined kinetic co-energy of the ball and annular fluid when the ball is subjected to a velocity V can be used to determine an "effective" ball mass.

To proceed in this vein, the ball and shell are modeled as two octagons of revolution; i.e., their cross section is that of two concentric octagons. This model was divided into five regions as shown in Figure A-1. The kinetic co-energy of the annular fluid in each of these regions is then determined when the ball is moved instantaneously with velocity V. Assuming flow incompressibility we can write the continuity equation for each of the five regions. The cross sectional area of a region was taken at its mid-length. With the convention that small v's refer to fluid velocity and the subscripts refer to the regions as numbered in Figure A-1, we get the five equalities

$$V\pi\left(R \sin \frac{\pi}{8}\right)^2 = v_1 \, 2\pi R \sin \frac{\pi}{8} h_o \tag{A-1}$$

$$V\pi\left[\left(R \sin \frac{3\pi}{8}\right)^2 - \left(R \sin \frac{\pi}{8}\right)^2\right] + V\pi\left(R \sin \frac{\pi}{8}\right)^2 = v_2 \, 2\pi R \sin \frac{\pi}{4} \frac{h_o}{\cos \frac{\pi}{4}}$$

$$V\pi\left(R \sin \frac{3\pi}{8}\right)^2 = v_3 \, 2\pi R \cos \frac{\pi}{8} h_o$$

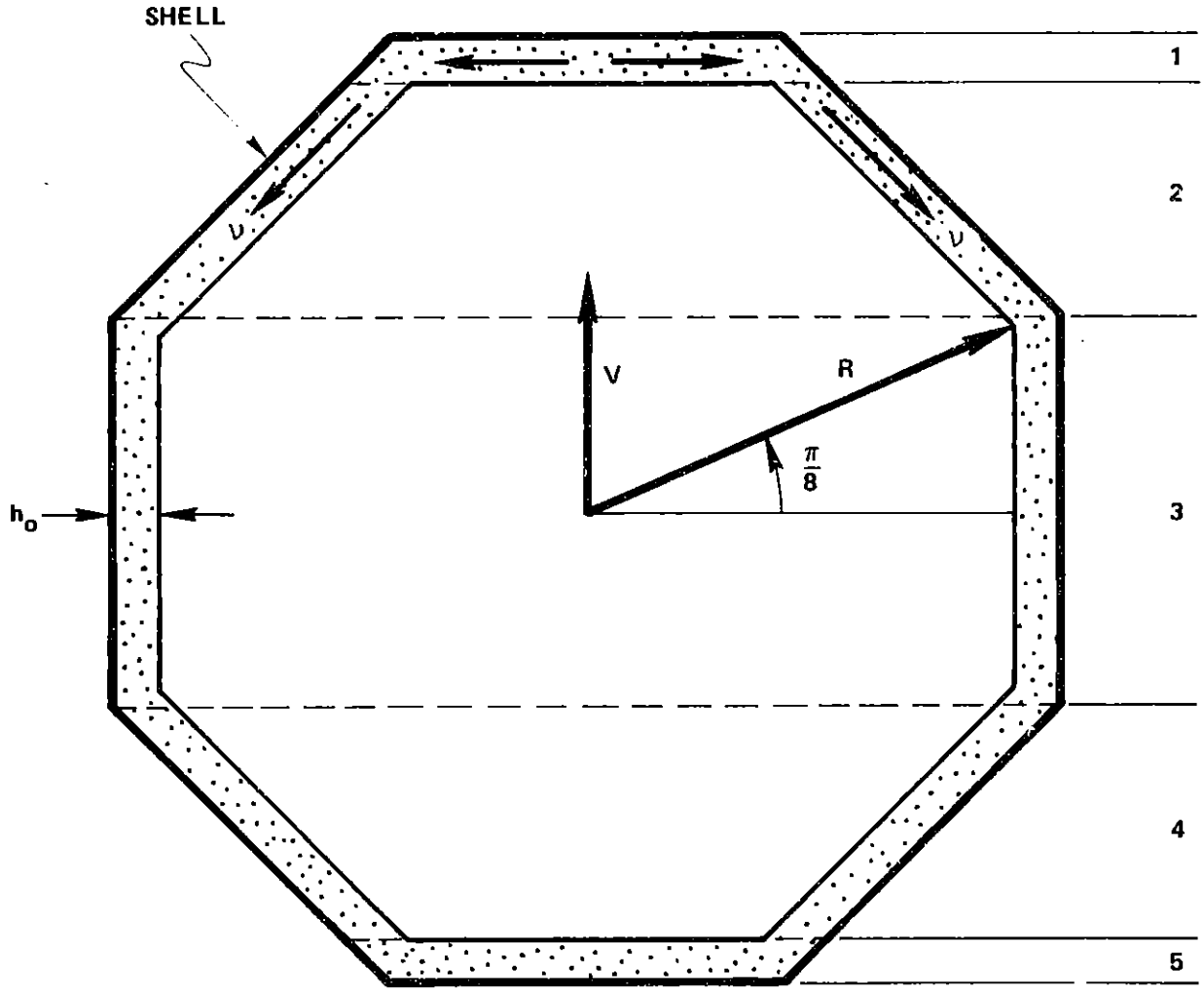

Figure A-1. Model for Calculating Effective Ball Mass

$$V\pi\left(R \sin \frac{3\pi}{8}\right)^2 - V\pi\left[\left(R \sin \frac{3\pi}{8}\right)^2 - \left(R \sin \frac{\pi}{8}\right)^2\right] = \upsilon_4 \, 2\pi R \sin \frac{\pi}{4} \frac{h_o}{\cos \frac{\pi}{4}}$$

$$V\pi\left(R \sin \frac{\pi}{8}\right)^2 - V\pi\left(R \sin \frac{\pi}{8}\right)^2 = \upsilon_5 \, 2\pi R \sin \frac{\pi}{8} \, h_o$$

Solving for the fluid velocities gives

$$\begin{aligned}
\upsilon_1 &= \frac{R \sin \frac{\pi}{8}}{2h_o} V &&= .19 \frac{R}{h_o} V \\
\upsilon_2 &= \frac{R \sin^2 \frac{3\pi}{8}}{2h_o} V &&= .43 \frac{R}{h_o} V \\
\upsilon_3 &= \frac{R \sin^2 \frac{3\pi}{8}}{2h_o \cos \frac{\pi}{8}} V &&= .46 \frac{R}{h_o} V \\
\upsilon_4 &= \frac{R \sin^2 \frac{\pi}{8}}{2h_o} V &&= .07 \frac{R}{h_o} V \\
\upsilon_5 &= 0
\end{aligned} \qquad \text{(A-2)}$$

To determine the fluid masses in one segment we multiply the fluid density ρ by the segment volume V. Noting that segments 2, 3, and 4 have length $2R \sin \frac{\pi}{8}$ the five volumes become

$$
\begin{aligned}
V_1 &= \left(\pi \quad R \sin \frac{\pi}{8}\right)^2 h_o \qquad\qquad = .46\ R^2\ h_o \\
V_2 &= \left(2\pi R \sin \frac{\pi}{4}\right) h_o \left(2R \sin \frac{\pi}{8}\right) = 3.4\ R^2\ h_o \\
V_3 &= \left(2\pi R \cos \frac{\pi}{8}\right) h_o \left(2R \sin \frac{\pi}{8}\right) = 4.4\ R^2\ h_o \\
V_4 &= \left(2\pi R \sin \frac{\pi}{4}\right) h_o \left(2R \sin \frac{\pi}{8}\right) = 3.4\ R^2\ h_o \\
V_5 &= \pi\left(R \sin \frac{\pi}{8}\right)^2 h_o = .46\ R^2\ h_o
\end{aligned}
\qquad \text{(A-3)}
$$

The actual mass of the ball is given by its density ρ_s times its volume $\frac{4}{3}\pi R^3$.

We are not ins a position to determine the total kinetic co-energy T* of the ball and annular fluid. It is given by the sum of each of the individual kinetic co-energies of the ball and annular fluid segments.

$$T^* = \frac{1}{2}\left\{\rho_s \frac{4}{3}\pi R^3 V^2 + \rho\left[V_1 \upsilon_1^2 + V_2 \upsilon_2^2 + V_3 \upsilon_3^2 + V_4 \upsilon_4^2 + V_5 \upsilon_5^2\right]\right\} \qquad \text{(A-4)}$$

Substituting equations A-2 and A-3 into A-4 simplifies the total kinetic co-energy to

$$T^* = \frac{1}{2}\left[\rho_s \frac{4}{3}\pi R^3 V^2 + 1.6\ \rho \frac{R^4}{h_o} V^2\right] \qquad \text{(A-5)}$$

which can be rewritten as

$$T^* = \frac{1}{2}\left[\rho_s \frac{4}{3}\pi R^3 \left(1 + \frac{\rho}{\rho_s}\frac{1.2\ R}{h_o}\right)\right]V^2 \qquad \text{(A-6)}$$

The bracketed quantity in equation (A-6) can be viewed as the effective ball mass. For a neutrally buoyant sphere $\rho_s = \rho$ and it can be seen that the effective mass is 35 times the actual ball mass for an 8.5 inch ball with a .15 inch annular gap.

The above technique for determining the effective mass could be extended further to give better estimates by dividing the gap and ball into a greater number of smaller segments. Hand calculations would become more tedious and computerization of the procedure would then be advisable.

APPENDIX B

JET STREAM MODEL

The calculation for the stream area in Section 4.3.1 gave the stream area as

$$A_s = \theta [(R+h)^2 - R^2] \tag{4-17}$$

which, when linearized for $\frac{h}{R} << 1$ yielded

$$A_s \cong 2\theta Rh \tag{4-18}$$

The result for θ in equation (4-19) implicitly assumes a jet width such that the given trigonometric relation holds true. To be truly correct this statement is exact only when the chord on the outer shell representing the jet stream width is also tangent to the inner ball. Figure B-1 shows the more general case. Here θ is given by

$$\theta = \tan^{-1} \left[\frac{\sqrt{(R+h)^2 - (R+\varepsilon h)^2}}{R + \varepsilon h} \right] \tag{B-1}$$

where ε is some multiplicative factor for h which can be adjusted to acommodate the chord length representing the jet stream width. (In Chapter 4 for the cord-tangency situation ε was 0.) Linearizing equation (B-2) for $\frac{h}{R} << 1$ and $\frac{\varepsilon h}{R} << 1$ gives

$$\theta \cong \sqrt{2 \frac{h}{R}} \left[\frac{\sqrt{1 - \varepsilon}}{1 + \frac{\varepsilon h}{R}} \right] \tag{B-2}$$

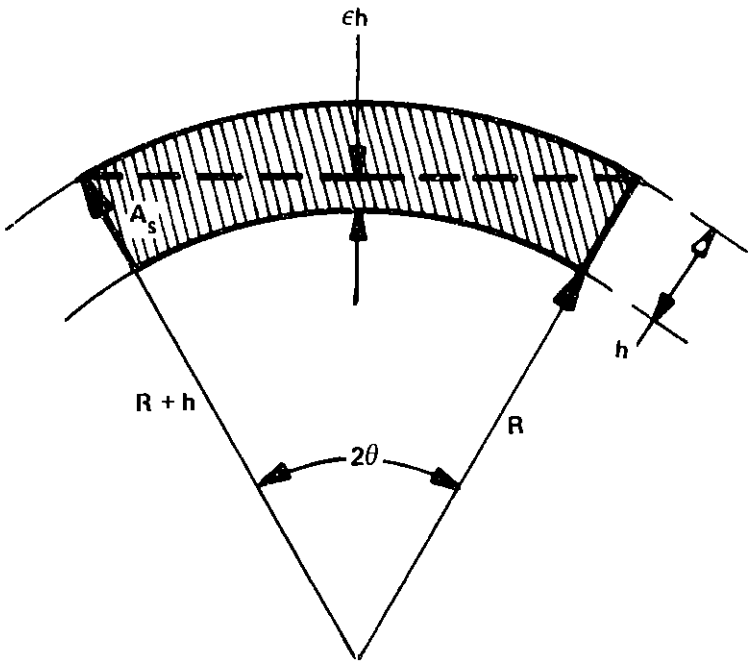

Figure B-1. Generalized Geometry of Jet Stream Cross Section

which, when substituted in the equation for A_s gives

$$A_s \simeq \sqrt{8Rh^3}\left[\frac{\sqrt{1-\varepsilon}}{1+\frac{\varepsilon h}{R}}\right] \tag{B-3}$$

Equation (4-16) gave the stream velocity as depending inversely on the square of the stream area. Substituting this modified value for A_s into equation (4-16) gives

$$V_s = \frac{Q_j}{\sqrt{A_j\sqrt{8Rh^3}}}\left[\frac{\sqrt{1-\varepsilon}}{1+\frac{\varepsilon h}{R}}\right]^{-\frac{1}{2}} \tag{B-4}$$

By assuming $\varepsilon = 0$ in Section 4.3.1 a percentage error of $\left[\frac{\sqrt{1-\varepsilon}}{1+\frac{\varepsilon h}{R}}\right]^{-\frac{1}{2}}$ is accrued when ε deviates from 0. Figure B-2 plots the bracketed quantity for $-.75 < \varepsilon < .75$. These limits correspond to jet stream widths between 3 in. ($\varepsilon = .75$). At wider jet stream widths the actual stream velocity may be only about 86% of that calculated in Chapter 4. At narrower jet stream widths the actual velocity may be as much as 43% greater than that calculated in Section 4.3.1. Guessing at a value for ε (such as 0) gives at most a ball-park figure for the characteristic stream velocity.

The crux of the matter lies in understanding exactly what determines the jet stream width (and corresponding ε value) and stream velocity. More knowledge is needed of the entrainment happening in the spreading region of the jet. The above analysis and that in Section 4.3.1 assumed dissipative turbulent and viscous forces in this region were approximately balanced by the momentum influx from the entrained flow. Let us examine what order of magnitude of entrainment is implied by the preceding analyses.

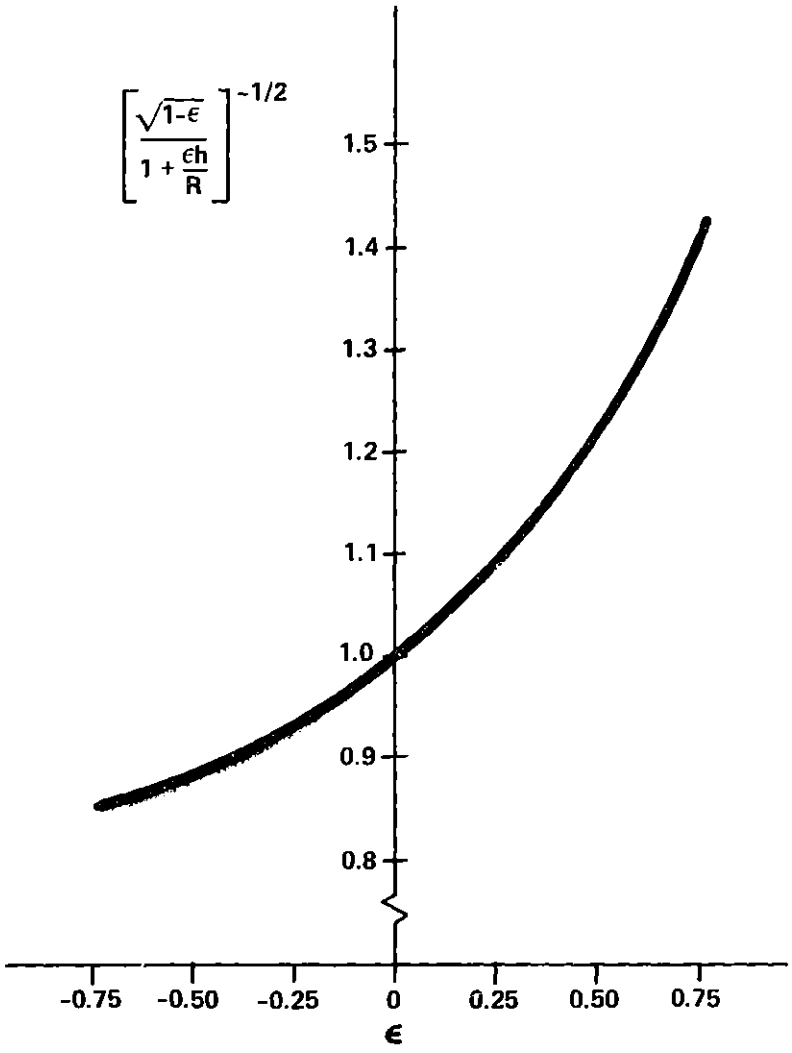

Figure B-2. Jet Steam Velocity Error Dependency on Approximation for Stream Width

The entrained flow Q_ϵ is given by the jet stream volumetric flow rate minus the jet nozzle contribution

$$Q_E = Q_s - Q_j \tag{B-5}$$

Noting that

$$Q_s = V_s A_s \tag{B-6}$$

equation (4-16) can be rewritten to give Q_s in terms of Q_j

$$Q_s = \sqrt{\frac{A_s}{A_j}}\, Q_j \tag{B-7}$$

The entrained flow rate may now be given in terms of the jet flow rate by substituting equation (B-7) into (B-5) to give

$$Q_E = \left(\sqrt{\frac{A_s}{A_j}} - 1\right) Q_j \tag{B-8}$$

For jet widths between 1 and 3 inches the entrained flow rate ranged between 10 and 18 times the jet nozzle flow rate. For $\epsilon = 0$ the entrained flow rate was 15 times the jet flow rate. These values appear very large. Intuitively one would expect something much smaller. If one stops and thinks, however, one must realize that flow is squirted from the nozzle at velocities on the order of one thousand inches per second into a medium of roughly zero velocity. Perhaps with this realization the 15 fold entrainment is more palatable. In all likelihood some error is introduced in the initial assumption that the momentum influx in the spreading region carried in by the entrained flow balances the turbulent and viscous losses there. Clearly a more complex phenomenon is occurring in this region than the above model portends.